THE GEOLOGICAL SOCIETY
OF AMERICA®

Influence of multistage hydrothermal fluids on dolomite reservoirs: A case study from the Lower Ordovician Yeli-Liangjiashan Formation in the Chengdao-Zhuanghai area, Jiyang subbasin, Bohai Bay Basin, China

Kai Sheng[1], Yanzhong Wang[1,†], Yingchang Cao[1,2], Shuping Wang[3], Yongshi Wang[4], Shuai Ma[4], and Yujie Du[1]
[1]*School of Geosciences, China University of Petroleum (East China), Qingdao 266580, China*
[2]*Laboratory for Marine Mineral Resources, Qingdao National Laboratory for Marine Science and Technology, Qingdao 266071, China*
[3]*Petroleum Industry Training Service, China University of Petroleum (East China), Qingdao 266580, China*
[4]*Shengli Oilfield Company, SINOPEC, Dongying 257001, China*

ABSTRACT

It remains controversial whether the influence of hydrothermal fluids on dolomite reservoirs is dominated by dissolution or precipitation. In this study, the influence of multistage hydrothermal fluids on the dolomite reservoirs of the Lower Ordovician Yeli-Liangjiashan Formation in the Chengdao-Zhuanghai area was investigated based on petrographic observations and geochemical analyses, with an emphasis on the temporal relationships among dolomitization, pore formation, and multistage hydrothermal fluid activities determined by in situ U-Pb dating. The $\delta^{18}O$, $\delta^{13}C$, and $^{87}Sr/^{86}Sr$ data indicate that the genesis of pre-hydrothermal dolomites and the earliest-formed dolomite cement (Cd1) closest to the edges of pores were related to coeval seawater. The U-Pb age of pre-hydrothermal dolomites is 427 ± 11 Ma, representing the time when early dolomitization occurred. The original pore formation predates the precipitation of Cd1 with a U-Pb age of 391 ± 12 Ma. Stage I and stage II hydrothermal fluids were derived from the Precambrian basement and the mantle, respectively, as evidenced by differences in $\delta^{18}O_{fluid}$ values and rare earth element characteristics. Stage I and II hydrothermal fluids occurred at 161 ± 12 Ma and 81 ± 16 Ma, respectively. Therefore, early dolomitization and pore formation are not correlated with the two stages of hydrothermal fluids. Stage II hydrothermal fluids contained a relatively higher amount of H_2S than stage I hydrothermal fluids. H_2S-related dissolution caused by stage II hydrothermal fluids mainly occurred in the dolomite reservoirs adjacent to major faults, and H_2S was gradually consumed as the distance from the major faults increased. The two stages of hydrothermal minerals successively filled most of the spaces in pores and fractures. The influence of multistage hydrothermal fluids on dolomite reservoirs was found to be dominated by precipitation.

1. INTRODUCTION

Hydrothermal dolomites have gained extensive attention globally because of their potential as hydrocarbon reservoirs (Qing and Mountjoy, 1994; Davies and Smith, 2006; Lavoie et al., 2010; Hirani et al., 2018; Koeshidayatullah et al., 2020a). Some cases of dolomite reservoirs that have undergone hydrothermal dolomitization or hydrothermal alteration have been proposed (Lonnee and Machel, 2006; Davies and Smith, 2006; Zhu et al., 2015; Guo et al., 2016; Du et al., 2018; Ahmad et al., 2021). Hydrothermal fluids (at least 10 °C higher than the ambient burial temperatures) are complex geological fluids that interact with surrounding rocks when they infiltrate carbonate reservoirs during burial (White, 1957; Davies, 1997; Al-Aasm, 2003; Machel and Lonnee, 2002; Montes-Hernandez et al., 2016). Hydrothermal fluids have been interpreted as causing dolomitization of limestones at shallow burial depths (Davies and Smith, 2006; Lavoie et al., 2010; Hollis et al., 2017; Mansurbeg et al., 2021; Stacey et al., 2021a) or modifying pre-hydrothermal dolomites (Dong et al., 2013; Zhu et al., 2015; Ahmad et al., 2021; Li et al., 2021). However, whether the influence of hydrothermal fluids on pre-hydrothermal dolomites is mainly dominated by dissolution or precipitation remains controversial (Ehrenberg et al., 2012; Dong et al., 2013; Zhu et al., 2015; Ehrenberg and Bjørlykke, 2016; Guo et al., 2021; Li et al., 2021).

The following views on the influence of hydrothermal fluids on dolomite reservoirs have been proposed: (1) Precipitation occurs mainly in dolomite reservoirs infiltrated by hydrothermal fluids, causing a reduction in the porosity and permeability (Katz et al., 2006; Ehrenberg et al., 2012; Biehl et al., 2016; Ehrenberg and Bjørlykke, 2016; Li et al., 2021; Pan et al., 2021). (2) Dissolution mainly occurs in dolomite reservoirs infiltrated by hydrothermal fluids at certain temperatures and pressures, causing an increase in porosity and permeability (Jin and Yu, 2011; Martín-Martín et al., 2015; Zhu et al., 2015; Liu et al., 2017; Mansurbeg et al., 2016; Montes-Hernandez et al., 2016). Silicon-rich and fluorine-bearing hydrothermal fluids exhibit strong dissolution abilities (Montañez, 1994; Gigoux et al., 2016; Guo et al., 2021; Su et al., 2021; Jia et al., 2022). The activity of hydrothermal fluids is episodic, which results in a cyclic dissolution ability (acidity) (Wierzbicki et al., 2006). (3) The influence of hydrothermal fluids evolves from early precipitation to late dissolution or from early dissolution to late precipitation, with variations in temperature, pressure, pH, and ion concentration (Wei et al., 2017; Du et al., 2018; Jiu et al., 2020; Chen et al., 2022).

The reason for a lack of consensus on this topic is that the contribution of hydrothermal fluids to dolomite reservoirs is difficult to accurately evaluate. First, dolomite reservoirs are affected by a variety of geological fluids and undergo complex diagenetic modifications (Loucks, 1999; Cai et al., 2001; Lavoie et al., 2010; Zhou et al., 2018). Second, the phenomena observed in petrography can be interpreted in various ways (Ehrenberg et al., 2019), leading to limited geochemical analysis by petrographic observations. For example, the phenomenon of hydrothermal minerals in pores/vugs can be explained either by the formation of pores/

[†] wyzh@upc.edu.cn

GSA Bulletin; https://doi.org/10.1130/B37150.1; 18 figures; 5 tables.

vugs first by hydrothermal dissolution, where spaces are later filled by hydrothermal minerals (Zhu et al., 2015; Mansurbeg et al., 2016; Guo et al., 2021), or the inheritance of pores/vugs from earlier precursor limestones or dolomites, where spaces are directly filled by hydrothermal minerals (Loucks, 2003; Ehrenberg et al., 2012; Ehrenberg and Bjørlykke, 2016). The reason for the multiplicity of interpretations is that the temporal relationships among dolomitization, pore formation, and hydrothermal fluid activity have not been precisely established. Recently, in situ U-Pb dating has been widely used to study diagenetic fluids and pore evolution in dolomite reservoirs (Roberts et al., 2017; Shen et al., 2019; Woodhead and Petrus, 2019; Pan et al., 2020; Mansurbeg et al., 2021; Yang et al., 2022), providing a new method for determining the temporal relationships among dolomitization, pore formation, and hydrothermal fluid activity.

In recent years, activity in the Shengli oilfield has focused on exploring the inner dolomite reservoirs of the Lower Ordovician Yeli-Liangjiashan Formation in the Jiyang subbasin, Bohai Bay Basin (Li et al., 2016; Zhang et al., 2022). Dolomite reservoirs in the Yeli-Liangjiashan Formation experienced multistage hydrothermal fluid activities (Lin, 2006; Li et al., 2016; Xu et al., 2017; Guo, 2021) and developed typical hydrothermal minerals, which are representative of the influence of multistage hydrothermal fluids on dolomite reservoirs. The objectives of this study were: (1) to clarify the stages and characteristics of hydrothermal fluids based on petrographic observations and geochemical analyses; (2) to establish the temporal relationships among dolomitization, pore formation, and multistage hydrothermal fluid activities based on in situ U-Pb dating of carbonate minerals; and (3) to reveal whether the influence of late multistage hydrothermal fluids on dolomite reservoirs was predominantly dissolution or precipitation. This research is helpful in resolving the controversy regarding the influence of hydrothermal fluids on dolomite reservoirs.

2. GEOLOGICAL SETTING

The Bohai Bay Basin is located on the eastern coast of China (Fig. 1A) and consists of six subbasins: Liaodong, Bozhong, Jiyang, Huanghua, Jizhong, and Linqing (Fig. 1B; Liu et al., 2016). The Chengdao-Zhuanghai area, with an area of ~500 km^2, is located between the Bozhong subbasin to the northeast and the Jiyang subbasin to the southwest (Fig. 1B; Luo et al., 2021) and is adjacent to the Shanan Sag to the north, Gunan Sag to the south, Chengbei Sag to the west, and Zhuangdong Sag to the east (Fig. 1C). In addition, the Chengdao-Zhuanghai area is close to the Tanlu strike-slip fault zone, which is the largest strike-slip fault in eastern China (Fig. 1B; Li et al., 2006; Wang et al., 2022a).

The study area has undergone multistage tectonic movements since the Paleozoic, including Caledonian, Hercynian, Indosinian, Yanshanian, and Himalayan movements (Li et al., 2006; Song et al., 2019; Luo et al., 2021; Lin et al., 2021). Five major faults have developed in the study area: the Chengbei fault, Chengbei 20 fault, Chengbei 30 North fault, Chengbei 30 South fault, and Chengnan fault (Figs. 1D and 1E). The tectonic movements in the study area are mainly divided into three stages (Zong et al., 1999; Yang et al., 2012). (1) Indosinian movement stage: At the end of the Triassic, the study area was under NE-SW compressive stress caused by the left-lateral strike-slip movement of the Tanlu fault, forming the basic structural framework and several NW thrust faults (Wu et al., 2005; Xiao et al., 2019; Cheng et al., 2023). (2) Yanshanian movement: During the Jurassic and Cretaceous, the left-lateral strike-slip motion of Tanlu fault zone generated NW extrusion pressure and NE tension in the study area (Luo et al., 2021). The major faults that formed during the Indosinian movement were reactivated and penetrated deep thermal sources (Song et al., 2019; Wang et al., 2022a; Cheng et al., 2023). The major faults then experienced a negative tectonic inversion from compression to extension and converged southward in a broom shape (Fig. 1D; Song et al., 2019). (3) Himalayan movement: During the Cenozoic, major faults were inherited based on fault development during the Mesozoic (Liu et al., 2019). Under the right-lateral strike-slip stress regime on the Tanlu fault, the study area experienced nearly N-S strike-slip-extension movement, and conjugate strike slip on NE- and NW-trending fault systems was formed (Luo et al., 2021; Liu et al., 2022). The Yanshanian and Himalayan movements were the main developmental stages of normal and strike-slip faults (Li et al., 2006; Ye et al., 2019; Cheng et al., 2023). Multiple magmatic intrusions and volcanic eruption events occurred in the study area, mainly during the Mesozoic (Jin et al., 2012; Li et al., 2016; Wang and Li, 2017).

The Lower Paleozoic section in the study area consists of Cambrian and Ordovician strata. The Ordovician section is divided into four formations, from bottom to top: Yeli, Liangjiashan, Majiagou, and Badou Formations (Fig. 2; Tian et al., 2021). From the late Caledonian to the early Hercynian, the study area was uplifted and subjected to erosion, which resulted in a lack of Upper Ordovician to Devonian strata (Li et al., 2004; Zhang et al., 2015). Seawater retreated because of seabed uplift during the sedimentary period of the Ordovician Yeli-Liangjiashan Formation, the sea area gradually narrowed, and the sedimentary environment changed from a vast shallow sea to a limited sea, which caused extensive dolomitization (Ma et al., 1998; Liu et al., 1999; Song, 2001). The Yeli-Liangjiashan Formation in the study area is composed mainly of limestones, argillaceous limestones, dolostones, dolorudstones, and argillaceous dolostones (Fig. 2). As for the burial history of the Yeli-Liangjiashan Formation, at the end of the Permian and before the start of the Indosinian movement, the Yeli-Liangjiashan Formation reached a maximum burial depth of nearly 5000 m and a maximum stratigraphic temperature of ~180 °C. At the end of the Indosinian movement, the Yeli-Liangjiashan Formation was uplifted to a depth of nearly 1100 m, while the burial temperature dropped to ~60 °C. By the Late Cretaceous, the strata were again starting to be continuously buried and reached the present depth of ~3000–4000 m, with the present measured temperature of the strata being from 128 °C to 153 °C (average 140 °C).

3. METHODOLOGY

Approximately 200 representative dolostone samples with diameters of 2.5 cm and lengths greater than 5 cm were collected from the Yeli-Liangjiashan Formation in the study area. All the analytical samples were obtained from oilfields. Six wells were used for the intensive sampling and key research (Fig. 1D). The top of the Yeli-Liangjiashan Formation in these six wells is more than 350 m on average from the Ordovician top unconformity, which minimizes the influence of meteoric water on dolomite reservoirs.

To analyze the mineralogy, diagenesis, and pore/fracture characteristics, 178 polished and cast thin sections were prepared and stained with Alizarin Red S to differentiate calcite from dolomite (Dickson, 1966), and 62 cathodoluminescent (CL) thin sections were prepared. Optical observations were performed using a Zeiss Axioscope A1 APOL digital transmission microscope. CL analysis was performed using a CAMBRIDGE CL8200 MK5 detector on a Zeiss microscope. The operating conditions for the CL microscope were set to 15 kV and 400 μA. Ten typical core samples plated with platinum were prepared to accurately observe the crystal morphology and dissolution using a Coxem-30^{plus} scanning electron microscope (SEM). The Coxem-30^{plus} SEM was integrated with a Bruker energy-dispersive X-ray analysis system (XFlasher Detector 430-M), which allowed the analysis of a spot ~1 μm in diameter.

In total, 43 thin sections with a thickness of 80 μm were prepared to conduct fluid inclusion

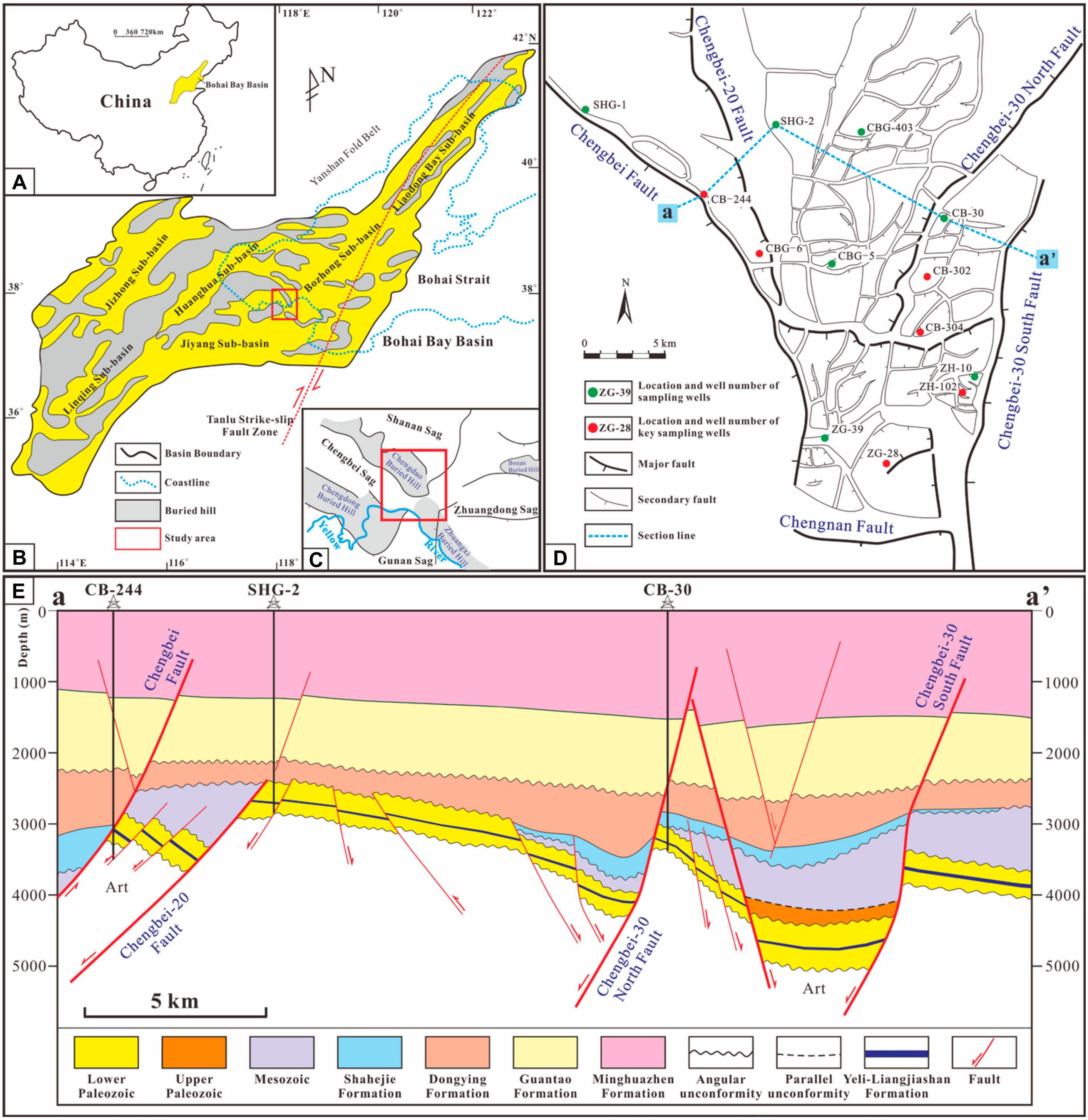

Figure 1. (A) Location of Bohai Bay Basin in China. (B) Structural map of Bohai Bay Basin showing distribution of main subbasins (Liu et al., 2023). Red box indicates location of the study area. (C) Distribution of the buried hills and Cenozoic sags in the study area (Xu et al., 2017). (D) Structural map of the Chengdao-Zhuanghai area showing major and secondary faults and locations of main wells (Lin et al., 2021). (E) Section a–a′ provides the reconstructed tectonostratigraphic framework showing the major unconformities, faults, wells, and Lower Paleozoic strata.

studies. The petrography of the fluid inclusions was characterized in detail using transmitted light and ultraviolet fluorescence microscopy. Homogenization temperature measurements were performed using a Linkam TH-600 heating-cooling stage. The measured temperature precision was ±0.5 °C. A laser Raman test was performed to analyze the vapor-phase composition of the liquid-vapor two-phase aqueous inclusions (LVAIs)

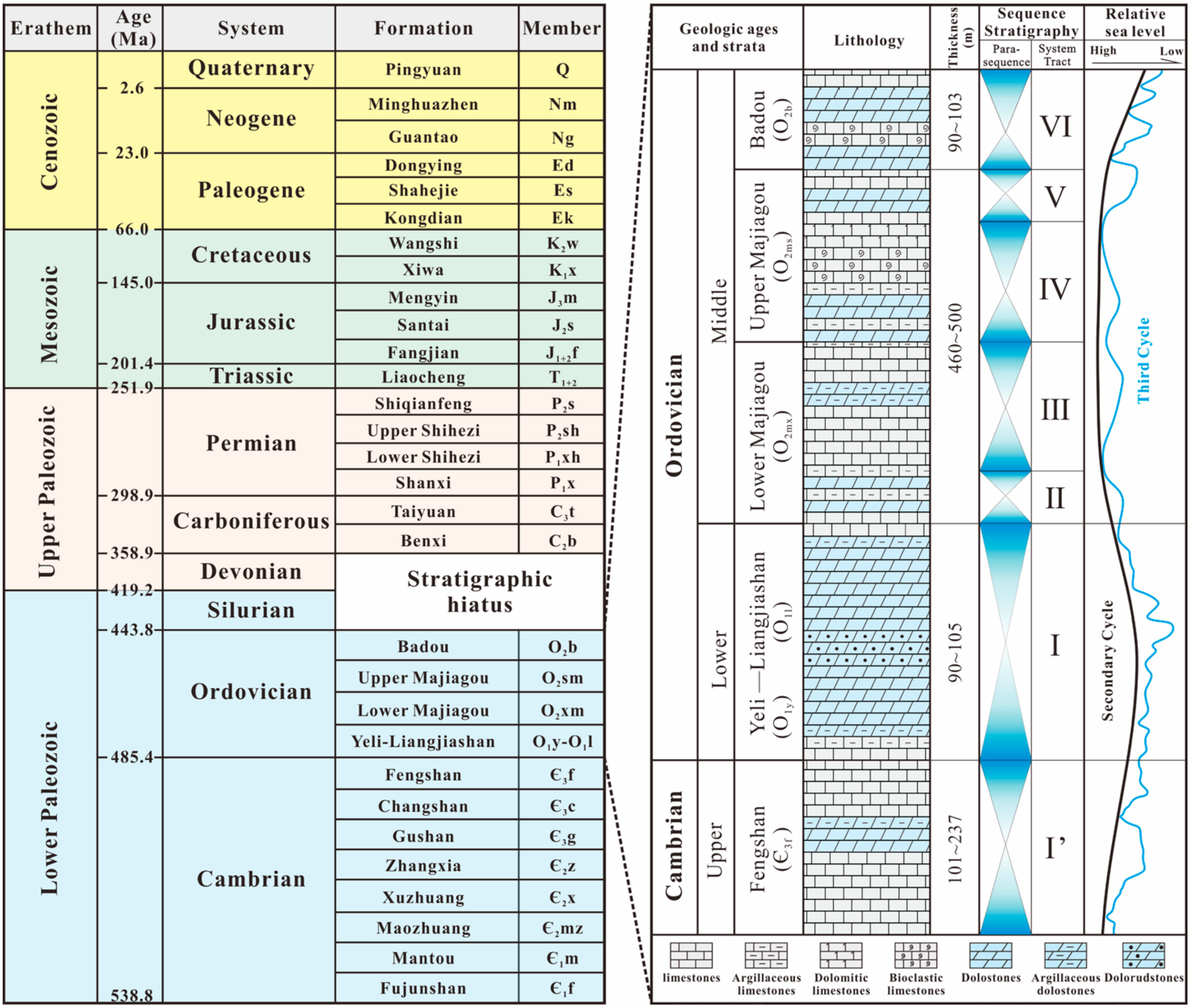

Figure 2. Comprehensive stratigraphic column from the Fengshan to Badou Formations. Stratigraphic development sequence is modified from Liu et al. (2023), relative sea-level changes refer to Liu et al. (1999), and sequence stratigraphy refers to Ma et al. (1998).

using a micro-Raman spectrometer (Renishaw inVia) with a 514 nm excitation light source.

For oxygen (O) and carbon (C) isotope analysis of different types of carbonate minerals, 18 thin sections with a thickness of 100 μm were prepared to obtain a powder of carbonate minerals by microdrilling (Marathon BM50M). The purity of the powder samples reached nearly 100% using microdrilling sampling. The C and O isotope analysis on microdrilling powder samples (5 mg) was performed on a MAT253 Plus isotope ratio mass spectrometer at a temperature of 26 °C and a relative humidity (RH) of 60% RH. The error for C isotopes was ±0.003‰, and the error for O isotopes was ±0.051‰. Here, $10^3 \ln\alpha_{\text{dolomite-fluid}} = 3.2 \times 10^6/T^{-2} - 3.3$ and $10^3 \ln\alpha_{\text{calcite-fluid}} = 2.78 \times 10^6/T^{-2} - 2.89$ were used to determine the fluid $\delta^{18}O$ values in the dolomite-fluid and calcite-fluid system, respectively (Land, 1983; Friedman and O'Neil, 1977).

In total, 40 thin sections with a thickness of 100 μm were prepared to obtain in situ trace-element data. Representative thin sections were subjected to laser ablation–inductively coupled plasma–mass spectrometry (LA-ICP-MS) analysis. Laser sampling was performed using a GeoLasPro laser system and Agilent 7900 ICP-MS. The operating conditions for the laser included a repetition rate of 5 Hz and an energy density of 5 J/cm². Each analysis spot size was 44 μm with a background acquisition of ~20 s (gas blank) followed by data acquisition of 50 s. For details of calibration methods and data processing, refer to Liu et al. (2008) and Chen et al., (2011). Rare earth element (REE) concentrations were normalized to post-Archean Australian shale (PAAS; Taylor and McLennan, 1985). Normalized REE anomalies were quantified following the methods of Bau and Dulski (1996) and Lawrence et al. (2006) and were defined as follows: $Ce_N/Ce^*_N = Ce_N/(2Pr_N - Nd_N)$, $Eu_N/Eu^*_N = Eu_N/(0.67Sm_N + 0.33Tb_N)$, and $Pr_N/Pr^*_N = Pr_N/(0.5Ce_N + 0.5Nd_N)$.

Fourteen sections with a thickness of 100 μm were prepared to obtain the in situ Sr isotopic

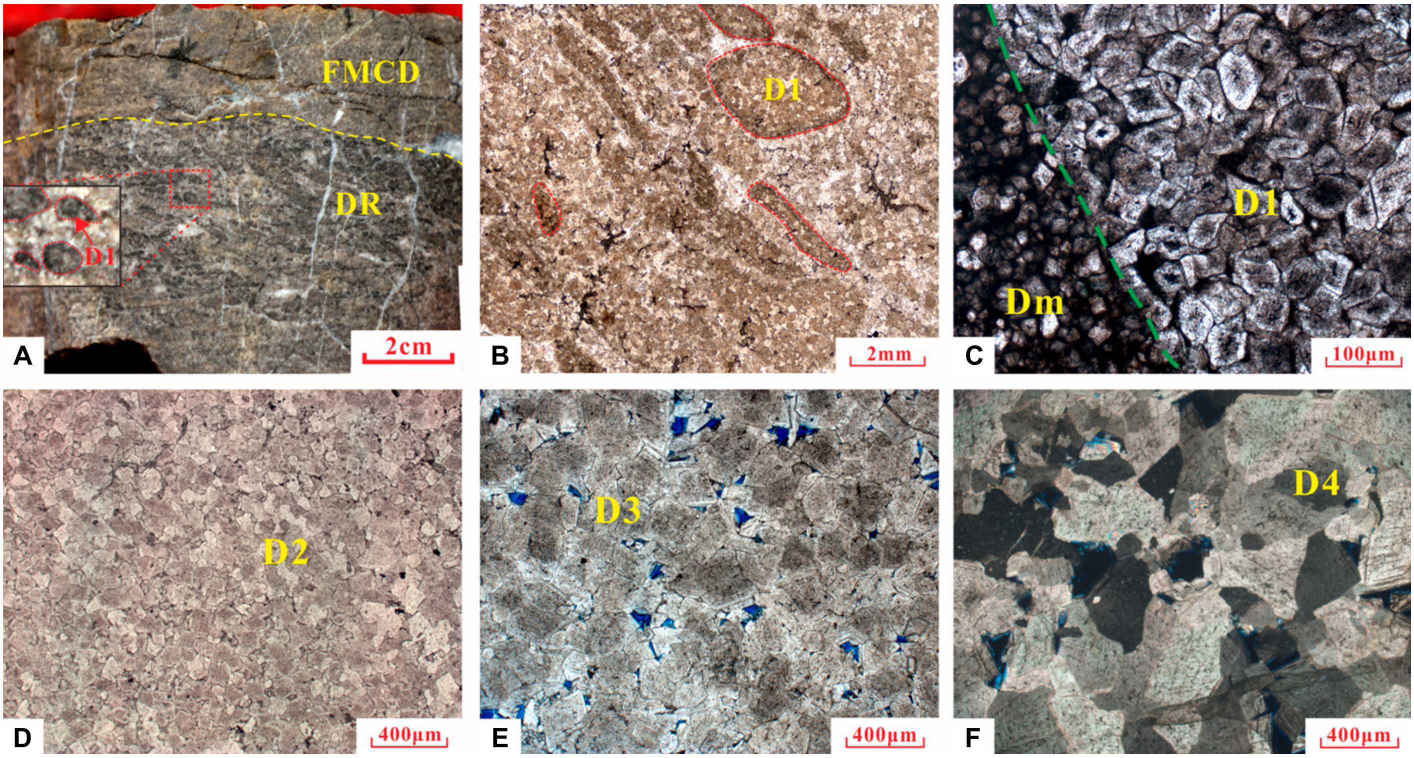

Figure 3. Petrological characteristics of dolorudstones and three types of nonmimic dolostones. (A) Core photograph of dolorudstones (DR), showing a distinctive granular morphology. Red lines indicate relict grains of dolorudstones (D1). Yellow dashed line is the boundary between fine to medium crystalline dolostone (FMCD) and DR. Well CB244, 2920.6 m. (B) Photomicrograph of D1 in part A, displaying very fine to fine dolomite crystals and apparently granular morphology. Red lines indicate relict grains. Well CB244, 2920.6 m, plane-polarized light (PPL). (C) Photomicrograph showing the planar euhedral (planar-e)/planar subhedral (planar-s) crystals of D1, and dolomitic mud (Dm) distributing among the relict grains. Well ZG28, 4137.93 m, PPL. (D) Photomicrograph of D2, showing fine euhedral to subhedral crystals. Well ZG28, 4122.92 m, PPL. (E) Photomicrograph of D3, showing fine to medium, subhedral to anhedral crystals. Well CB302, 4005.26 m, PPL. (F) Photomicrograph of D4, showing medium to coarse, nonplanar-anhedral (nonplanar-a) crystals, and a sharp to slightly wavy extinction. Well ZH102, 4622.66 m, cross-polarized light (XPL).

values of the carbonate minerals. Measurements were conducted using a Nu Plasma III multi-collector (MC) ICP-MS attached to a RESOlution-155 193 nm ArF laser-ablation system. The operating conditions were as follows: 30 s baseline time, 40 s ablation time, 60 μm spot size, 6 Hz repetition rate, and 6 J/cm^2 energy density. Calibration methods and data processing followed the method described by Ramos et al. (2004) and were fully addressed by Gao and Zhou (2013).

To determine the timing of the carbonate minerals, 10 thin sections with a thickness of 100 μm were prepared for in situ U-Pb dating. Representative thin sections were obtained using a GeoLasPro 193 nm ArF excimer laser-ablation system coupled with a Thermo Fisher Scientific quadrupole for mass spectrometry detection. The operating conditions of the laser included a repetition rate of 10 Hz and an energy density of 5 J/cm^2. Each analysis spot size was 90 μm, with a background acquisition of ~20 s (gas blank) followed by data acquisition of 40 s. Details of the calibration methods and data processing were provided in Roberts et al. (2017) and Tang et al. (2020).

Thin-section preparation, microdrilling sampling, optical observations, CL analyses, SEM analyses, petrographic observations, homogenization temperature measurements of fluid inclusions, and stable C and O isotope determinations were performed at the Key Laboratory of Deep Oil and Gas, Ministry of Education, China University of Petroleum, Qingdao, China. U-Pb dating, Sr isotopic analyses, and trace-element analyses were conducted at the State Key Laboratory of Ore Deposit Geochemistry, Institute of Geochemistry, Chinese Academy of Sciences, Guiyang, Guizhou Province, China.

4. RESULTS

4.1. Petrography

4.1.1. Lithology

The dolostone types of the Yeli-Liangjiashan Formation primarily include both fabric-preserving and fabric nonmimic varieties (Sibley and Gregg, 1987). The fabric-preserving types are mainly dolorudstones (DR). The relict grains of the dolorudstones (D1) show a distinct grain morphology at the core scale, with the size of the relict grains varying from 2 mm to 10 mm (Fig. 3A). In the interior of D1, the dolomite crystals are mostly 40–170 μm in size and characterized by planar euhedral (planar-e) to planar subhedral (planar-s) textures (Figs. 3B and 3C). Dolomitic mud (Dm) with crystals less than 10 μm in size is distributed among the relict grains (Fig. 3C).

Based on petrographic observations of crystal size, distribution, and crystal plane shape and according to the classification scheme of Sibley and Gregg (1987), three types of nonmimic dolostones were recognized: fine crystalline dolostone (FCD), fine to medium crystalline dolostone (FMCD), and medium to coarse crystalline dolostone (MCCD). D2, D3, and D4 refer to the matrices of FCD, FMCD, and MCCD, respectively. The crystal size of D2 with planar-e

Figure 4. Petrological characteristics of dolomite cements in pores and fractures (Cd1: A–D, Cd2: E–H, SD: I–L). (A) Photomicrograph of earliest-formed dolomite cement (Cd1) with planar euhedral (planar-e) texture. Red dashed lines are the boundary between Cd1 and D3. Well CB302, 4007.76 m, plane-polarized light (PPL). (B) Cathodoluminescence (CL) photomicrograph of the yellow dashed box in part A. Cd1 shows red to shiny red luminescence, and D3 shows red to dull-red luminescence. Yellow dashed lines are the boundary between Cd1 and D3. Well CB302, 4007.76 m. (C) Backscattered electron (BSE) image of Cd1 growing around D3. Well CB302, 4002.36 m. (D) Scanning electron microscope (SEM) image showing euhedral Cd1 around pore. Yellow dashed lines are the boundary between Cd1 and D3. Well CB302, 4002.36 m. (E) Photomicrograph of Cd2 as clear overgrowth rims. Well CB302, 4005.45 m, PPL. (F) Magnified view of red dashed box in part E, showing Cd2 as clear overgrowth rims around Cd1. Green dashed lines are the boundary between Cd1 and D3, red dashed lines are the boundary between Cd2 and Cd1, and yellow dashed lines are the boundary of Cd2. (G) BSE image of Cd2 growing around Cd1. Well ZH102, 4623.26 m. (H) CL photomicrograph of Cd2 displaying nonluminescent to very dull-red luminescence under CL. Well CB302, 4005.45 m. (I) Core photograph of saddle dolomite (SD) growing along two sides of the fracture. Well ZG28, 4123.42 m. (J) Photomicrograph showing SD growing along the edge of the fracture. Well ZG28, 4123.42 m, PPL. (K) CL photomicrograph of image in part J, where SD displays nonluminescent to very dull-red luminescence. (L) Photomicrograph of SD with curved crystal plane and wavy extinction. Well ZG28, 4122.92 m, cross-polarized light (XPL). P—pore; C1—the first type of calcite; D1—relict grains of the dolorudstones; D2, D3, and D4—matrices of fine crystalline dolostone (FCD), fine to medium crystalline dolostone (FMCD), and medium to coarse crystalline dolostone (MCCD), respectively.

to planar-s textures varied from 70 μm to 250 μm (Fig. 3D). The crystal size of D3 with planar-s to planar-anhedral (a) textures varied from 100 μm to 400 μm (Fig. 3E). D4 exhibited nonplanar textures with sharp to slightly wavy extinction under cross-polarized light (XPL), and the crystal size of D4 was greater than 250 μm (Fig. 3F). The nonmimic dolostones are the most abundant type in the formation, accounting for ~80% of the total dolostones in the Lower Ordovician Yeli-Liangjiashan Formation.

4.1.2. Dolomite Cements

The earliest-formed dolomite cement (Cd1). Cd1, with a crystal size of 20–120 μm, mainly overgrows around the D3 type dolomite in the form of a clean ring-band structure, and it shows a planar-e texture under plane-polarized light (PPL; Fig. 4A). Cd1 displays red to shiny red luminescence under CL (Fig. 4B). Cd1 is distributed around the pores/vugs and is the first phase of cement closest to the edges of the pores (Figs. 4A and 4C). Cd1 is characterized by a smooth crystal plane and a complete crystal morphology under SEM (Fig. 4D). Furthermore, Cd1 mostly developed in the FMCD.

Dolomite cement adjacent to Cd1 (Cd2). Cd2 mainly overgrows around Cd1 in the form of a clean ring-band structure (Figs. 4E–4G). The crystals of Cd2 are planar and range from 50 μm to 250 μm in size. Cd2 displays nonluminescent to very dull-red luminescence under CL (Fig. 4H). Cd2 also fills the fractures and is closest to the walls of the fractures. Additionally, Cd2 mainly developed in dolomite reservoirs away from major faults, such as in well CB302.

Saddle dolomite (SD). SD consists of medium to coarse crystalline, nonplanar-a dolomite rhombs, ranging from 300 μm to 800 μm in size. SD grows along both sides of the fractures (Figs. 4I and 4J). These crystals show typical features of saddle dolomite with a distinctively curved crystal plane and wavy extinction under XPL (Figs. 4J, 4L, and 5A). SD displays nonluminescent to very dull-red luminescence under CL (Fig. 4K). Additionally, the dissolution of the SD in the fractures can be clearly observed (Fig. 5), and calcite and quartz fill some of the dissolution pores of the SD (Figs. 5A and 5B). SD mainly developed in dolomite reservoirs adjacent to major faults, such as in well CB244.

4.1.3. Calcite and Quartz

There are two types of calcite in the Lower Ordovician Yeli-Liangjiashan Formation, which occur as coarsely crystalline spar-filling fractures and pores. The first type of calcite (C1), with a cloudy crystal surface, is characterized by subhedral to anhedral coarse crystalline crystals over 400 μm in size (Fig. 6A). C1 displays bright-orange to yellow luminescence under CL (Fig. 6B). The second type of calcite (C2) exhibits a euhedral crystal plane and bright-orange to dull-yellow luminescence under CL (Figs. 6A and 6B). C1 is closer to the walls of the fractures than C2 (Fig. 6C). In the fractures, C1 precipitated after Cd2 (Fig. 6D) and filled the dissolution pores of the SD (Fig. 5A). Moreover, C1 filled the intercrystalline pores after the precipitation of Cd1 and SD/Cd2 (Figs. 6E and 6F).

Quartz (Qz) is characterized by euhedral crystals 30–150 μm in size (Figs. 7A and 7B) and exhibits a hexagonal bipyramidal crystal morphology (Figs. 7C and 7D). Qz is pervasive in fractures and intercrystalline pores (Figs. 7A and 7B) and partially fills the dissolution pores of the SD (Figs. 7E–7H). Moreover, Qz is always associated with barite or pyrite (Figs. 7B–7D).

4.1.4. Pores

Three types of pores, intercrystalline pores, vugs, and dissolution pores, developed in the dolomite reservoirs of the Lower Ordovician Yeli-Liangjiashan Formation. All these pore types mainly developed in the FMCD. The dolomite crystals around the intercrystalline pores (Figs. 8A–8C) and vugs (Figs. 8D–8E) are euhedral with a flat crystal plane. SD filled the vugs following the precipitation of Cd1 (Figs. 8F–8H). The dissolution pores of the SD appear to be embayed (Figs. 5B and 5C) and are most common in the fractures (Fig. 5).

4.1.5. Microfractures

Microfractures are generally defined as fractures less than 100 μm in width (Anders et al., 2014). The microfractures in the Lower Ordovician Yeli-Liangjiashan Formation can be divided into two stages. The first-stage microfractures (Mf-I) are filled with Cd2 (Figs. 9A and 9B). The second-stage microfractures (Mf-II), cutting Mf-I, are mostly filled with C1 (Figs. 9A and 9B). The pores connected by Mf-I always developed Cd2 (Figs. 9C and 9D), while the pores not connected by Mf-I did not develop Cd2 (Fig. 9E). The walls of Mf-II can be observed to be uneven due to dissolution (Fig. 9F). Moreover, because of the Mf-II connecting pores, the SD in the pores was affected by the erosive fluids, resulting in crystal plane deformation and unevenness (Figs. 9F–9H).

4.2. Geochemistry

4.2.1. Trace Elements

The contents of Mn and Fe in D1 are relatively low, with an average of 16.5 ppm and 1160.4 ppm, respectively. The Mn and Fe contents in D2 are relatively moderate, with averages of 84 ppm and 1455 ppm, respectively. D3 is characterized by relatively moderate contents of Mn and Fe, with an average of 76.1 ppm and 1784.5 ppm, respectively. D4 is characterized by relatively low contents of Mn and Fe, with an average of 47.8 ppm and 956.3 ppm, respectively. Cd1 is characterized by higher

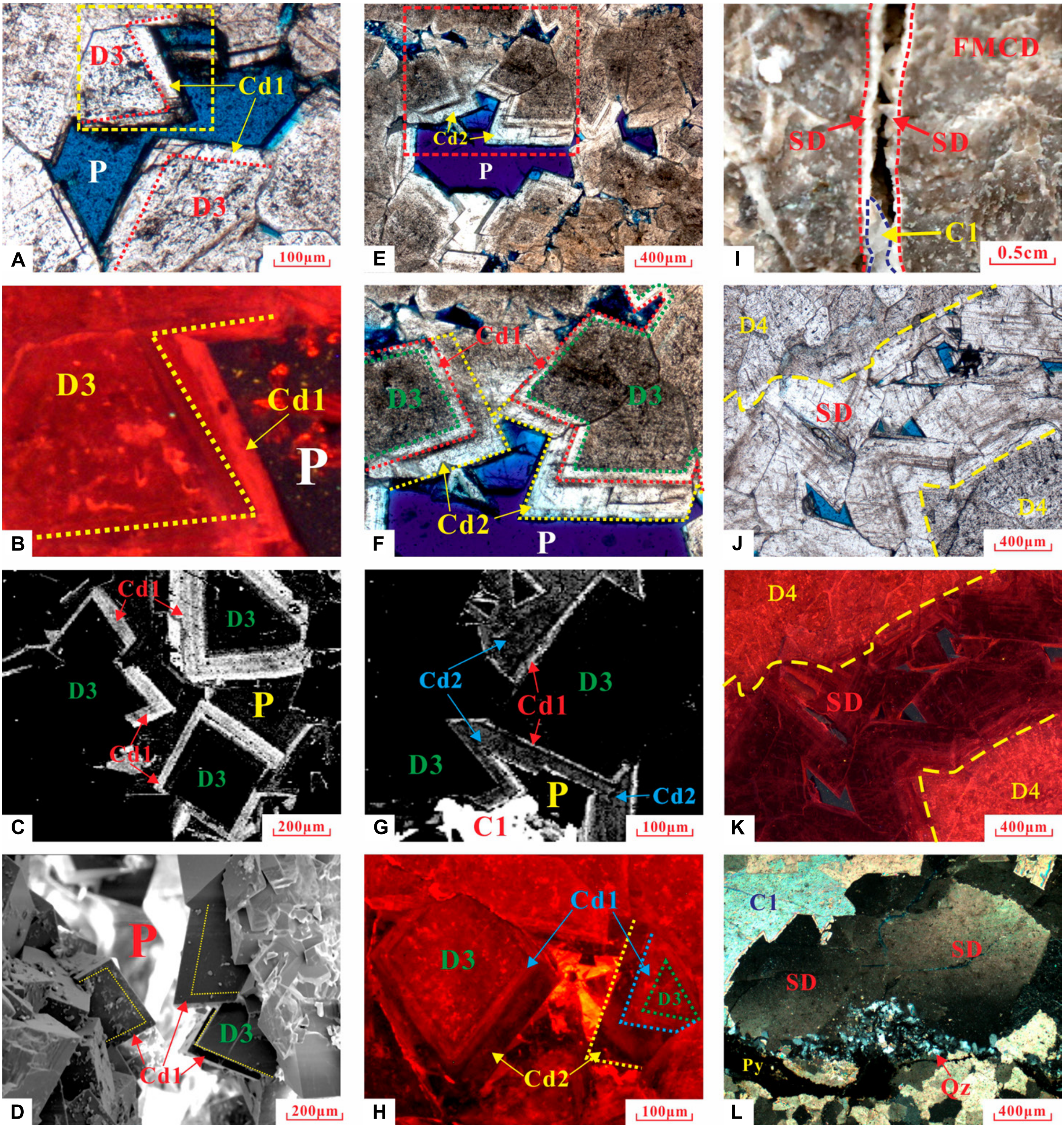

Mn content and Fe content with an average of 111.2 ppm and 2872.1 ppm, respectively. The average contents of Mn and Fe in Cd2 are 349.5 ppm and 18,537.1 ppm, respectively. The average contents of Mn and Fe in SD are 422.0 ppm and 16,497.7 ppm, respectively. The Fe and Mn contents of Cd2 and SD are much higher than those of D1, D2, D3, D4, and Cd1 (Fig. 10A).

4.2.2. Rare Earth Elements

D1 displays distinguished negative Ce anomalies from 0.28 to 0.40 and is within the seawater quadrant of the Ce/Ce* versus Pr/Pr* plot (Fig. 10B). D1 is characterized by depletion of light REEs (LREEs; Fig. 10C). The REE patterns of D1 are comparable to those of seawater, including prominent negative Ce anomalies (Fig. 11A).

D2, D3, D4, and Cd1 exhibit flat REE patterns (Figs. 11A and 11B) and are characterized

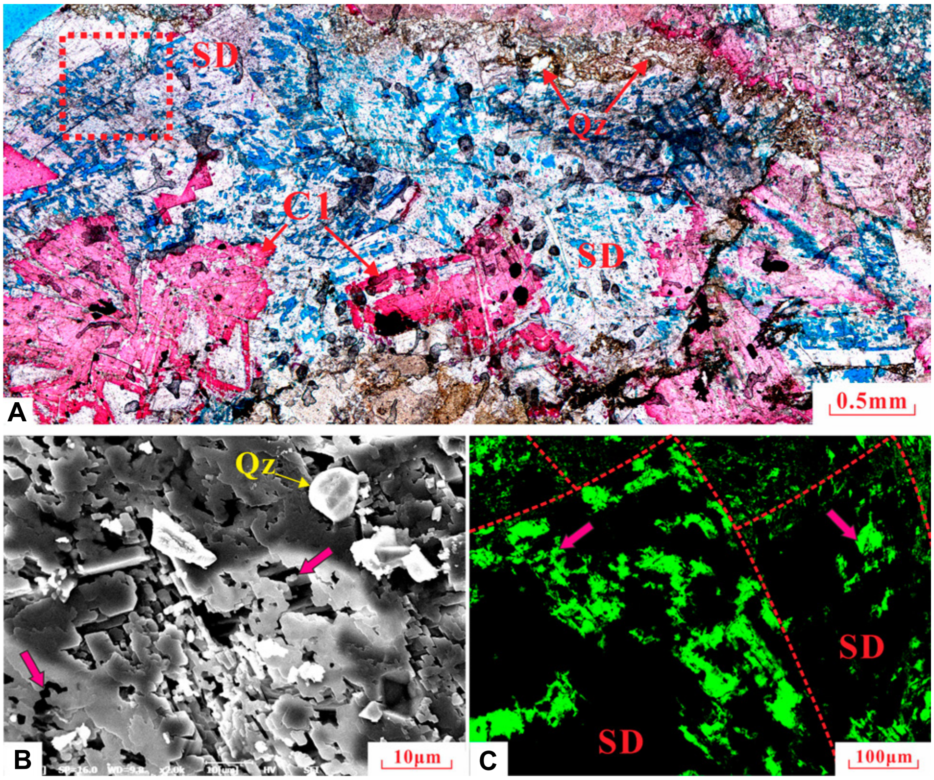

Figure 5. (A) Multiview collage showing the dissolution of saddle dolomite (SD) in a fracture, where C1 fills in part of the dissolution pores of SD. Well CB244, 2914.37 m, plane-polarized light (PPL). (B) Photomicrograph of SD indicated by red dashed box in part A, where dissolution pores (pink arrows) are preserved in SD, and Qz fills in dissolution pores. Scanning electron microscope image. (C) Laser scan confocal photomicrograph of SD, where red dashed line is the boundary of SD, and green areas represent dissolution pores (pink arrow) preserved in SD. Well CB244, 2914.37 m. C1—the first type of calcite; Qz—quartz.

by enrichment of LREEs and depletion of middle REEs (MREEs; Table A1 [see Appendix]; Fig. 10C). The ΣREEs in D2, D3, and D4 successively decrease with increasing crystal size (Table A1).

Cd2 and SD are outside the seawater quadrant of the Ce/Ce* versus Pr/Pr* plots (Fig. 10B). Cd2 and SD exhibit very low ΣLREE/ΣMREE ratios (Table A1; Fig. 10C). SD displays distinctively positive Eu anomalies from 0.94 to 2.70, while Cd2 exhibits slightly positive Eu anomalies from 0.94 to 1.42 (Table A1; Fig. 10D). Both Cd2 and SD exhibit extremely low La/Ho ratios (Fig. 10D). The REE patterns of Cd2 and SD are extremely LREE-depleted and exhibit a leftward dip (Fig. 11B).

C1 exhibits significantly positive Eu anomalies from 0.99 to 2.31, and C2 exhibits negative Eu anomalies ranging from 0.72 to 1.00 (Table A2 [see Appendix]; Fig. 10E). In the Yb/La-Yb/Ca cross-plot, C1 is distributed in the range of hydrothermal origin, while C2 is mostly distributed in the range of sedimentary origin (Fig. 10F). Qz displays significantly positive Eu anomalies ranging from 1.20 to 4.75 (Table A3 [see Appendix]; Fig. 10I). The REE patterns of Qz and C1 display a slight MREE bulge and are similar to the hydrothermal fluids of the Mid-Atlantic Ridge (Figs. 11C and 11D).

4.2.3. Carbon and Oxygen Isotopes

The oxygen and carbon isotopic compositions of D1, D2, D3, D4, Cd1, Cd2, SD, C1, and C2 are presented in Table A4 (see Appendix) and are plotted in Figure 12A. The δ^{18}O and δ^{13}C values of D1 range from −7.00‰ to −6.03‰ relative to Vienna Peedee belemnite (VPDB) and 0.07‰ to 1.41‰ VPDB, respectively. The δ^{18}O and δ^{13}C values of D2 range from −5.77‰ to −5.00‰ VPDB and −1.68‰ to 0.07‰ VPDB, respectively. The δ^{18}O and δ^{13}C values of D3 range from −7.17‰ to −6.55‰ VPDB and from −2.15‰ to 0.45‰ VPDB, respectively. As for D4, the δ^{18}O and δ^{13}C values span from −8.50‰ to −7.26‰ VPDB and from −0.66‰ to 0.26‰ VPDB, respectively. The δ^{18}O and δ^{13}C values of Cd1 span from −7.72‰ to −6.28‰ VPDB and from −0.35‰ to 0.44‰ VPDB, respectively. The δ^{18}O and δ^{13}C values of D1, D2, D3, D4, and Cd1 are mostly within the estimated range for carbonate precipitated from the late Cambrian–Early Ordovician coeval seawater.

The δ^{18}O and δ^{13}C values of Cd2 vary from −14.93‰ to −13.41‰ VPDB and from −0.78‰ to −0.43‰ VPDB, respectively. SD exhibits extreme δ^{18}O depletion from −19.15‰ to −17.12‰ VPDB and δ^{13}C from −1.18‰ to −0.40‰ VPDB.

The δ^{18}O and δ^{13}C values of C1 span from −18.24‰ to −14.26‰ VPDB and from −2.27‰ to −1.27‰ VPDB, respectively. The δ^{18}O and δ^{13}C values of C2 span from −15.40‰ to −12.13‰ VPDB and from −2.72‰ to −2.27‰ VPDB, respectively.

4.2.4. Strontium Isotopes

The ^{87}Sr/^{86}Sr ratios are presented in Table A5 (see Appendix) and Figure 12B. The ^{87}Sr/^{86}Sr ratios of D3, D4, and Cd1 range 0.70883–0.70890, 0.70907–0.70925, and 0.70885–0.70901, respectively, which overlap with the estimated ^{87}Sr/^{86}Sr ratio range for carbonate precipitated from the late Cambrian–Early Ordovician coeval seawater.

The ^{87}Sr/^{86}Sr ratios of Cd2, SD, C1, and C2 range 0.71455–0.71482, 0.71472–0.71496, 0.71670–0.71692, and 0.71459–0.71562, respectively, which are much higher than those of D3, D4, and Cd1 and significantly deviate from the ^{87}Sr/^{86}Sr ratios of coeval seawater.

4.2.5. In Situ U-Pb Dating

The U-Pb Tera-Wasserburg concordia diagrams for D3, D4, Cd1, SD, C1, and C2 are shown in Figure 13. Uncertainties on the U-Pb ages of dated samples are given at 2σ. The ^{207}Pb/^{206}Pb and ^{238}U/^{206}Pb ratios of D3 define a linear array on the Tera-Wasserburg concordia diagram, generating an intercept age of 427 ± 11 Ma (mean square of weighted deviates [MSWD] = 1.7; Fig. 13A), corresponding to the Late Ordovician to Early Devonian (Caledonian period). The U-Pb age of D4 is 310 ± 17 Ma (MSWD = 1.3; Fig. 13B), corresponding to the early Carboniferous to late Carboniferous (Hercynian period). The U-Pb age of Cd1 is 391 ± 12 Ma (MSWD = 1.6; Fig. 13C), which is close to, but later than, the age of D3, corresponding to the Early Devonian to Late Devonian (Hercynian period). The U-Pb age of SD is 161 ± 12 Ma (MSWD = 3.3; Fig. 13D), corresponding to the Middle Jurassic to Late Jurassic (Yanshanian period). The U-Pb age of C1 is 81 ± 16 Ma (MSWD = 3.7; Fig. 13E), corresponding to the Late Cretaceous (Yanshanian period). However, the U-Pb age of C2 is not available (Fig. 13F).

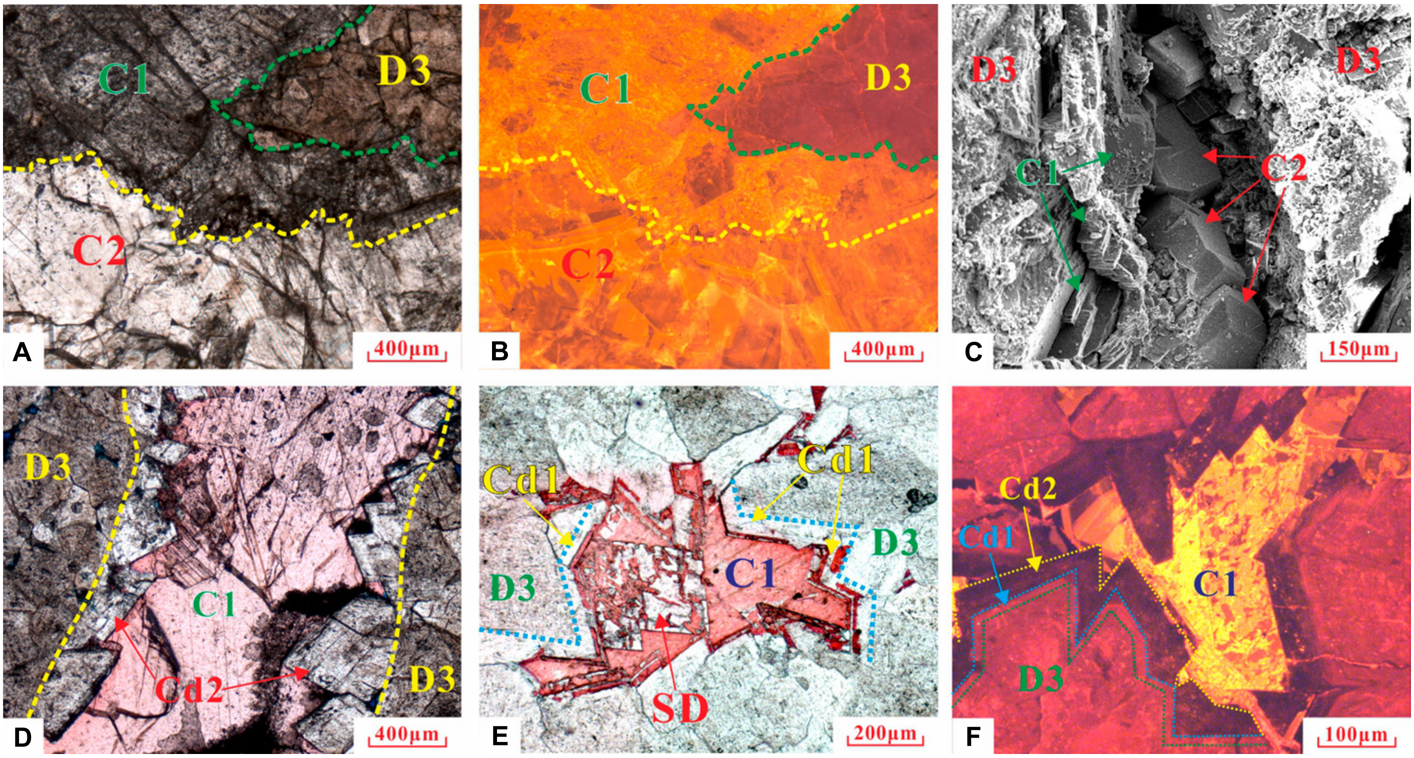

Figure 6. Petrological characteristics of the first type of calcite (C1) and second type of calcite (C2). (A) Photomicrograph of C1 and C2 filling fractures. The fracture wall is outlined by the green dashed line. C1 is adjacent to the fracture wall, and C2, filling the remaining fracture space, is next to C1. Yellow dashed line is the boundary between C1 and C2. Well CB302, 4003.76 m, plane-polarized light (PPL). (B) Cathodoluminescence (CL) photomicrograph of image in part A, showing the bright-orange to yellow luminescence of C1 and the bright-orange to dull-yellow luminescence of C2. Well CB302, 4003.76 m. (C) Photomicrograph of C2 displaying crystal characteristics similar to C1 and filling the remaining fracture space after C1. Well CB302, 4002.36 m, scanning electron microscope image. (D) Photomicrograph of Cd2 (dolomite cement adjacent to Cd1) and C1 successively filling the fracture, where the fracture wall is outlined by the yellow dashed lines. Well CB302, 4007.76 m, PPL. (E) Photomicrograph of C1 filling the intercrystalline pore. Pore was filled successively by earliest-formed dolomite cement (Cd1), saddle dolomite (SD), and C1. Blue dashed lines are the boundary between Cd1 and D3 (matrix of fine to medium crystalline dolostone). Dissolution can be observed in SD and Cd1. Well CB244, 2903.77 m, PPL. (F) Photomicrograph of C1 filling the intercrystalline pore, where the pore was filled successively by Cd1, Cd2, and C1. Yellow dashed lines are the profile of Cd2, blue dashed lines are the profile of Cd1, and green dashed lines are the profile of C1. Well CB302, 4005.45 m, CL.

4.3. Fluid Inclusions

Fluid inclusions in the dolomites, calcites, and quartz were mainly liquid-vapor two-phase aqueous inclusions (LVAIs), which varied in size from ~3.35 μm to 18.76 μm. The vapor phase of LVAIs accounted for ~4%–18% of the total inclusion volume. The LVAIs in D4, Cd2, SD, C1, C2, and Qz were selected to measure the homogenization temperatures. The LVAIs in D4 were isolated (Fig. 14A). The LVAIs in Cd2, SD, C1, C2, and Qz were mostly distributed linearly (Figs. 14B–14F) and can be considered as fluid inclusion assemblages (FIAs; Goldstein and Reynolds, 1994). The LVAIs in D1, D2, D3, and Cd1 were too small to be measured.

The homogenization temperatures of the LVAIs in D3, Cd2, and SD ranged 85.2–95.2 °C, 107.2–168.5 °C, and 142.3–192.5 °C, with average values of 88.9 °C, 138.7 °C, and 166.1 °C, respectively (Fig. 14G). The homogenization temperatures of the LVAIs in C1 and C2 ranged 124.5–178.6 °C and 98.0–141.9 °C, with average values of 141.6 °C and 111.5 °C, respectively (Fig. 14H). The homogenization temperatures of the LVAIs in Qz ranged from 155.4 °C to 179.8 °C, with an average value of 160.1 °C (Fig. 14I).

A laser Raman analysis was performed on the vapor-phase components of the LVAIs (Fig. 15). The results showed that the vapor-phase components of the LVAIs in C1 adjacent to the major faults and Qz contained hydrogen sulfide (H_2S; Figs. 15B, 15D, and 15E). However, there were no distinct H_2S peaks in the LVAIs in C1 away from the major faults or in SD (Figs. 15A and 15C). The intensity of H_2S contained in the vapor-phase components of the LVAIs in C1 adjacent to the major faults ranged from 104.16 counts/s to 319.89 counts/s, while the intensity of H_2S contained in the vapor-phase components of the LVAIs in C1 away from the major faults ranged from 2.64 counts/s to 11.89 counts/s.

5. DISCUSSION

5.1. Stages and Characteristics of Hydrothermal Fluids

Based on the comprehensive analyses of petrography, geochemistry, fluid inclusions, U-Pb dating, and tectonic movements, two stages of hydrothermal fluids were distinguished in the dolomite reservoirs of the Lower Ordovician Yeli-Liangjiashan Formation.

5.1.1. Stage I Hydrothermal Fluids

SD shows typical features of saddle dolomite with distinctive curved crystal faces (Figs. 4J and 4L), suggesting that SD formed in a hydro-

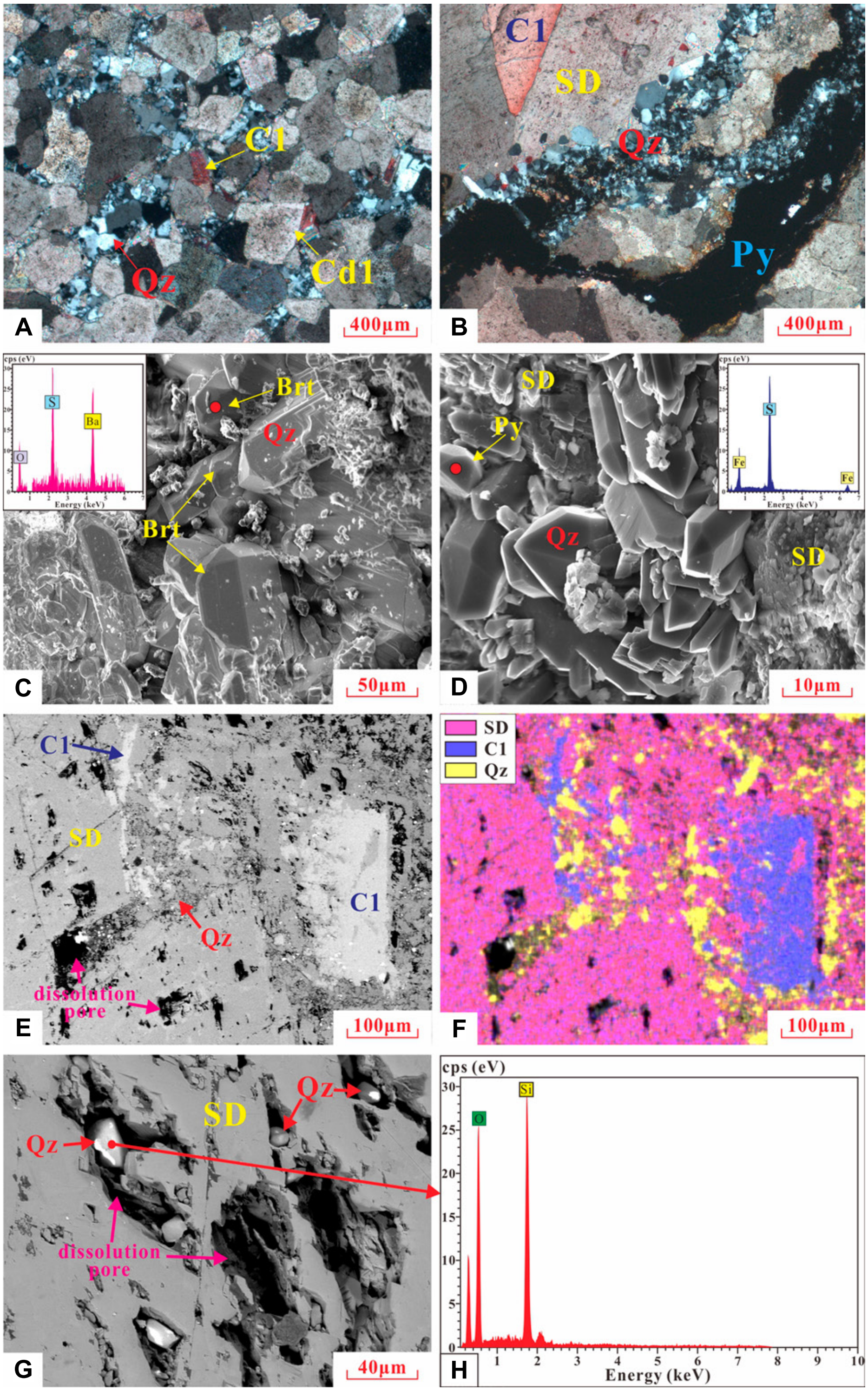

Figure 7. Petrological characteristics of quartz (Qz). (A) Photomicrograph of Qz filling the intercrystalline pores. Well ZG28, 4123.32 m, cross-polarized light (XPL). (B) Photomicrograph of Qz, pyrite (Py), first type of calcite (C1), and saddle dolomite (SD) filling a fracture. Well ZG28, 4122.92 m, XPL. (C) Photomicrograph of barite (Brt) and Qz. Position of characteristic energy spectra (inset) indicated by red dot. Well CB244, 2904.67 m, scanning electron microscope (SEM). (D) Photomicrograph of Qz with hexagonal bipyramidal quartz crystals and Py. Position of characteristic energy spectra (inset) indicated by red dot. Well ZG28, 4122.92 m, SEM. (E) Photomicrograph of Qz and C1 filling the dissolution pores of SD. Well CB244, 2914.37 m, SEM. (F) Energy-dispersive X-ray spectroscopy (EDX) analysis (SEM) of the entire field of part E. (G) Photomicrograph of Qz filling the dissolution pores of SD. Well CB244, 2914.37 m, SEM. (H) EDX analysis of the Qz in part G. Cd1—earliest-formed dolomite cement.

thermal setting (Radke and Mathis, 1980; Al-Aasm et al., 2002; Davies and Smith, 2006). SD commonly fills or lines the walls of fractures (Figs. 4J and 5A), indicating that its genesis was associated with fracturing/faulting caused by tectonic events (Luczaj et al., 2006). The U-Pb age of 161 ± 12 Ma for SD (Fig. 13D) corresponds to the period of intense left-slip thrusting on the Tanlu fault during the early Yanshanian movement (Xiao et al., 2019; Luo et al., 2021). High-angle thrust faults connected to the Precambrian basement developed during the Middle to Late Jurassic (Cheng et al., 2023). These basement-rooted faults are likely the pathways for the migration of hydrothermal fluids (Du et al., 2018). Combined with the burial-thermal history of the Yeli-Liangjiashan Formation, the burial depth of the Yeli-Liangjiashan Formation should have been ∼1100 m during the Middle to Late Jurassic, corresponding to burial temperatures ranging from 55 °C to 65 °C (Fig. 16). The homogenization temperatures of the LVAIs in SD (Fig. 14G) significantly exceed the ambient burial temperature, indicating that the precipitation of SD was closely related to hydrothermal fluids (Machel and Lonnee, 2002). Hydrothermal fluids are often characterized by significantly positive Eu anomalies (Bau, 1991; Bau and Möller, 1993; Frimmel, 2009). SD displays distinctively positive Eu anomalies (Fig. 10D), further illustrating that the genesis of SD was related to hydrothermal fluids. Based on the $\delta^{18}O$ values (Fig. 12) and the homogenization temperatures, employing Land's dolomite-fluid equation (Land, 1983), the calculated $\delta^{18}O_{fluid}$ values for stage I hydrothermal fluids range from −4.48‰ to 1.98‰ relative to Vienna standard mean ocean water (VSMOW), which is lower than hydrothermal fluids of mantle origin (Mattey et al., 1994). The $^{87}Sr/^{86}Sr$ ratios of SD are much higher than those of coeval seawater (Fig. 12B), indicating that the hydrothermal fluids interacted with the silicate clastic rocks and obtained radioactive Sr from the felsic Precambrian basement (Cai et al., 2008; Han et al., 2017; Köster et al., 2017; Lima et al., 2020). The REE patterns of

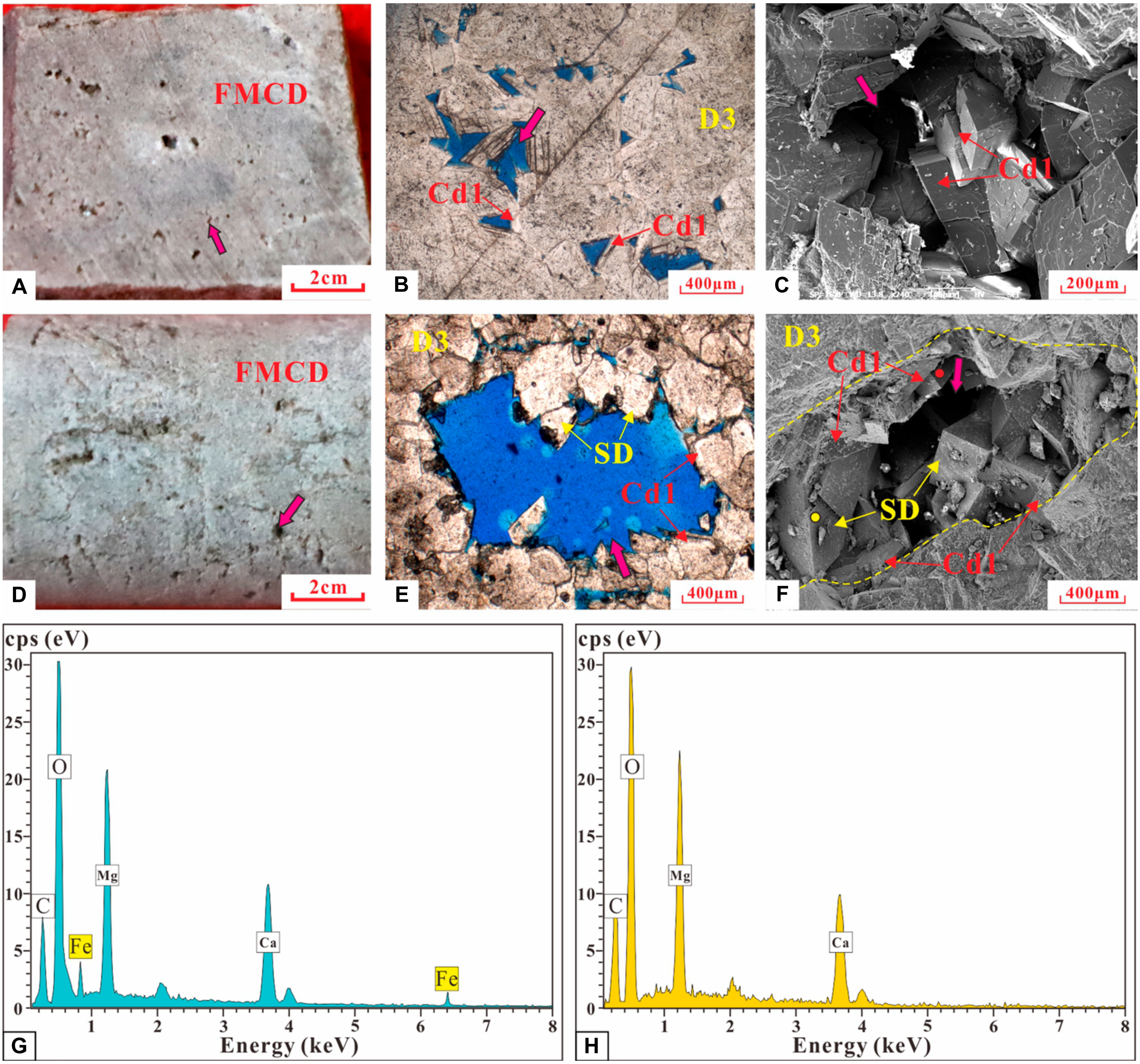

Figure 8. Petrological characteristics of pores and vugs. (A) Core photograph of the pores (pink arrow) in the fine to medium crystalline dolostone (FMCD). Well CB302, 4007.06 m. (B) Photomicrograph of intercrystalline pore (pink arrow). Well CB302, 4007.06 m, plane-polarized light (PPL). (C) Scanning electron microscope (SEM) image of intercrystalline pore (pink arrow). Well CB302, 4007.06 m. (D) Core photograph of the FMCD developing vugs (pink arrow). Well CB244, 2903.77 m. (E) Photomicrograph of the vug (pink arrow), and Cd1 and SD filling around the vug. Well CB244, 2903.77 m, PPL. (F) SEM image of the vug (pink arrow), where yellow dashed line is the boundary of the vug. Cd1 and SD successively filled the vug. Well CB244, 2903.77 m. (G) Energy-dispersive X-ray spectroscopy (EDX) analysis of the SD in part F, yellow point. (H) EDX analysis of the Cd1 in part F, red point. Cd1—earliest-formed dolomite cement; D3—matrix of fine to medium crystalline dolostone; SD—saddle dolomite.

SD show significant LREE depletion and heavy REE (HREE) enrichment (Fig. 11B), which are consistent with the REE patterns of saddle dolomite precipitated from nonmagmatic hydrothermal fluids (Zhang et al., 2014; Stacey et al., 2021a) and distinctly different from general LREE-enriched and HREE-depleted saddle dolomites formed in magmatic hydrothermal fluids (Haas et al., 1995; Cai et al., 2008; Kareem et al., 2021). Consequently, the stage I hydrothermal fluids that precipitated SD were derived from the Precambrian basement.

Both SD and Cd2 exhibit dull-red luminescence (Figs. 4H and 4 K) closest to the fracture walls (Figs. 4I, 4J, and 6D). SD developed in the

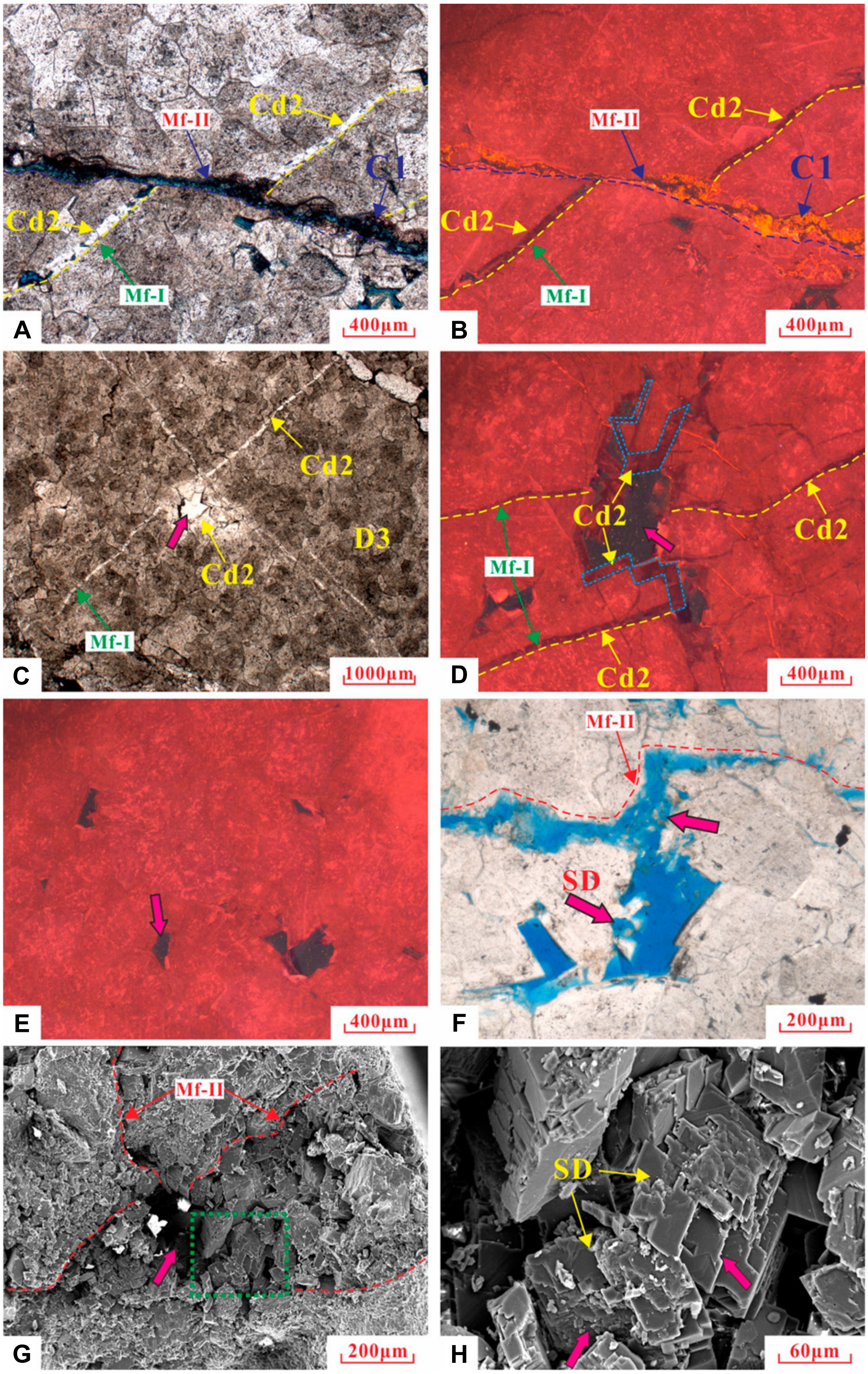

Figure 9. (A) First-stage microfractures (Mf-I) filled with Cd2 (dolomite cement adjacent to Cd1) and cut by second-stage microfractures (Mf-II) filled with first type of calcite (C1). Well CB302, 4003.26 m, plane-polarized light (PPL). (B) Cathodoluminescence (CL) photomicrograph of image in part A. Well CB302, 4003.26 m. (C) Mf-I filled with Cd2 crosscutting the intercrystalline pores (pink arrow) where Cd2 developed. Well CB302, 4005.45 m, PPL. (D) Mf-I filled with Cd2 crosscutting the intercrystalline pores (pink arrow) where Cd2 developed. Blue dashed lines are the profile of Cd2. Well CB302, 4003.26 m, CL. (E) Photomicrograph showing Cd2 did not develop in the intercrystalline pores (pink arrow) that are not connected by Mf-I. Well CB302, 4006.76 m, CL. (F) Mf-II displaying uneven edge with dissolution (pink arrow). Well CB244, 2903.77 m, PPL. (G) Scanning electron microscope (SEM) image of Mf-II and pore (pink arrow), with Mf-II connected with the pore. Well CB244, 2906.47 m, SEM. (H) Magnification of the green dashed box in part G, where saddle dolomite (SD) filling the pore displays dissolution characteristics (pink arrow). SEM.

dolomite reservoirs adjacent to the major faults, whereas Cd2 dominantly developed away from the major faults (Fig. 17), indicating a gradual change in the characteristics of the same stage of hydrothermal fluids as they infiltrated the strata (Koeshidayatullah et al., 2020b; Stacey et al., 2021a). Most of the geochemical characteristics of Cd2 highly coincide with SD, including the $\delta^{13}C$ values, $^{87}Sr/^{86}Sr$ ratios (Fig. 12), La/Ho ratios, ΣLREE/ΣMREE ratios, and Fe and Mn contents (Figs. 10A, 10C, and 10D). These results further demonstrate that Cd2 formed during the same stage as the hydrothermal fluids that precipitated SD. However, Cd2 shows minor positive Eu anomaly characteristics (Fig. 10D) and relatively lower homogenization temperatures of the LVAIs in Cd2 than those in SD (Fig. 14G), indicating that Cd2 formed in relatively low-temperature hydrothermal fluids (Bau et al., 2010; Frei et al., 2017). Temperature significantly affects the growth behavior of crystals, resulting in larger crystal sizes at higher temperatures (Rollett et al., 1989; Holm et al., 1998; Wei and Li, 2011). Therefore, particularly in the fractures, the crystal size of Cd2 (Fig. 6E) is significantly narrower than that of SD (Figs. 4J and 5A), suggesting that the difference in size is due to the change in temperature of the hydrothermal fluids. The constant cooling of hydrothermal fluids as they migrated into the formation led to differences in the homogenization temperatures of the LVAIs in SD and Cd2 as well as differences in $\delta^{18}O$ values due to temperature variations (Milliman, 1974; Veizer and Prokoph, 2015). Furthermore, the $MgCO_3$ content of Cd2 (42.32–44.56 wt%) is lower than that of SD (44.55–45.11 wt%). Therefore, combined with the homogenization temperatures of the LVAIs in Cd2 and SD, as the hydrothermal fluid migrated along the fractures toward the interior of the formation, it gradually transformed from a Mg-rich hot hydrothermal fluid to a Mg-depleted cooler-temperature hydrothermal fluid (Figs. 18B–18D; Wendte et al., 2009; Kaczmarek and Thornton, 2017; Koeshidayatullah et al., 2020b; Li et al., 2022). Additionally,

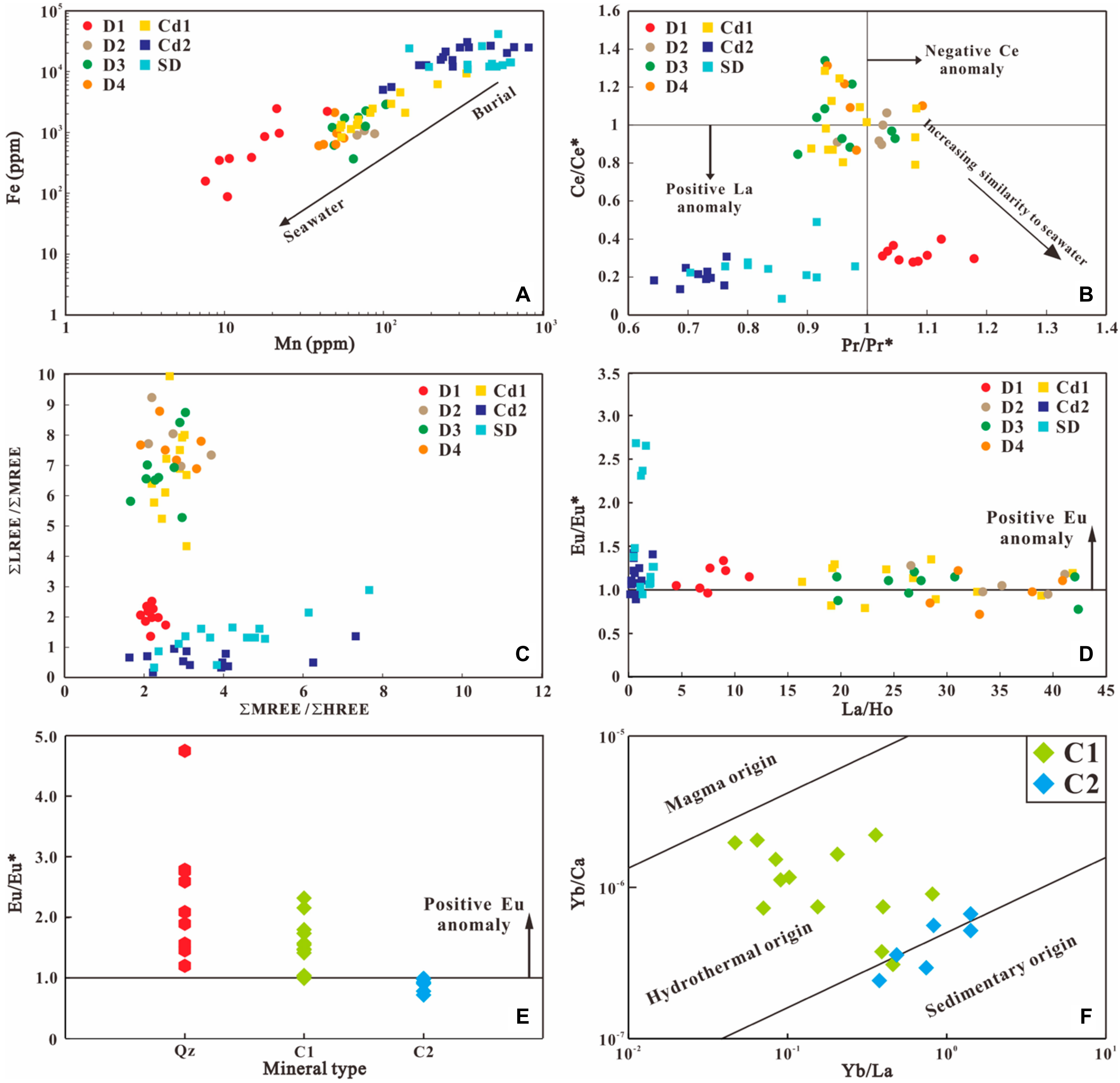

Figure 10. (A) Mn versus Fe concentrations. (B) δCe versus δPr (Bau and Dulski, 1996; Webb and Kamber, 2000; Stacey et al., 2021a). (C) ΣMREE/ΣHREE ratios versus ΣLREE/ΣMREE ratios (L/M/HREE—light/middle/heavy rare earth elements). (D) La/Ho ratios versus δEu. (E) δEu of Qz, C1, and C2. (F) Yb/La ratios versus Yb/Ca ratios of C1 and C2 using the method of Möller et al. (1980). D1—relict grains of the dolorudstones; D2, D3, and D4—matrices of fine crystalline dolostone (FCD), fine to medium crystalline dolostone (FMCD), and medium to coarse crystalline dolostone (MCCD), respectively; Cd1, Cd2—earliest-formed dolomite cement and dolomite cement adjacent to Cd1, respectively; C1, C2—first and second type of calcite; respectively; SD—saddle dolomite.

Cd2 exhibits relatively lower ΣREE compared to SD (Table A1), suggesting that continuous dilution of REE concentrations due to hydrothermal fluid was gradually affected by mixing with the original formation water and interaction with the carbonate wall rocks (Hu et al., 2010; Wang et al., 2014).

In particular, to prevent misleading readers when dividing the stages of the hydrothermal fluids, it is worth noting that these two phases of dolomite (Cd2, SD) were identified separately in the petrographic and geochemical descriptions, but this does not mean that they were derived from different stages of the hydrothermal fluids. The petrographic and

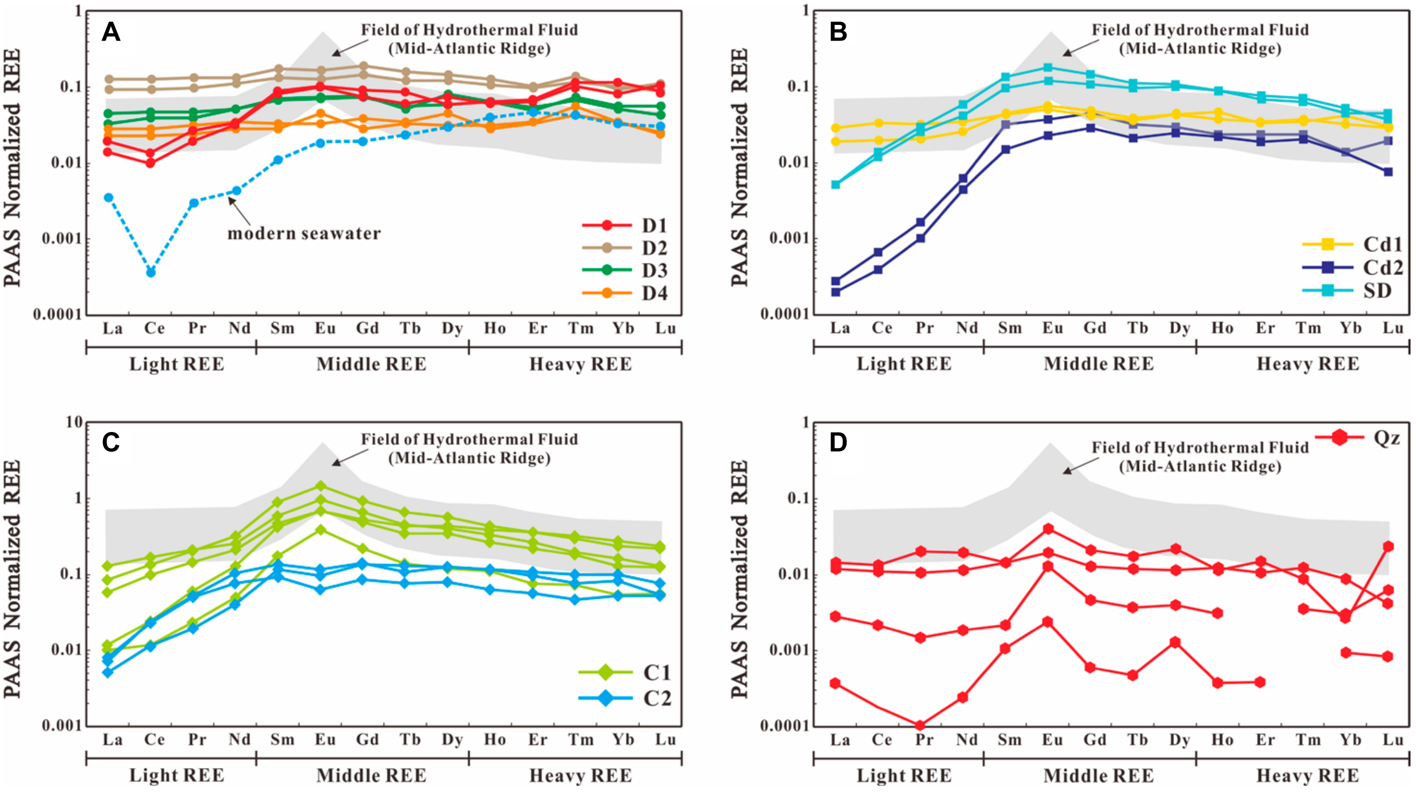

Figure 11. (A) Rare earth element (REE) patterns of D1, D2, D3, and D4. (B) REE patterns of Cd1, Cd2, and SD. (C) REE patterns of C1 and C2. (D) REE patterns of quartz (Qz). REE pattern of modern seawater normalized to post-Archean Australian shale (PAAS) was adopted from Webb and Kamber (2000); hydrothermal fluid profile was adopted from Douville et al. (2002). See Figure 10 caption for mineral abbreviations.

geochemical comparisons of Cd2 and SD precipitated from stage I hydrothermal fluids reflect the constantly varying characteristics of the hydrothermal fluids as they infiltrated the strata. Additionally, the U content of Cd2 is extremely low, resulting in the unavailability of an accurate U-Pb age. However, the above discussion suggests that the U-Pb age of SD is an approximate representation of the U-Pb age of Cd2.

5.1.2. Stage II Hydrothermal Fluids

The positive Eu anomalies (Fig. 10E) of C1 and Qz and the high homogenization temperatures (Figs. 14B and 14C) of the LVAIs in C1 and Qz suggest that C1 and Qz precipitated

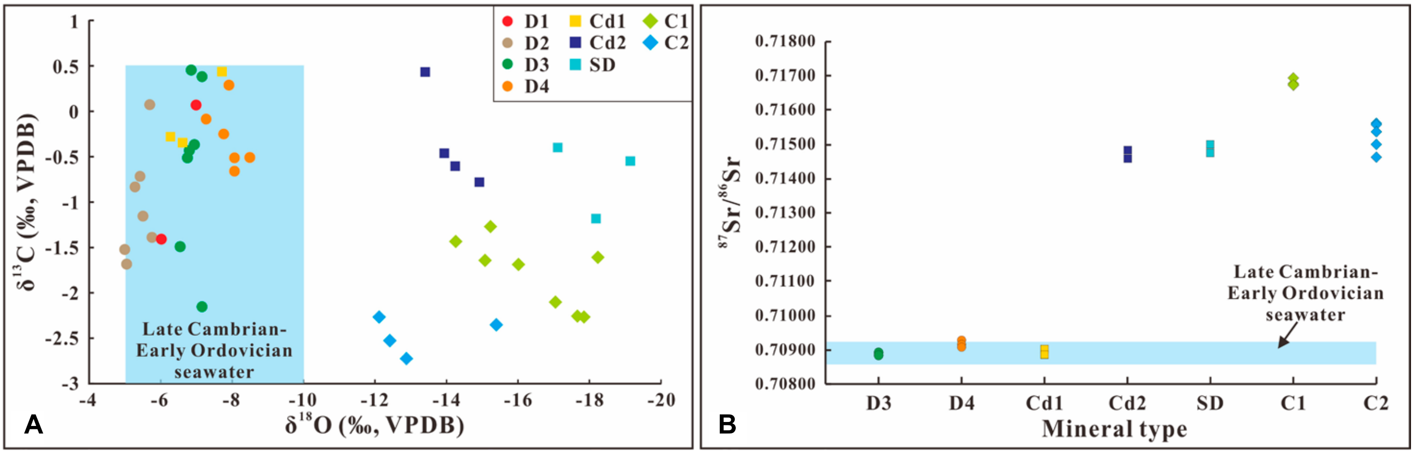

Figure 12. (A) Carbon and oxygen isotopic compositions and ranges of carbonate minerals. The isotopic range of carbonate precipitated from the late Cambrian–Early Ordovician coeval seawater is marked with a blue bar (data from Veizer et al., 1999). (B) $^{87}Sr/^{86}Sr$ ratios of carbonate minerals. Blue area represents the $^{87}Sr/^{86}Sr$ ratios of the carbonate precipitated from the late Cambrian–Early Ordovician coeval seawater, ranging from 0.7086 to 0.7092 (Burke et al., 1982; Veizer et al., 1999). See Figure 10 caption for mineral abbreviations. VPDB—Vienna Peedee belemnite.

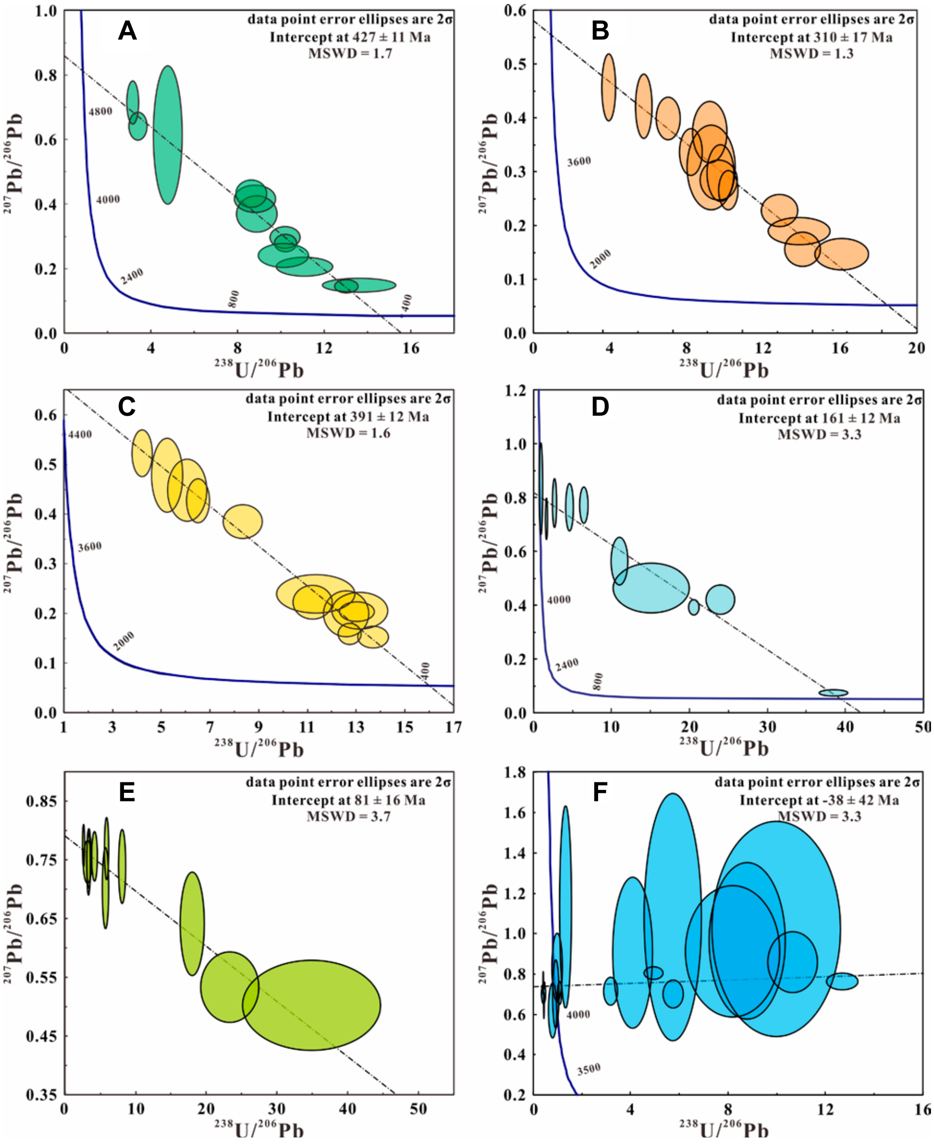

Figure 13. Tera-Wasserburg concordia diagrams showing $^{238}U/^{206}Pb$ versus $^{207}Pb/^{206}Pb$ for (A) D3, (B) D4, (C) Cd1, (D) SD, (E) C1, and (F) C2 in the Lower Ordovician Yeli-Liangjiashan Formation. See Figure 10 caption for mineral abbreviations. MSWD—mean square of weighted deviates.

from hydrothermal fluids (Dong et al., 2013). C1 plots within the hydrothermal origin in the Yb/La versus Yb/Ca plot (Fig. 10F; Möller et al., 1980). Furthermore, both C1 and Qz exhibit REE patterns similar to those of the hydrothermal fluid of the Mid-Atlantic Ridge (Fig. 11C), indicating that these hydrothermal fluids probably had a magmatic source (Douville et al., 2002; Jiu et al., 2022). Based on the calcite-fluid fractionation equation of Friedman and O'Neil (1977) and the $\delta^{18}O$ values and the homogenization temperatures of the LVAIs in C1, the estimated $\delta^{18}O_{fluid}$ values of the hydrothermal fluids forming C1 vary from −2.48‰ to 5.6‰ VSMOW, which is close to the hydrothermal fluids of mantle origin (Mattey et al., 1994). The U-Pb age of 81 ± 16 Ma for C1 (Fig. 13E) corresponds to the Late Cretaceous. During this period, preexisting NW-striking thrust faults such as the Chengbei fault were dominantly reactivated, and extensional inversion occurred (Wang et al., 2022a). Meanwhile, because of the left-lateral strike-slip motion on the Tanlu fault, NE-striking slip faults formed, such as the Chengbei 30 fault (Liu et al., 2019; Cheng et al., 2023). Intense structural strike-slip activity triggered the upwelling of the mantle floor and intense volcanic eruptions (Xiao et al., 2019). The close occurrence of C1 with Qz (Figs. 7E and 7F) indicates that silica was enriched in the hydrothermal fluids that precipitated C1. The vapor phase of the LVAIs in both C1 and Qz is characterized by significant hydrogen sulfide (H_2S) gas peaks (Figs. 15B, 15D, and 15E). The $\delta^{13}C$ values of C1 range from −2.27‰ to −1.27‰ VPDB (Fig. 12A), which are close to mantle-derived calcite (Nelson et al., 1988; Wang et al., 2022b) but higher than calcites genetically closely associated with thermochemical sulfate reduction (TSR; Cai et al., 2013; Hao et al., 2015). The hydrothermal fluids also precipitated associated hydrothermal minerals, such as barite and pyrite (Figs. 7B–7D), and evidence of the dissolution of the anhydrite related to the TSR is not present in the study (Jiang et al., 2018), indicating that the hydrothermal fluids from the mantle carried a large amount of sulfur components (Zhou et al., 2018). Therefore, stage II hydrothermal fluids were derived from the mantle, and the hydrothermal fluids carried H_2S mainly from the reduction of degassed SO_2 from the deep magma (Chen et al., 2015). Moreover, the $^{87}Sr/^{86}Sr$ ratios of C1 (Fig. 12B) are extremely high. The Cambrian Maozhuang and Xuzhuang Formations deposited thick shale (Zhang et al., 2022). When hydrothermal fluids migrated through the felsic Precambrian basement or Cambrian thick shale containing argillaceous or feldspathic components, quantities of radioactive Sr isotopes were obtained (Qing and Mountjoy, 1994; Köster et al., 2017; Bai et al., 2018; Guo et al., 2021). Additionally, Qz barely developed in the dolomite reservoirs away from the major faults (Fig. 17) and gradually decreases with increasing distance from the major faults (Figs. 18F and 18H), suggesting that the migration of hydrothermal fluids into the formation was accompanied by a gradual depletion of SiO_2.

Although SD/Cd2 and C1/Qz have a hydrothermal origin, they were derived from different stages of the hydrothermal fluids and have distinctive characteristics. C1 has a significantly higher $^{87}Sr/^{86}Sr$ than SD and Cd2, while showing a significant negative characteristic in $\delta^{13}C$ compared to SD and Cd2. If C1 and SD/Cd2 formed from the same period of hydrothermal fluids, then $\delta^{13}C$ fractionation would be difficult because of temperature and pressure variations (Machel, 2004; Huang et al., 2021), and there should not be such a large difference in $^{87}Sr/^{86}Sr$ ratios between them. For petrographic evidence: (1) SD and Cd2 are closer to the edges of the pores and fractures compared to C1 (Figs. 4G–4I, 6D–6F, and 8F), (2) both C1 and Qz were observed filling the dissolution pores of the SD in the fractures (Figs. 5A, 7E, and 7F), and (3) Mf-I filled with C1 crosscut Mf-II filled with Cd2 (Figs. 9A and 9B). These results demon-

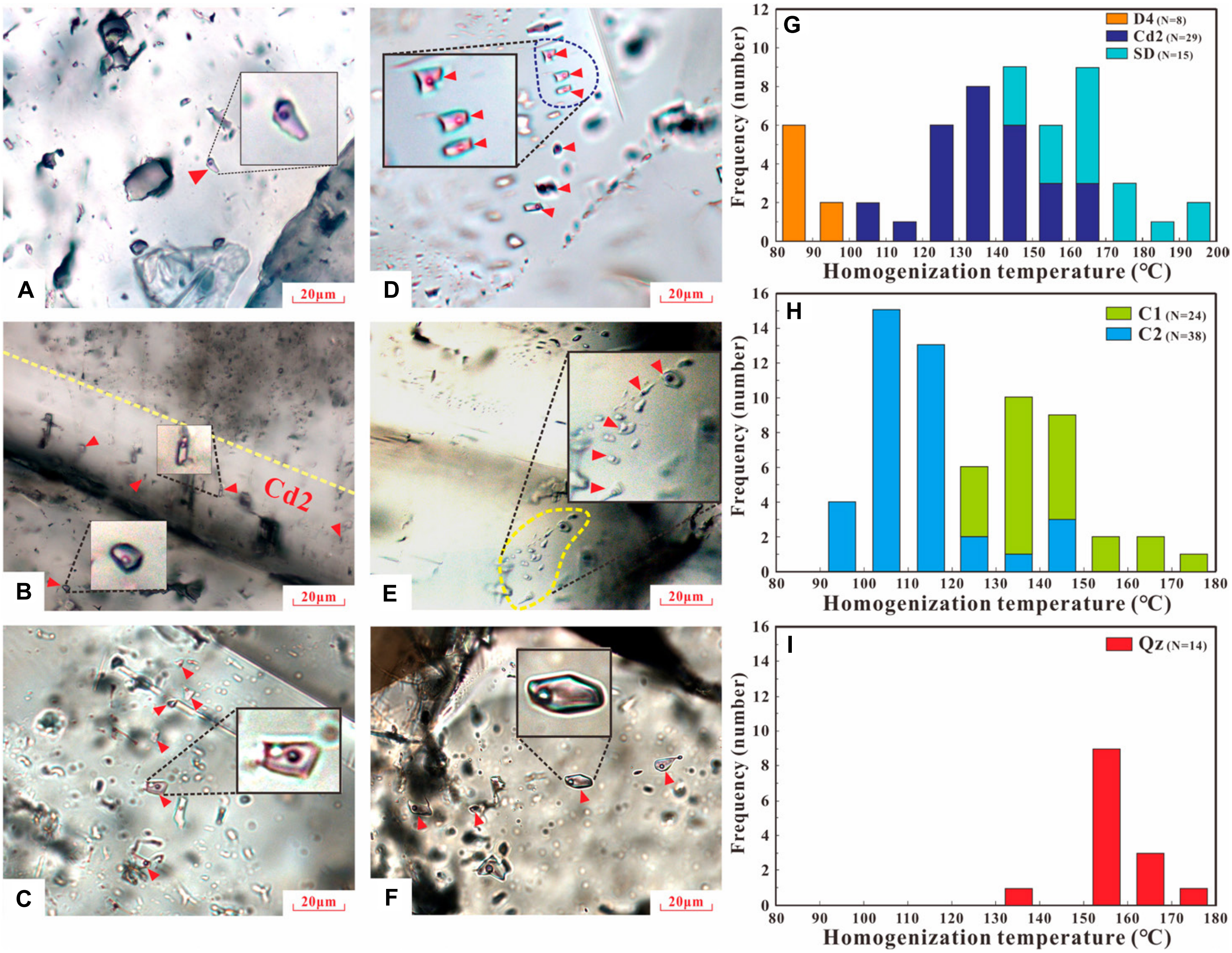

Figure 14. Petrographic photomicrographs (A–F) and homogenization temperatures (G–I) of fluid inclusions. (A) D4, (B) Cd2, (C) SD, (D) C1, (E) C2, and (F) quartz (Qz). Red arrows—liquid-vapor two-phase aqueous inclusions (LVAIs) in the different host rocks. (G) Homogenization temperatures of the LVAIs in D4, Cd2, and SD. (H) Homogenization temperatures of the LVAIs in C1 and C2. (I) Homogenization temperatures of the LVAIs in Qz. See Figure 10 caption for mineral abbreviations.

strate that the hydrothermal fluids that precipitated C1 and Qz occurred later than those that precipitated SD and Cd2 (Fig. 16).

The $\delta^{18}O$ values (Fig. 12A) and $^{87}Sr/^{86}Sr$ ratios (Fig. 12B) of C2 are lower than those of C1, indicating that C2 and C1 originated from different sources (Huang et al., 2021). The data from the radioactive U/Pb isotope ratios did not provide a reliable U-Pb age for C2 (Fig. 13F), which probably resulted from an open- or mixed-fluid system (Rasbury and Cole, 2009; Roberts et al., 2020). However, according to the distribution between C1 and C2 in the fractures, C1 is closer to the edges of the fractures than C2 (Figs. 6A–6C), so it is inferred that C2 definitely formed after C1. Therefore, the U-Pb age of C1 was utilized to constrain the age of C2, which suggests that C2 formed later than the Late Cretaceous (Fig. 16). During this period, under the right-lateral strike-slip stress of the Tanlu fault, the preexisting NE and NW strike-slip faults were reextended and activated (Xiao et al., 2019; Liu et al., 2022). Deep fluids followed an upward influx. However, the homogenization temperatures of the LVAIs in C2 (Fig. 14H) are much lower than the maximum burial temperature during the Late Cretaceous to the Neogene (~150 °C). C2 displays negative Eu anomalies (Fig. 10E) and mostly occurs in the range of sedimentary origin in the Yb/La-Yb/Ca cross-plot (Fig. 10F; Möller et al., 1980). Therefore, the genesis of C2 was not closely associated with hydrothermal fluids. Furthermore, the content of C2 is low, and C2 is only distributed in the fractures (Fig. 6A); therefore, there is no further discussion of C2 here.

5.2. Temporal Relationships among Dolomitization, Pore Formation, and Hydrothermal Fluid Activities

5.2.1. Dolomitization Prior to Hydrothermal Fluid Activities

Constraining the temporal relationship between early dolomitization and hydrothermal fluid activities requires an interpretation of whether the genesis of early dolomitization was

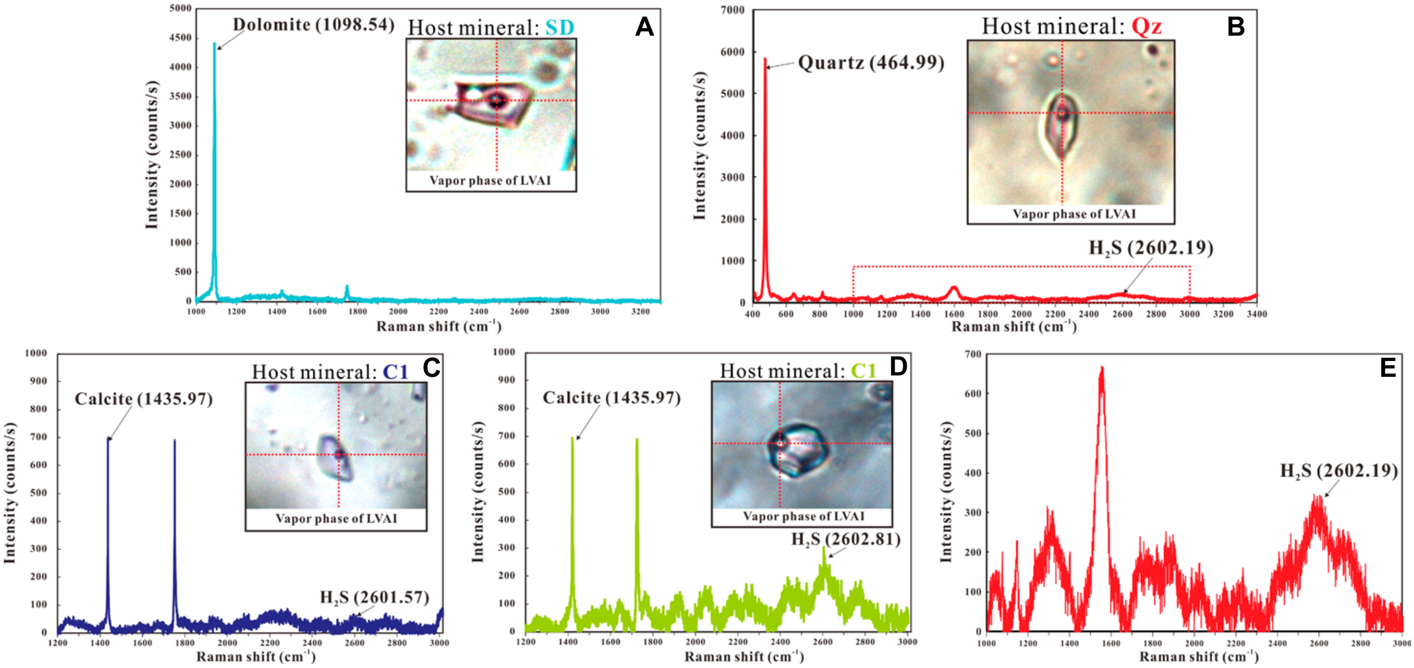

Figure 15. Raman analysis spectrum of the liquid-vapor two-phase aqueous inclusions (LVAIs) in: (A) saddle dolomite (SD), well CB244, 2914.37 m; (B) quartz (Qz), well CB244, 2914.37 m; (C) first type of calcite (C1) (away from the major fault), well CB302, 4002.36 m; (D) C1 (adjacent to the major fault), illustrating typical H_2S peak, well CB244, 2914.37 m; and (E) magnification of the red dashed box in part B, illustrating typical H_2S peak. Intersection of red dashed lines represents the focal position of the incident laser.

associated with hydrothermal fluids and application of in situ U-Pb dating.

D1 is typically characterized by REE patterns similar to those of modern seawater, including prominent negative Ce anomalies (Fig. 11A; Webb and Kamber, 2000), and it lies within the seawater quadrant in the Ce/Ce* versus Pr/Pr* plot (Fig. 10B), indicating that D1 formed in a normal seawater environment (Bolhar and Van Kranendonk, 2007; Zhao et al., 2009; Stacey et al., 2021b). Fe and Mn concentrations are typically very low in seawater (Warren, 2000). D1, D2, D3, and D4 showed much lower concentrations of Fe and Mn than Cd2 and SD (Fig. 10A), suggesting that they formed near the surface of seawater or at a shallow depth. The $\delta^{18}O$ and $\delta^{13}C$ values of D2, D3, and D4 are within the respective ranges of the late Cambrian–Early Ordovician coeval seawater (Fig. 12A; Veizer et al., 1999), and the $^{87}Sr/^{86}Sr$ ratios of D3 and D4 overlap with the estimated $^{87}Sr/^{86}Sr$ ratio range for the late Cambrian–Early Ordovician coeval seawater (Fig. 12B; Burke et al., 1982; Veizer et al., 1999), indicating that dolomitization fluids forming D2, D3, and D4 were all associated with coeval seawater. Therefore, the genesis of D1, D2, D3, and D4 was associated with coeval seawater, further illustrating that early dolomitization is irrelevant to the two stages of hydrothermal fluids.

D1 and D2 are characterized by finely subhedral to euhedral crystals (Figs. 3C and 3E), suggesting that they formed at relatively low temperatures, lower than the critical roughening temperature (50–60 °C; Gregg and Sibley, 1984; Sibley and Gregg, 1987; Warren, 2000). Therefore, D1 and D2 formed near the surface and at depths less than 500 m. Combined with the burial-thermal history, their formation occurred during the Ordovician Period (Fig. 16). The U-Pb ages of D3 and D4 are 427 ± 11 Ma and 310 ± 17 Ma (Figs. 13A and 13B), respectively, corresponding to the period from the Late Ordovician to the late Carboniferous. However, the U-Pb ages of SD and C1 are 161 ± 12 Ma and 81 ± 16 Ma, respectively, corresponding to two stages of hydrothermal activity from the Middle Jurassic to the Late Cretaceous (Fig. 16). Consequently, the two-stage hydrothermal activities occurred later than the early dolomitization.

5.2.2. Formation of Pores Prior to Hydrothermal Fluid Activity

Determining the genesis and sequential formation of multiphase authigenic minerals around pores is important for constraining the temporal relationship between pore formation and hydrothermal fluid activities.

Cd1 is the first phase of authigenic minerals closest to the edges of the pores/vugs (Figs. 4A–4G, 6F, 8B, 8F, and 17). Compared to D2, D3, and D4, Cd1 is characterized by similar concentrations of Fe and Mn (Fig. 10A) and similar REE patterns (Figs. 11A and 11B). Furthermore, the $\delta^{18}O$ values, $\delta^{13}C$ values, and $^{87}Sr/^{86}Sr$ ratios of Cd1 highly overlap with those of coeval seawater (Fig. 12). These results demonstrate that the genesis of Cd1 was associated with coeval seawater rather than hydrothermal fluids. In particular, the edges of Cd1 near the pores exhibit euhedral characteristics (Figs. 4A–4D). A convincing explanation for this petrographic phenomenon is that pores/vugs were present before the precipitation of Cd1; without the presence of these pores, there would have been no space for Cd1 to grow such euhedral crystals. The U-Pb age of Cd1 is 391 ± 12 Ma (Fig. 13C), so the pores formed earlier than 391 ± 12 Ma. Moreover, the U-Pb ages of SD and C1 are distinctly later than that of Cd1, indicating that the pores formed much earlier than the two stages of hydrothermal fluid activities. This further demonstrates that the genesis of pores was not correlated with the two stages of hydrothermal fluids. The U-Pb age of Cd1 is close to that of D3; in other words, the U-Pb age of Cd1 is close to the time of early dolomitization, suggesting that the pores were probably inherited from precursor limestones or the earliest D1 stage of dolomitization (Weyl, 1960; Saller et al., 2014).

An explanation is needed as to why the U-Pb age of Cd1 is earlier than that of D4. Compared

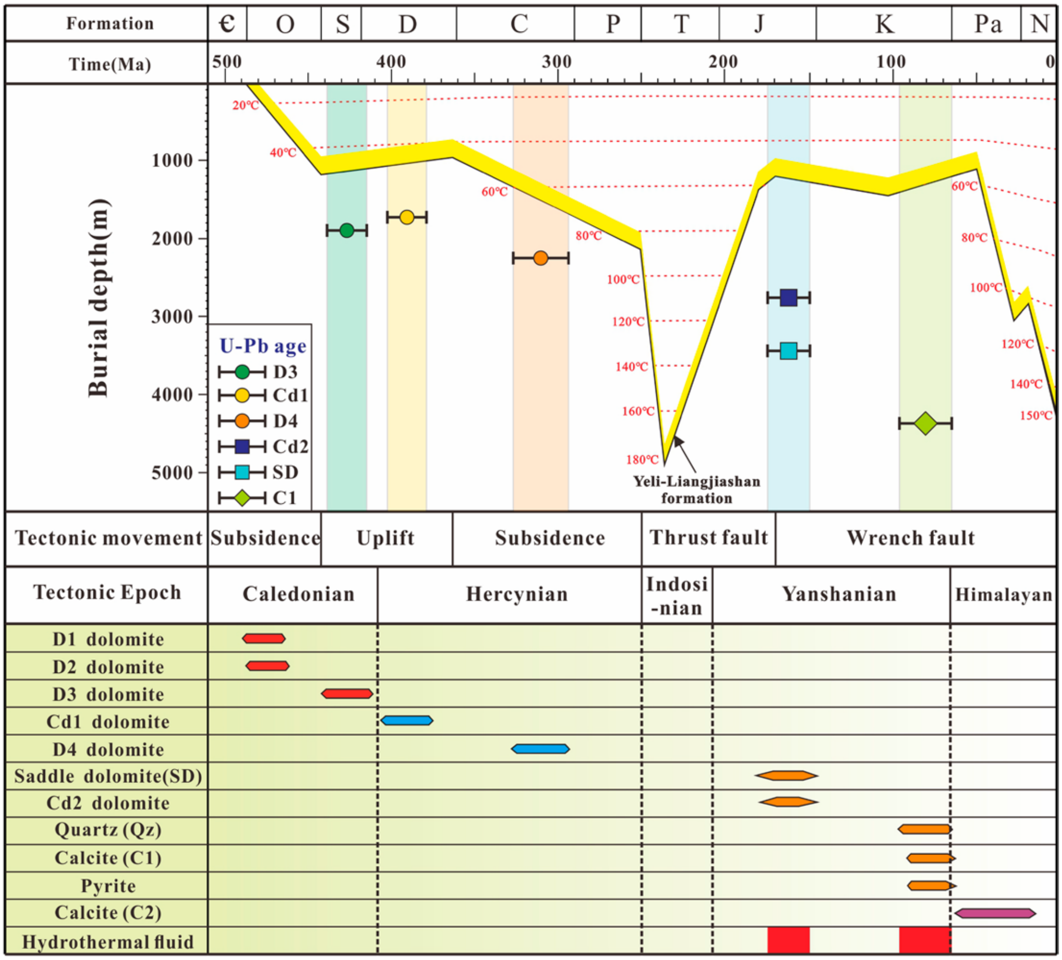

Figure 16. Burial history curves of the Lower Ordovician Yeli-Liangjiashan Formation, major diagenetic events, and hydrothermal fluid activity. See Figure 10 caption for mineral abbreviations. Time period abbreviations: Є—Cambrian; O—Ordovician; S—Silurian; D—Devonian; C—Carboniferous; P—Permian; T—Triassic; J—Jurassic; K—Cretaceous; Pa—Paleogene; N—Neogene.

to D3, there is almost no development of Cd1 in D4. The dolomite crystals of D4 tend to be coarser and display a more curved crystal plane (Fig. 3F), indicating a more rapid growth at temperatures above the roughening temperature (Gregg and Sibley, 1984). The $\delta^{18}O$ values of D4 (Fig. 12A) are more negative than those of D3, reflecting a greater degree of recrystallization with increasing burial temperature (Qing et al., 2023). Therefore, with increasing burial depth, D4 probably formed because D3 underwent significant recrystallization (Huang et al., 2021). In a recent study, Gasparrini et al. (2023) revealed the recrystallization of dolomite by U-Pb dating. It is suggested that U-Pb ages can be used to represent the time when recrystallization occurred. The homogenization temperatures of the LVAIs in D4 range from 85.2 °C to 95.2 °C (Fig. 14G). Combined with the burial history (Fig. 16), this suggests a formation time of D4 from 260 Ma to 250 Ma. This time is later than the U-Pb age of D4 (310 ± 17 Ma). This suggests that the U-Pb isotopic system of D4 is a composite of early dolomitization and late recrystallization. In addition, the diagenesis during the recrystallization process probably excludes radiogenic Pb from the crystal lattices, resulting in a younger measured U-Pb age (Rasbury and Cole, 2009; Qiao et al., 2020). Therefore, the U-Pb age of D4 is closer to the time at which recrystallization occurred.

5.3. Influence of Hydrothermal Fluids on Dolomite Reservoirs

The influence of hydrothermal fluids with different properties (temperature, pH, ion concentration, and gas composition) on dolomite reservoirs is distinctive. In addition, the properties of the hydrothermal fluids change constantly as they migrate up the faults and into the formation (Koeshidayatullah et al., 2020b; Chen et al., 2022), resulting in differences in the modification of the dolomite reservoirs adjacent to or away from the faults during the same stage of hydrothermal fluid activity (Fig. 17).

5.3.1. Influence of Stage I Hydrothermal Fluids

It has been proven that the pores/vugs in these dolomites were probably inherited from precursor limestones or the earliest D1 stage of dolomitization; therefore, the influence of the two stages of hydrothermal fluids on the dolomite reservoirs can be further discussed. Stage I hydrothermal fluids were derived from the Precambrian basement, which mainly precipitated SD and Cd2. In the pores/vugs, SD and Cd2 grew around Cd1, and Cd1 was found to have a euhedral crystal morphology using SEM (Figs. 4A–4D, 8C, and 8F), demonstrating that it was not influenced by hydrothermal dissolution. This further suggests that hydrothermal dissolution was not associated with the stage I hydrothermal fluids. In addition, based on the intensity of H_2S contained in the vapor-phase components of the LVAIs in SD (Fig. 15A), the hydrothermal fluids precipitating SD contained a relatively low amount of corrosive gas (H_2S), which further proves that stage I hydrothermal fluids had a very weak ability to cause dissolution. SD and Cd2, especially SD, occupied a large volume of the fractures (Figs. 4J and 6D). Furthermore, Cd2 significantly occupied the pore space as a ring band growing around Cd1 (Figs. 4E–4G and 17D), which is destructive to the dolomite reser-

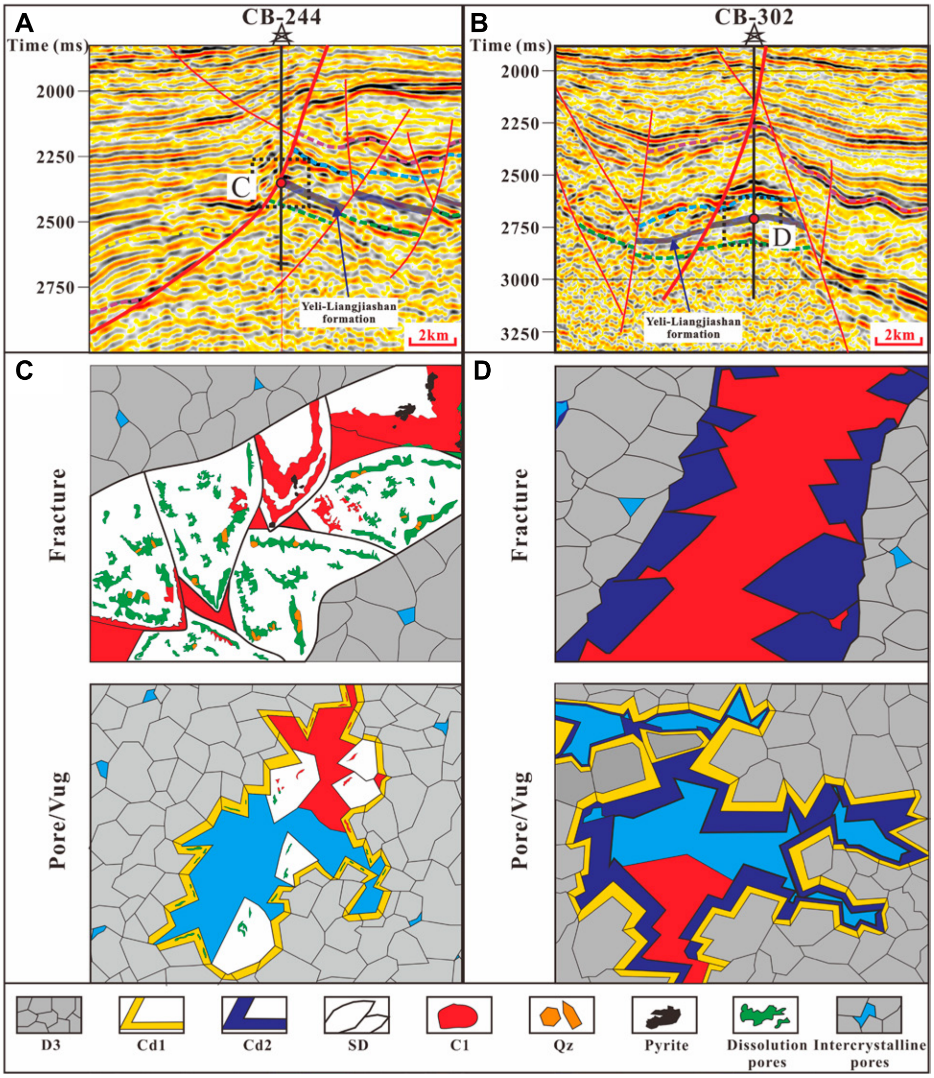

Figure 17. Response of differential multistage hydrothermal fluids in the fractures and pores in near-fault (well CB244) and distal-fault (well CB302) dolomite reservoirs. (A) Seismic profile across well CB244. (B) Seismic profile across well CB302. (C) Types and characteristics of authigenic minerals developing in fractures and pores adjacent to the major faults. (D) Types and characteristics of authigenic minerals developing in fractures and pores away from the major faults. Qz—quartz; see Figure 10 caption for other mineral abbreviations.

voirs. Therefore, the dominant influence of stage I hydrothermal fluids on the dolomite reservoirs was precipitation.

5.3.2. Influence of Stage II Hydrothermal Fluids

Stage II hydrothermal fluids originated from the mantle, and the main products were C1 and Qz, accompanied by pyrite and barite (Figs. 7B–7D). The most abundant stage II hydrothermal mineral is C1, which filled both fractures and pores. Based on the intensity of H_2S contained in the vapor-phase components of the LVAIs in C1 (Fig. 15D), the stage II hydrothermal fluids in the dolomite reservoirs adjacent to major faults contained a relatively notable amount of corrosive gas (H_2S; Fig. 18G) that may have caused dolomite to dissolve (Davies and Smith, 2006). The reactions were described by Jiang et al. (2018) as follows:

$$Fe^{2+} + 2H_2S \rightarrow FeS_2 + 4H^+; \qquad (1)$$

$$CaMg\left(CO_3\right)_2 + 4H^+ \rightarrow Ca^{2+} + Mg^{2+} + H_2O + CO_2. \qquad (2)$$

Equation 1 and Equation 2 represent the generation of H^+ with pyrite precipitation, which results in dolomite dissolution. Combined with the petrographic observations, C1 and Qz filled the dissolution pores of the SD in the fractures and were accompanied by significant amounts of pyrite (Figs. 5A, 7B, 7D, and 17C), indicating that H_2S-related dissolution occurred (Cai et al., 2001; Jiu et al., 2022) and that the dissolution was significant in the fractures. Dissolution is still observed in the pores/vugs and present in SD and Cd1 (Figs. 6E and 9H). However, compared to the dissolution within the fractures (Fig. 5A), the dissolution in the pores/vugs is much weaker and hardly extends into the matrix. There are still significant dissolved residues of Cd1 and SD (Fig. 6E), indicating that the secondary pores generated by H_2S-related dissolution are very few and much fewer than the pores prior to the precipitation of Cd1. Consequently, after the dissolution by stage II hydrothermal fluids, the pore space did not recover to the original pore space prior to the precipitation of Cd1.

Dissolution is not visible in the dolomite reservoirs away from major faults. As previously mentioned, stage I hydrothermal fluids in the dolomite reservoirs away from the major faults mainly precipitated Cd2 (Fig. 17D). Cd2 was barely dissolved by the stage II hydrothermal fluid and exhibits intact crystal planes in the pores and fractures (Figs. 4F, 6D, and 6F). The stage II hydrothermal fluids away from the major faults contained a relatively lower amount of corrosive gas (H_2S) than the stage II hydrothermal fluids adjacent to major faults (Figs. 15C, 15D, and 18G). Therefore, it is speculated that as stage II hydrothermal fluids migrated along the fractures into the strata, the corrosive gas (H_2S) was gradually consumed, and the dissolution ability of the hydrothermal fluids decreased gradually (Fig. 18G). The trend of constant depletion of H_2S is similar to that of the gradual decrease in the amount of Qz with increasing distance from the major faults (Fig. 18H). Based on the trend in the intensity of H_2S, it should be noted that the dissolution capacity of hydrothermal fluids was probably depleted within a distance of 800 m from the major faults (Fig. 18H). Therefore, the influence of dissolution can be considered to be minimal for extensively developed dolomite reservoirs. This localized dissolution mainly dissolved the minerals precipitated by the hydrothermal fluids in the previous stage in the pores/fractures (Figs. 5A, 9F, and 9H) and did not constructively alter the dolomite matrix and generate new pore spaces, indicating that the contribution of such dissolution was limited. Moreover, C1 significantly occupied most of the pores/fractures in the dolomite reservoirs, whether adjacent to or away from the major faults (Figs. 6D–6F, 17C, and 17D). In summary, stage II hydrothermal fluid caused significant H_2S-related dissolution in the dolo-

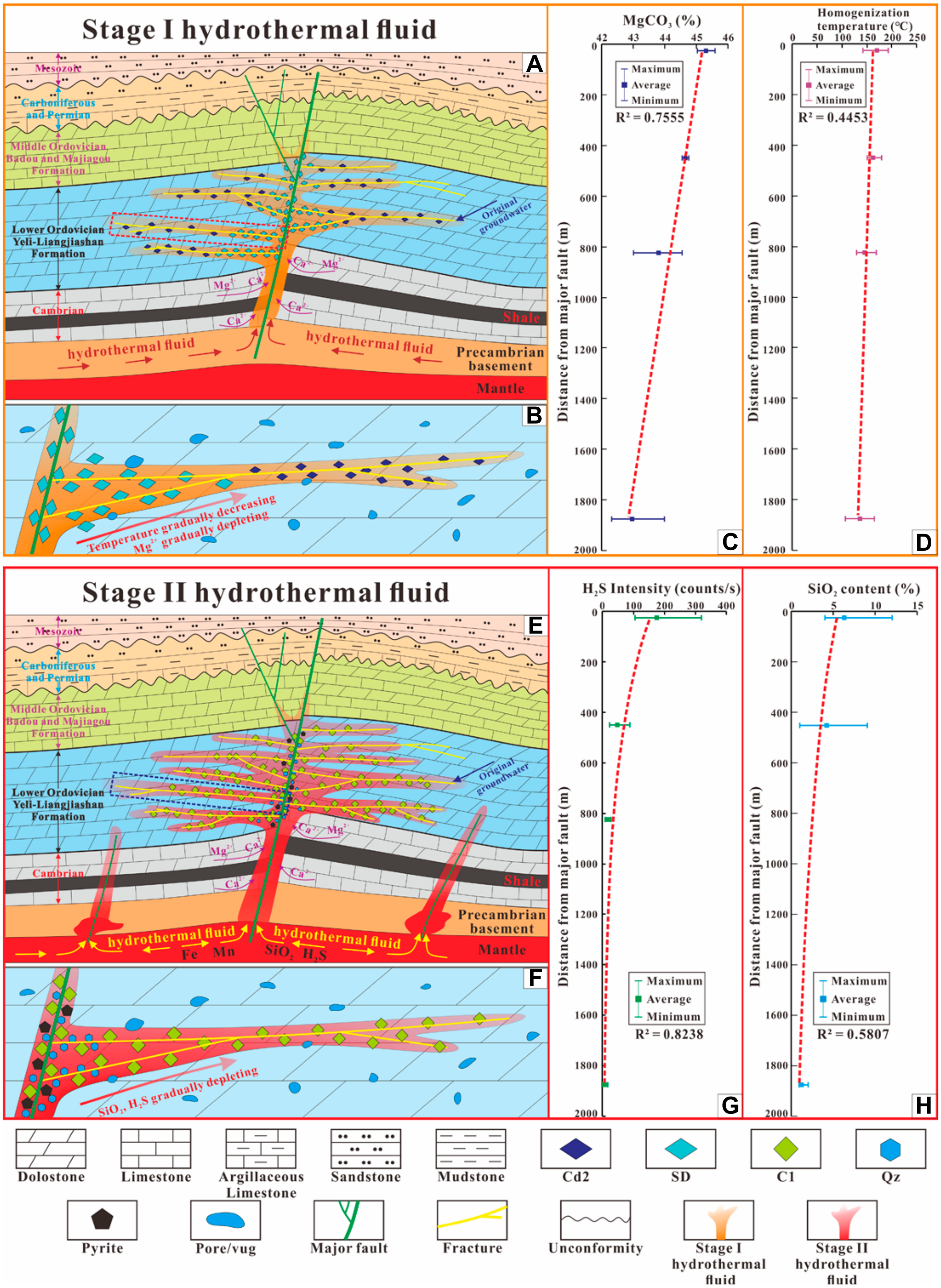

Figure 18. Migration and modification model of multistage hydrothermal fluids from the Precambrian basement or the mantle to the Yeli-Liangjiashan Formation. (A) Model for modification of dolomite reservoirs by stage I hydrothermal fluids. (B) Magnification of red dashed box in part A. (C) Concentration of $MgCO_3$ in SD/Cd2 (saddle dolomite/dolomite cement adjacent to Cd1) versus distance from the major faults. (D) Homogenization temperatures of the liquid-vapor two-phase aqueous inclusions (LVAIs) in SD/Cd2 versus distance from the major faults. (E) Model for modification of dolomite reservoirs by stage II hydrothermal fluids. (F) Magnification of the blue dashed box in part E. (G) The H_2S intensity of the LVAIs in first type of calcite (C1) versus distance from the major faults. (H) SiO_2 content (obtained by X-ray diffraction) in dolomite versus distance from the major faults. Qz—quartz.

mite reservoirs adjacent to the major faults, but dissolution was weakened or not visible away from the major faults. The influence of stage II hydrothermal fluids was primarily through the destructive filling of fractures and pores.

Hydrothermal fluids driven by geothermal and pressure gradients can migrate into fracture zones and permeable layers (Pan et al., 2021; Chen et al., 2022). However, as early overdolomitization and recrystallization densified the dolomite reservoir (Halley and Schmoker, 1983; Lucia and Major, 1994; Shen et al., 2019), later fractures represent crucial features as transport channels influencing the modification of the reservoir by hydrothermal fluids (Davies and Smith, 2006; Li et al., 2023). The development of strike-slip normal faults and the introduction of hydrothermal fluids may increase pressure and create fractures (Phillips, 1972; Katz et al., 2006; Centrella et al., 2022). At the microscopic level, microfractures are important pathways for the migration of hydrothermal fluids into formations and are crucial for hydrothermal fluids to modify pores (Martín-Martín et al., 2015; Guo et al., 2016; Li et al., 2023). Mf-I is almost fully filled and has relatively straight fracture edges (Figs. 9A and 9C), indicating that the influence of stage I hydrothermal fluids was predominantly precipitation. In contrast, the edges of Mf-II are uneven and not fully filled (Figs. 9A and 9F), indicating that both dissolution and precipitation occurred in stage II hydrothermal fluids. Only the pores/vugs connected by Mf-I could develop stage I hydrothermal precipitation (Figs. 9C–9E), and dissolved crystalline surfaces are visible in the pores connected by Mf-II (Figs. 9F–9H), indicating microfractures played a vital and critical role in hydrothermal modification.

6. CONCLUSIONS

(1) The genesis of pre-hydrothermal dolomites and Cd1 (the earliest-formed dolomite cement) was related to coeval seawater. Early dolomitization and pore formation predated multistage hydrothermal fluid activities. The pores were probably inherited from precursor limestones or formed during the earliest D1 stage of dolomitization.

(2) Two stages of hydrothermal fluids were identified in the Lower Ordovician Yeli-Liangjiashan Formation. Stage I and stage II hydrothermal fluids were derived from the Precambrian basement and the mantle, respectively. Stage I hydrothermal fluids mainly precipitated SD in the dolomite reservoirs adjacent to the major faults, while Cd2 was mainly precipitated in the dolomite reservoirs away from the major faults. The main precipitated minerals of the stage II hydrothermal fluids were C1, Qz, pyrite, and barite. As the distance from the major faults increased, the temperature of the hydrothermal fluids gradually became cooler, and SiO_2 and Mg were consumed continuously.

(3) Stage I hydrothermal fluids contained a relatively low amount of corrosive gas (H_2S). Cd1 shows complete crystal morphology without dissolution. SD and Cd2 significantly occupied the pores and fractures. The influence of stage I hydrothermal fluid on dolomite reservoirs was dominated by precipitation.

(4) Stage II hydrothermal fluids in the dolomite reservoirs adjacent to major faults caused dissolution owing to a relatively notable amount of H_2S. The H_2S-related dissolution is relatively limited in the pores. The secondary pores generated by H_2S-related dissolution are very few and much fewer than those generated by the pores prior to the precipitation of Cd1. As the distance from the major faults increased, the H_2S was gradually consumed. Dissolution is barely visible in the dolomite reservoirs away from the major faults. C1 followed the precipitated minerals in the stage I hydrothermal fluids and occupied most of the pores and fractures. Stage II hydrothermal fluids caused localized dissolution in dolomite reservoirs adjacent to major faults, but the influence of stage II hydrothermal fluid on the dolomite reservoirs was dominated by precipitation.

APPENDIX

The main geochemical data are included in Tables A1–A5: Table A1: In situ rare earth element (REE) data of dolomites. Table A2: In situ REE data of calcites. Table A3: In situ REE data of quartz (Qz). Table A4: C and O isotopic values of carbonate minerals. Table A5: In situ Sr isotopic values of carbonate minerals.

ACKNOWLEDGMENTS

This study was supported by the National Natural Science Foundation of China (grant no. 42272165). We would like to thank the Shengli Oilfield Company of SINOPEC for providing the core samples and geological data. We would like to thank the anonymous reviewers for their constructive comments.

REFERENCES CITED

Ahmad, W., Ullah, S., Ahmad, I., Gingras, M.K., Shafique, M., Khan, E.U., and Shah, M., 2021, Reflux dolomitization and subsequent hydrothermal dolomitization induced by the alkaline igneous province in the Middle Devonian Nowshera Formation (Peshawar Basin, NW Pakistan): Marine and Petroleum Geology, v. 131, p. 1–17, https://doi.org/10.1016/j.marpetgeo.2021.105178.

Al-Aasm, I., 2003, Origin and characterization of hydrothermal dolomite in the Western Canada sedimentary basin: Journal of Geochemical Exploration, v. 78–79, p. 9–15, https://doi.org/10.1016/S0375-6742(03)00089-X.

Al-Aasm, I.S., Lonnee, J., and Clarke, J., 2002, Multiple fluid flow events and the formation of saddle dolomite: Case studies from the Middle Devonian of the Western Canada sedimentary basin: Marine and Petroleum Geology, v. 19, p. 209–217, https://doi.org/10.1016/S0264-8172(02)00013-2.

Anders, M.H., Laubach, S.E., and Scholz, C.H., 2014, Microfractures: A review: Journal of Structural Geology, v. 69, p. 377–394, https://doi.org/10.1016/j.jsg.2014.05.011.

Bai, C., Yu, B., Liu, H., Xie, Z., Han, S., Zhang, L., Ye, R., and Ge, J., 2018, The genesis and evolution of carbonate minerals in shale oil formations from Dongying depression, Bohai Bay Basin, China: International Journal of Coal Geology, v. 189, p. 8–26, https://doi.org/10.1016/j.coal.2018.02.008.

Bau, M., 1991, Rare-earth element mobility during hydrothermal and metamorphic fluid-rock interaction and the significance of the oxidation state of europium: Chemical Geology, v. 93, p. 219–230, https://doi.org/10.1016/0009-2541(91)90115-8.

Bau, M., and Dulski, P., 1996, Distribution of yttrium and rare-earth elements in the Penge and Kuruman iron-formations, Transvaal Supergroup, South Africa: Precambrian Research, v. 79, p. 37–55, https://doi.org/10.1016/0301-9268(95)00087-9.

Bau, M., and Möller, P., 1993, Rare earth element systematics of the chemically precipitated component in early Precambrian iron formations and the evolution of the terrestrial atmosphere-hydrosphere-lithosphere system: Geochimica et Cosmochimica Acta, v. 57, p. 2239–2249, https://doi.org/10.1016/0016-7037(93)90566-F.

Bau, M., Balan, S., Schmidt, K., and Koschinsky, A., 2010, Rare earth elements in mussel shells of the Mytilidae family as tracers for hidden and fossil high-temperature hydrothermal systems: Earth and Planetary Science Letters, v. 299, p. 310–316, https://doi.org/10.1016/j.epsl.2010.09.011.

Biehl, B.C., Reuning, L., Schoenherr, J., Lewin, A., Leupold, M., and Kukla, P.A., 2016, Do CO_2-charged fluids contribute to secondary porosity creation in deeply buried carbonates?: Marine and Petroleum Geology, v. 76, p. 176–186, https://doi.org/10.1016/j.marpetgeo.2016.05.005.

Bolhar, R., and Vankranendonk, M., 2007, A non-marine depositional setting for the northern Fortescue Group, Pilbara craton, inferred from trace element geochemistry of stromatolitic carbonates: Precambrian Research, v. 155, p. 229–250, https://doi.org/10.1016/j.precamres.2007.02.002.

Burke, W.H., Denison, R.E., Hetherington, E.A., Koepnick, R.B., Nelson, H.F., and Otto, J.B., 1982, Variation of seawater $^{87}Sr/^{86}Sr$ throughout Phanerozoic time: Geology, v. 10, p. 516–519, https://doi.org/10.1130/0091-7613(1982)10<516:VOSSTP>2.0.CO;2.

Cai, C., Hu, W., and Worden, R.H., 2001, Thermochemical sulphate reduction in Cambro-Ordovician carbonates in central Tarim: Marine and Petroleum Geology, v. 18, p. 729–741, https://doi.org/10.1016/S0264-8172(01)00028-9.

Cai, C., Li, K., Li, H., and Zhang, B., 2008, Evidence for cross formational hot brine flow from integrated $^{87}Sr/^{86}Sr$, REE and fluid inclusions of the Ordovician veins in central Tarim, China: Applied Geochemistry, v. 23, p. 2226–2235, https://doi.org/10.1016/j.apgeochem.2008.03.009.

Cai, C., Zhang, C., He, H., and Tang, Y., 2013, Carbon isotope fractionation during methane-dominated TSR in East Sichuan Basin gasfields, China: A review: Marine and Petroleum Geology, v. 48, p. 100–110, https://doi.org/10.1016/j.marpetgeo.2013.08.006.

Centrella, S., Beaudoin, N.E., Koehn, D., Motte, G., Hoareau, G., and Callot, J.P., 2022, How fluid-mediated rock transformations can mimic hydro-fracturing patterns in hydrothermal dolomite: Marine and Petroleum Geology, v. 140, https://doi.org/10.1016/j.marpetgeo.2022.105657.

Chen, H., Lu, Z., Cao, Z., Han, J., and Yun, L., 2015, Hydrothermal alteration of Ordovician reservoir in northeastern slope of Tazhong uplift, Tarim Basin: Acta Petrolei Sinica, v. 37, no. 1, p. 43–63, https://doi.org/10.7623/syxb201601004.

Chen, L., Liu, Y., Hu, Z., Gao, S., Zong, K., and Chen, H., 2011, Accurate determinations of fifty-four major and trace elements in carbonate by LA-ICP-MS using normalization strategy of bulk components as 100%: Chemical Geology, v. 284, p. 283–295, https://doi.org/10.1016/j.chemgeo.2011.03.007.

Chen, L., Zhang, H., Cai, Z., Hao, F., Xue, Y., and Zhao, W., 2022, Petrographic, mineralogical and geochemical constraints on the fluid origin and multistage karstification of the Middle–Lower Ordovician carbonate reservoir, NW Tarim Basin, China: Journal of Petroleum Science Engineering, v. 208, https://doi.org/10.1016/j.petrol.2021.109561.

Cheng, Y., Wu, Z., Su, W., Chen, M., Zhang, J., Liu, Y., and Wu, Q., 2023, Basement structures exert a crucial influence on the structural configuration of later rift development: Insights from the Shanan and Chengbei sag, Bohai Bay Basin: Marine and Petroleum Geology, v. 153, https://doi.org/10.1016/j.marpetgeo.2023.106272.

Davies, G.R., 1997, The Triassic of the Western Canada sedimentary basin: Tectonic and stratigraphic framework, paleogeography, paleoclimate and biota: Bulletin of Canadian Petroleum Geology, v. 45, p. 434–460, https://doi.org/10.35767/gscpgbull.45.4.434.

Davies, G.R., and Smith, L.B., Jr., 2006, Structurally controlled hydrothermal dolomite reservoir facies: An overview: American Association of Petroleum Geologists Bulletin, v. 90, p. 1641–1690, https://doi.org/10.1306/05220605164.

Dickson, J.A.D., 1966, Carbonate identification and genesis as revealed by staining: Journal of Sedimentary Research, v. 36, p. 491–505, https://doi.org/10.1306/74D714F6-2B21-11D7-8648000102C1865D.

Dong, S., Chen, D., Qing, H., Zhou, X., Wang, D., Guo, Z., Jiang, M., and Qian, Y., 2013, Hydrothermal alteration of dolostones in the Lower Ordovician, Tarim Basin, NW China: Multiple constraints from petrology, isotope geochemistry and fluid inclusion microthermometry: Marine and Petroleum Geology, v. 46, p. 270–286, https://doi.org/10.1016/j.marpetgeo.2013.06.013.

Douville, E., Charlou, J.L., Oelkers, E.H., Bienvenu, P., Jove Colon, C.F., Donval, J.P., Fouquet, Y., Prieur,

TABLE A1. IN SITU RARE EARTH ELEMENT (REE) DATA OF DOLOMITES, YELI-LIANGJIASHAN FORMATION, CHENGDAO-ZHUANGHAI AREA, CHINA

Well	Depth (m)	Lithology	La	Ce	Pr	Nd	Sm	Eu	Gd	Tb	Dy	Ho	Er	Tm	Yb	Lu	ΣREE	ΣLREE	ΣMREE	ΣHREE	LREE/ MREE	δEu	δCe
ZH102	4623.56	D1	0.73	1.09	0.23	1.14	0.50	0.11	0.42	0.07	0.28	0.06	0.19	0.05	0.33	0.04	5.24	3.19	1.37	0.67	2.32	1.15	0.40
ZH102	4624.66	D1	0.51	0.86	0.20	1.12	0.44	0.13	0.33	0.04	0.28	0.05	0.19	0.03	0.28	0.03	4.52	2.69	1.24	0.59	2.17	1.72	0.34
ZG28	4137.93	D1	0.50	1.12	0.26	1.30	0.41	0.10	0.38	0.06	0.32	0.07	0.20	0.05	0.23	0.04	5.02	3.18	1.27	0.58	2.50	1.26	0.31
ZG28	4137.93	D1	0.44	0.80	0.20	1.14	0.46	0.09	0.37	0.06	0.29	0.07	0.21	0.04	0.33	0.04	4.53	2.59	1.27	0.67	2.03	1.02	0.29
ZG28	4133.78	D1	0.53	0.78	0.17	1.07	0.45	0.11	0.34	0.05	0.35	0.06	0.18	0.04	0.23	0.05	4.41	2.55	1.30	0.56	1.96	1.34	0.39
ZG28	4133.87	D1	0.44	0.59	0.17	0.96	0.44	0.14	0.32	0.05	0.32	0.06	0.17	0.03	0.21	0.03	3.94	2.16	1.27	0.50	1.70	1.72	0.28
ZG28	4132.83	D1	0.48	0.63	0.17	0.99	0.41	0.10	0.33	0.05	0.27	0.05	0.15	0.04	0.25	0.04	3.96	2.27	1.16	0.53	1.96	1.22	0.31
CB244	2920.60	D1	0.65	1.05	0.23	1.28	0.53	0.09	0.42	0.06	0.34	0.09	0.19	0.03	0.30	0.04	5.30	3.21	1.44	0.65	2.24	0.97	0.37
CB244	2920.60	D1	0.41	0.55	0.16	0.88	0.48	0.10	0.48	0.07	0.34	0.09	0.23	0.05	0.27	0.05	4.13	1.99	1.46	0.68	1.36	1.05	0.28
CB244	2925.27	D1	0.47	0.93	0.23	1.09	0.46	0.15	0.44	0.06	0.38	0.09	0.23	0.06	0.29	0.05	4.92	2.71	1.48	0.73	1.83	1.69	0.30
ZG28	4122.92	D2	3.55	7.48	0.87	3.82	0.75	0.14	0.70	0.10	0.57	0.11	0.28	0.05	0.30	0.04	18.74	15.72	2.26	0.77	6.97	0.98	0.91
ZG28	4122.92	D2	3.80	7.72	0.87	3.20	0.70	0.17	0.51	0.08	0.57	0.14	0.39	0.04	0.34	0.04	18.57	15.59	2.03	0.96	7.68	1.28	1.00
ZG28	4126.87	D2	3.88	7.74	0.85	3.04	0.56	0.13	0.48	0.07	0.44	0.09	0.28	0.05	0.31	0.04	17.95	15.50	1.68	0.77	9.21	1.17	1.06
ZH102	4622.26	D2	5.00	10.42	1.21	4.66	1.00	0.18	0.90	0.13	0.70	0.13	0.29	0.06	0.26	0.05	24.97	21.28	2.90	0.79	7.33	0.95	0.92
ZH102	4622.26	D2	3.21	7.62	0.84	3.07	0.62	0.11	0.50	0.06	0.54	0.09	0.24	0.04	0.26	0.04	17.25	14.74	1.84	0.67	8.01	1.05	0.90
ZH102	4622.92	D3	1.29	3.25	0.36	1.77	0.40	0.08	0.36	0.04	0.39	0.07	0.14	0.03	0.17	0.03	8.38	6.68	1.27	0.430	5.26	1.15	0.85
ZH102	4623.56	D3	1.27	2.61	0.28	1.20	0.29	0.06	0.21	0.04	0.23	0.05	0.15	0.02	0.12	0.01	6.55	5.36	0.83	0.362	6.49	1.11	1.09
ZH102	4623.56	D3	1.80	3.91	0.42	1.83	0.39	0.08	0.36	0.04	0.28	0.07	0.15	0.03	0.15	0.02	9.52	7.95	1.15	0.416	6.92	1.10	1.04
CB244	2914.37	D3	1.80	3.73	0.36	1.41	0.32	0.04	0.23	0.03	0.24	0.04	0.11	0.02	0.11	0.01	8.47	7.30	0.87	0.301	8.41	0.77	1.34
CB244	2904.67	D3	1.64	3.25	0.34	1.28	0.24	0.05	0.21	0.03	0.21	0.04	0.10	0.02	0.07	0.02	7.50	6.51	0.75	0.247	8.71	1.15	1.22
CB244	2906.47	D3	1.37	2.38	0.30	1.17	0.26	0.05	0.22	0.04	0.23	1.76	0.05	0.15	0.02	0.14	6.41	5.22	0.80	0.39	6.53	0.96	0.97
CB244	2903.77	D3	0.94	1.79	0.22	0.99	0.20	0.04	0.16	0.03	0.24	1.37	0.05	0.15	0.02	0.17	5.02	3.93	0.68	0.41	5.81	0.87	0.88
CB302	4005.45	D3	1.17	2.43	0.28	1.22	0.24	0.06	0.21	0.03	0.19	1.24	0.04	0.14	0.02	0.13	6.18	5.10	0.73	0.35	6.98	1.21	0.93
CB302	4007.76	D3	1.18	2.37	0.28	1.03	0.22	0.05	0.22	0.04	0.20	1.22	0.04	0.14	0.01	0.11	5.90	4.85	0.73	0.31	6.60	1.16	0.93
CB302	4001.96	D4	0.95	1.98	0.19	0.75	0.14	0.02	0.17	0.01	0.16	0.03	0.06	0.01	0.04	0.00	4.51	3.87	0.50	0.14	7.78	0.72	1.31
CB302	4001.96	D4	0.87	1.77	0.19	0.58	0.17	0.03	0.16	0.02	0.10	0.03	0.07	0.00	0.05	0.01	4.06	3.41	0.48	0.17	7.17	0.84	1.10
CB302	4003.50	D4	1.10	2.27	0.27	1.16	0.18	0.04	0.18	0.03	0.21	0.03	0.10	0.02	0.10	0.01	5.69	4.80	0.64	0.25	7.50	0.98	0.87
CB302	4004.00	D4	0.88	1.81	0.21	0.97	0.15	0.05	0.13	0.03	0.15	0.03	0.10	0.02	0.10	0.01	4.64	3.87	0.51	0.26	7.65	1.51	0.92
ZH102	4622.66	D4	1.00	1.95	0.21	0.86	0.13	0.03	0.14	0.02	0.13	0.78	0.03	0.08	0.01	0.06	4.67	4.02	0.46	0.19	8.78	1.22	1.09
ZH102	4622.66	D4	0.89	1.79	0.18	0.71	0.20	0.04	0.11	0.02	0.14	0.79	0.02	0.05	0.01	0.06	4.24	3.56	0.52	0.16	6.88	1.10	1.22
CB244	2903.77	Cd1	0.70	1.54	0.18	0.81	0.20	0.03	0.12	0.03	0.16	0.04	0.09	0.01	0.06	0.01	3.98	3.24	0.53	0.21	6.11	0.82	0.87
CB244	2903.77	Cd1	0.73	1.58	0.19	0.89	0.26	0.06	0.23	0.03	0.21	0.04	0.10	0.02	0.09	0.01	4.44	3.39	0.79	0.26	4.32	1.29	0.87
CB244	2914.37	Cd1	0.82	1.82	0.21	0.96	0.17	0.04	0.17	0.02	0.17	0.03	0.08	0.01	0.06	0.01	4.56	3.81	0.57	0.19	6.68	1.35	0.87
CB244	2914.37	Cd1	0.80	1.74	0.21	0.78	0.15	0.04	0.19	0.03	0.20	0.04	0.11	0.02	0.09	0.02	4.42	3.53	0.61	0.27	5.74	1.25	0.79
ZG28	4122.92	Cd1	0.87	1.84	0.20	0.76	0.20	0.03	0.19	0.03	0.19	0.04	0.11	0.01	0.11	0.01	4.59	3.67	0.64	0.28	5.76	0.79	1.01
ZG28	4122.92	Cd1	0.69	1.66	0.19	0.85	0.23	0.05	0.16	0.03	0.18	0.04	0.12	0.01	0.08	0.01	4.32	3.40	0.65	0.26	5.24	1.09	0.80
ZH102	4623.36	Cd1	1.14	2.71	0.28	1.19	0.25	0.06	0.20	0.03	0.21	0.05	0.10	0.01	0.12	0.01	6.35	5.32	0.74	0.29	7.19	1.23	0.98
ZH102	4623.36	Cd1	1.28	2.58	0.26	1.05	0.29	0.05	0.20	0.03	0.19	0.04	0.10	0.02	0.09	0.01	6.18	5.17	0.75	0.26	6.85	0.88	1.28
CB244	2914.37	Cd1	1.23	2.48	0.29	1.00	0.21	0.05	0.16	0.02	0.18	0.03	0.07	0.01	0.08	0.01	5.83	5.00	0.62	0.21	7.99	1.19	0.93
CB244	2914.37	Cd1	1.40	2.93	0.31	1.17	0.25	0.04	0.21	0.03	0.19	0.04	0.10	0.02	0.08	0.01	6.79	5.81	0.73	0.25	7.92	0.94	1.09
CB302	4002.36	Cd1	1.66	3.22	0.36	1.16	0.23	0.05	0.17	0.03	0.16	0.03	0.10	0.01	0.08	0.01	7.28	6.39	0.65	0.25	9.91	1.10	1.09
CB302	4002.36	Cd1	1.27	2.42	0.25	1.02	0.20	0.04	0.21	0.03	0.18	0.04	0.09	0.01	0.08	0.01	5.85	4.96	0.66	0.23	7.47	0.98	1.25
CB302	4007.76	Cd1	1.00	1.87	0.21	0.90	0.20	0.04	0.18	0.03	0.17	0.04	0.10	0.01	0.11	0.02	4.89	3.98	0.62	0.28	6.38	1.13	1.12
CBG6	3037.7	Cd2	0.01	0.08	0.03	0.39	0.48	0.10	0.59	0.07	0.49	0.07	0.20	0.03	0.14	0.02	2.70	0.51	1.74	0.44	0.30	1.06	0.16
CBG6	3039.7	Cd2	0.02	0.06	0.02	0.15	0.10	0.02	0.13	0.01	0.14	0.04	0.11	0.02	0.07	0.01	0.90	0.25	0.40	0.25	0.63	1.22	0.23
CB302	4002.36	Cd2	0.01	0.10	0.04	0.32	0.44	0.09	0.41	0.05	0.27	0.05	0.14	0.02	0.09	0.01	2.03	0.46	1.26	0.31	0.37	1.10	0.16
CB302	4002.36	Cd2	0.01	0.11	0.03	0.28	0.13	0.03	0.16	0.02	0.17	0.02	0.08	0.01	0.05	0.01	1.12	0.43	0.52	0.17	0.84	1.07	0.22
CB302	4007.76	Cd2	0.01	0.03	0.01	0.15	0.08	0.02	0.13	0.02	0.11	0.02	0.05	0.01	0.04	0.00	0.69	0.19	0.37	0.12	0.52	1.37	0.21
CB302	4007.76	Cd2	0.03	0.19	0.05	0.75	0.46	0.08	0.42	0.06	0.31	0.05	0.14	0.02	0.11	0.02	2.70	1.03	1.34	0.33	0.77	0.89	0.21
ZH102	4623.36	Cd2	0.00	0.04	0.01	0.13	0.20	0.05	0.37	0.07	0.42	0.08	0.18	0.03	0.18	0.03	1.79	0.18	1.11	0.50	0.16	0.94	0.26
ZH102	4623.36	Cd2	0.05	0.27	0.05	0.43	0.32	0.07	0.38	0.06	0.38	0.08	0.23	0.03	0.22	0.03	2.60	0.81	1.21	0.58	0.67	0.94	0.31
ZH102	4624.26	Cd2	0.02	0.11	0.03	0.26	0.29	0.07	0.34	0.03	0.19	0.03	0.07	0.01	0.05	0.00	1.50	0.43	0.92	0.15	0.46	1.25	0.25
ZH102	4624.26	Cd2	0.05	0.26	0.08	0.76	0.27	0.07	0.29	0.02	0.20	0.02	0.05	0.01	0.03	0.01	2.13	1.16	0.85	0.12	1.35	1.41	0.19
ZH102	4623.86	Cd2	0.01	0.06	0.03	0.28	0.36	0.06	0.29	0.04	0.21	0.03	0.10	0.01	0.09	0.01	1.59	0.39	0.96	0.24	0.41	0.94	0.13
ZH102	4623.86	Cd2	0.02	0.09	0.03	0.24	0.27	0.07	0.33	0.04	0.25	0.04	0.12	0.01	0.11	0.02	1.63	0.37	0.95	0.30	0.39	1.42	0.20
CB302	4005.45	Cd2	0.01	0.05	0.01	0.21	0.17	0.04	0.21	0.02	0.14	0.02	0.07	0.01	0.04	0.01	1.02	0.28	0.58	0.15	0.49	1.20	0.22
CB302	4006.67	Cd2	0.01	0.04	0.01	0.14	0.06	0.01	0.08	0.01	0.05	0.01	0.03	0.00	0.04	0.00	0.49	0.20	0.21	0.08	0.94	1.10	0.18
ZG28	4122.92	SD	0.01	0.06	0.02	0.13	0.17	0.05	0.15	0.02	0.14	0.03	0.06	0.01	0.03	0.01	0.90	0.22	0.54	0.14	0.41	1.38	0.18
CB244	2914.37	SD	0.10	0.25	0.05	0.21	0.06	0.03	0.04	0.01	0.09	0.01	0.01	0.01	0.00	0.00	0.87	0.62	0.22	0.03	2.86	2.29	0.36
CB244	2914.37	SD	0.01	0.05	0.00	0.06	0.03	0.01	0.04	0.00	0.03	0.01	0.01	0.00	0.02	0.00	0.27	0.12	0.11	0.04	1.09	2.38	1.04
CB244	2914.37	SD	0.01	0.04	0.01	0.13	0.03	0.02	0.04	0.01	0.05	0.01	0.02	0.00	0.01	0.00	0.38	0.19	0.14	0.05	1.36	2.66	0.30
CB244	2914.37	SD	0.01	0.09	0.03	0.18	0.06	0.04	0.16	0.02	0.09	0.02	0.04	0.01	0.07	0.01	0.82	0.30	0.36	0.15	0.83	2.70	0.20
ZG28	4122.92	SD	0.02	0.03	0.02	0.18	0.22	0.06	0.25	0.03	0.18	0.04	0.13	0.01	0.14	0.02	1.34	0.25	0.76	0.34	0.32	1.48	0.09
ZG28	4123.42	SD	0.15	0.94	0.21	1.61	0.83	0.15	0.66	0.08	0.54	0.08	0.23	0.03	0.14	0.02	5.67	2.92	2.26	0.49	1.29	1.06	0.27
ZG28	4123.42	SD	0.10	0.63	0.17	1.61	0.71	0.12	0.64	0.07	0.43	0.08	0.20	0.02	0.09	0.02	4.89	2.52	1.96	0.41	1.28	0.94	0.22
CB244	2906.47	SD	0.17	1.01	0.25	1.88	0.73	0.14	0.60	0.08	0.47	0.09	0.23	0.02	0.12	0.02	5.81	3.31	2.02	0.48	1.63	1.08	0.24
CB244	2906.47	SD	0.19	1.10	0.26	2.00	0.75	0.17	0.69	0.09	0.50	0.09	0.19	0.03	0.13	0.02	6.20	3.55	2.20	0.45	1.61	1.27	0.26
CB244	2903.77	SD	0.14	0.73	0.18	1.48	0.70	0.15	0.61	0.08	0.44	0.07	0.18	0.02	0.11	0.01	4.91	2.53	1.99	0.39	1.27	1.14	0.25
CB244	2903.77	SD	0.20	0.93	0.23	1.38	0.53	0.13	0.50	0.07	0.46	0.09	0.21	0.03	0.15	0.02	4.91	2.73	1.69	0.49	1.61	1.26	0.25
CB244	2899.19	SD	0.08	0.61	0.17	1.19	0.54	0.10	0.49	0.06	0.40	0.08	0.18	0.02	0.14	0.02	4.09	2.05	1.60	0.44	1.29	1.03	0.21

Note: Values for individual elements are given in ppm. Lithologies: D1—relict grains of the dolorudstones; D2, D3, and D4—matrices of fine crystalline dolostone (FCD), fine to medium crystalline dolostone (FMCD), and medium to coarse crystalline dolostone (MCCD), respectively; Cd1, Cd2—earliest-formed dolomite cement and dolomite cement adjacent to Cd1, respectively; SD—saddle dolomite. Refer to Section 3 for the method of REE normalization and calculation of REE anomalies. L/M/HREE—light/middle/heavy rare earth elements.

TABLE A2. IN SITU RARE EARTH ELEMENT DATA OF CALCITES, YELI-LIANGJIASHAN FORMATION, CHENGDAO-ZHUANGHAI AREA, CHINA

Well	Depth (m)	Lithology	La	Ce	Pr	Nd	Sm	Eu	Gd	Tb	Dy	Ho	Er	Tm	Yb	Lu	δEu
CB244	2903.77	C1	1.93	5.71	0.81	4.44	1.57	0.42	1.48	0.18	0.93	0.15	0.42	0.05	0.30	0.03	1.47
CB244	2903.77	C1	7.33	22.82	3.11	14.44	4.55	1.26	4.20	0.50	2.38	0.40	0.92	0.11	0.62	0.08	1.53
CB244	2906.47	C1	0.27	1.62	0.34	2.37	1.05	0.25	0.76	0.08	0.49	0.07	0.17	0.02	0.12	0.01	1.41
CB244	2906.47	C1	0.04	0.14	0.03	0.20	0.09	0.04	0.10	0.02	0.10	0.02	0.04	0.01	0.05	0.01	2.16
CB244	2914.37	C1	0.44	1.96	0.53	4.41	2.33	0.74	2.28	0.27	1.61	0.26	0.62	0.07	0.36	0.05	1.73
CB244	2914.37	C1	2.20	7.71	1.30	7.29	2.65	0.73	2.44	0.34	2.04	0.38	1.02	0.13	0.78	0.10	1.46
CB244	2914.37	C1	0.39	0.94	0.20	1.68	0.99	0.41	1.04	0.11	0.56	0.11	0.21	0.03	0.15	0.02	2.31
CB302	4002.36	C1	5.01	13.58	1.87	8.56	3.32	1.03	3.13	0.35	1.86	0.33	0.76	0.08	0.45	0.06	1.74
CB302	4002.36	C1	3.25	10.72	1.83	11.01	5.00	1.58	4.25	0.50	2.70	0.43	1.03	0.12	0.66	0.09	1.79
ZG28	4122.92	C1	0.73	2.67	0.49	3.52	1.77	0.51	1.59	0.20	1.03	0.17	0.36	0.06	0.29	0.05	1.58
ZG28	4123.42	C1	4.56	10.52	1.33	5.96	1.56	0.30	1.59	0.22	1.26	0.25	0.63	0.09	0.47	0.07	0.99
ZG28	4123.42	C1	4.10	12.27	1.77	7.99	2.00	0.38	1.74	0.23	1.11	0.20	0.46	0.05	0.29	0.04	1.03
CB302	4006.67	C1	12.75	28.33	3.83	17.51	4.25	0.81	3.76	0.47	2.62	0.44	1.14	0.15	0.82	0.12	1.04
CB302	4007.76	C1	16.90	37.41	4.71	20.38	4.32	0.77	3.34	0.42	2.12	0.39	1.04	0.13	0.78	0.12	1.02
ZH102	4624.26	C2	0.17	0.78	0.16	1.03	0.49	0.09	0.43	0.08	0.50	0.07	0.21	0.03	0.12	0.02	0.93
ZH102	4623.86	C2	0.27	1.14	0.19	1.14	0.44	0.08	0.40	0.06	0.35	0.07	0.16	0.02	0.10	0.02	1.00
ZH102	4624.26	C2	0.20	0.90	0.17	1.33	0.64	0.10	0.61	0.10	0.59	0.11	0.30	0.04	0.28	0.03	0.78
CB302	4005.45	C2	0.31	1.77	0.43	2.52	0.50	0.07	0.40	0.06	0.37	0.06	0.16	0.02	0.15	0.02	0.72
CB302	4006.67	C2	0.28	1.86	0.46	3.45	0.75	0.12	0.66	0.08	0.59	0.11	0.27	0.03	0.23	0.02	0.91
CB302	4007.76	C2	0.15	0.89	0.31	3.54	3.90	0.64	3.12	0.32	1.45	0.20	0.37	0.04	0.21	0.04	0.98

Note: Values for individual elements are given in ppm. Lithologies: C1, C2—first and second type of calcite, respectively.

TABLE A3. IN SITU RARE EARTH ELEMENT DATA OF QUARTZ (QZ), YELI-LIANGJIASHAN FORMATION, CHENGDAO-ZHUANGHAI AREA, CHINA

Well	Depth (m)	Lithology	La	Ce	Pr	Nd	Sm	Eu	Gd	Tb	Dy	Ho	Er	Tm	Yb	Lu	δEu
CB244	2903.77	Qz	0.107	0.168	0.013	0.061	0.012	0.014	0.022	0.003	0.018	0.003	0.000	0.001	0.008	0.003	4.750
CB244	2906.47	Qz	0.333	0.761	0.100	0.797	0.107	0.020	0.016	0.006	0.009	0.000	0.000	0.004	0.025	0.000	1.199
CB244	2914.37	Qz	0.291	0.557	0.072	0.242	0.029	0.009	0.005	0.001	0.008	0.003	0.005	0.000	0.008	0.002	2.081
CB244	2914.37	Qz	5.523	5.705	0.008	0.011	0.012	0.005	0.008	0.002	0.010	0.003	0.014	0.003	0.129	0.012	1.885
ZG28	4122.92	Qz	0.014	0.014	0.001	0.008	0.006	0.003	0.003	0.000	0.006	0.000	0.001	0.000	0.003	0.000	2.757
ZG28	4123.42	Qz	0.554	1.034	0.177	0.652	0.080	0.042	0.099	0.013	0.100	0.011	0.042	0.003	0.007	0.010	2.559
ZG28	4123.42	Qz	0.003	0.008	0.000	0.023	0.004	0.001	0.003	0.000	0.000	0.000	0.000	0.000	0.000	0.000	1.555
ZH102	4623.86	Qz	0.001	0.006	0.001	0.005	0.004	0.001	0.007	0.000	0.000	0.000	0.000	0.000	0.006	0.000	1.558
ZH102	4623.86	Qz	0.447	0.866	0.094	0.382	0.081	0.021	0.060	0.009	0.053	0.012	0.030	0.005	0.025	0.002	1.422

Note: Values for individual elements are given in ppm.

D., and Appriou, P., 2002, The Rainbow vent fluids (36°14′N, MAR): The influence of ultramafic rocks and phase separation on trace metal content in Mid-Atlantic Ridge hydrothermal fluids: Chemical Geology, v. 184, p. 37–48, https://doi.org/10.1016/S0009-2541(01)00351-5.

Du, Y., Fan, T., Machel, H.G., and Gao, Z., 2018, Genesis of Upper Cambrian–Lower Ordovician dolomites in the Tahe oilfield, Tarim Basin, NW China: Several limitations from petrology, geochemistry, and fluid inclusions: Marine and Petroleum Geology, v. 91, p. 43–70, https://doi.org/10.1016/j.marpetgeo.2017.12.023.

Ehrenberg, S.N., and Bjørlykke, K., 2016, Comments regarding hydrothermal dolomitization and porosity development in the paper "Formation mechanism of deep Cambrian dolomite reservoirs in the Tarim Basin, northwestern China" by Zhu et al. (2015): Marine and Petroleum Geology, v. 76, p. 480–481, https://doi.org/10.1016/j.marpetgeo.2015.09.008.

Ehrenberg, S.N., Walderhaug, O., and Bjørlykke, K., 2012, Carbonate porosity creation by mesogenetic dissolution: Reality or illusion?: American Association of Petroleum Geologists Bulletin, v. 96, p. 217–233, https://doi.org/10.1306/05031110187.

Ehrenberg, S.N., Walderhaug, O., and Bjørlykke, K., 2019, Discussion of "Microfacies, diagenesis and oil emplacement of the Upper Jurassic Arab-D carbonate reservoir in an oil field in central Saudi Arabia (Khurais Complex)" by Rosales et al. (2018): Marine and Petroleum Geology, v. 100, p. 551–553, https://doi.org/10.1016/j.marpetgeo.2018.11.041.

Frei, R., Døssing, L.N., Gaucher, C., Boggiani, P.C., Frei, K.M., Bech Árting, T., Crowe, S.A., and Freitas, B.T., 2017, Extensive oxidative weathering in the aftermath of a late Neoproterozoic glaciation—Evidence from trace element and chromium isotope records in the Urucum district (Jacadigo Group) and Puga iron formations (Mato Grosso do Sul, Brazil): Gondwana Research, v. 49, p. 1–20, https://doi.org/10.1016/j.gr.2017.05.003.

Friedman, I., and O'Neil, J.R., 1977, Compilation of Stable Isotope Fractionation Factors of Geochemical Interest: U.S. Geological Survey Professional Paper 440-KK, 11 p., https://doi.org/10.3133/pp440KK.

Frimmel, H.E., 2009, Trace element distribution in Neoproterozoic carbonates as palaeoenvironmental indicator: Chemical Geology, v. 258, p. 338–353, https://doi.org/10.1016/j.chemgeo.2008.10.033.

Gao, J.F., and Zhou, M.F., 2013, Generation and evolution of siliceous high magnesium basaltic magmas in the formation of the Permian Huangshandong intrusion (Xinjiang, NW China): Lithos, v. 162–163, p. 128–139, https://doi.org/10.1016/j.lithos.2013.01.002.

Gasparrini, M., Morad, D., Mangenot, X., Bonifacie, M., Morad, S., Nader, F.H., and Gerdes, A., 2023, Dolomite recrystallization revealed by Δ_{47}/U-Pb thermochronometry in the Upper Jurassic Arab Formation, United Arab Emirates: Geology, v. 51, p. 471–475, https://doi.org/10.1130/G50960.1.

Gigoux, M., Brigaud, B., Pagel, M., Delpech, G., Guerrot, C., Augé, T., and Négrel, P., 2016, Genetic constraints on world-class carbonate- and siliciclastic-hosted stratabound fluorite deposits in Burgundy (France) inferred from mineral paragenetic sequence and fluid inclusion studies: Ore Geology Reviews, v. 72, p. 940–962, https://doi.org/10.1016/j.oregeorev.2015.09.013.

Goldstein, R.H., and Reynolds, T.J., 1994, Fluid inclusion microthermometry, *in* Goldstein, R.H., and Reynolds, T.J., eds., Systematics of Fluid Inclusions in Diagenetic Minerals: Society for Sedimentary Geology (SEPM) Short Course 31, p. 87–121, https://doi.org/10.2110/scn.94.31.

Gregg, J.M., and Sibley, D.F., 1984, Epigenetic dolomitization and the origin of xenotopic dolomite texture: Journal of Sedimentary Research, v. 54, p. 908–931, https://doi.org/10.1306/212F8535-2B24-11D7-8648000102C1865D.

Guo, C., Chen, D., Qing, H., Dong, S., Li, G., Wang, D., Qian, Y., and Liu, C., 2016, Multiple dolomitization and later hydrothermal alteration on the Upper Cambrian–Lower Ordovician carbonates in the northern Tarim Basin, China: Marine and Petroleum Geology, v. 72, p. 295–316, https://doi.org/10.1016/j.marpetgeo.2016.01.023.

Guo, R., Zhang, S., Wang, K., Han, M., and Ding, X., 2021, Multiphase dolomitization and hydrothermal alteration of the Upper Cambrian–Lower Ordovician carbonates in the Gucheng uplift, Tarim Basin (NW China): Journal of Petroleum Science Engineering, v. 206, https://doi.org/10.1016/j.petrol.2021.108964.

Guo, Y., 2021, A study on constructive diagenesis of the dolomite reservoir within the Yeli-Liangjiashan Formation in the Zhuanghai area of Jiyang Depression: Acta Mineralogica Sinica, v. 41, no. 2, p. 163–170, https://doi.org/10.16461/j.cnki.1000-4734.2021.41.067 [in Chinese with English abstract].

Haas, J.R., Shock, E.L., and Sassani, D.C., 1995, Rare earth elements in hydrothermal systems: Estimates of standard partial molal thermodynamic properties of aqueous complexes of the rare earth elements at high pressures and temperatures: Geochimica et Cosmochimica Acta, v. 59, p. 4329–4350, https://doi.org/10.1016/0016-7037(95)00314-P.

Halley, R.B., and Schmoker, J.W., 1983, High-porosity Cenozoic carbonate rocks of south Florida: Progressive loss of porosity with depth: American Association of Petroleum Geologists Bulletin, v. 67, p. 191–200, https://doi.org/10.1306/03B5ACE6-16D1-11D7-8645000102C1865D.

Han, T., Fan, H., Zhu, X., Wen, H., Zhao, C., and Xiao, F., 2017, Submarine hydrothermal contribution for the extreme element accumulation during the early Cambrian, South China: Ore Geology Reviews, v. 86, p. 297–308, https://doi.org/10.1016/j.oregeorev.2017.02.030.

Hao, F., Zhang, X., Wang, C., Li, P., Guo, T., Zou, H., Zhu, Y., Liu, J., and Cai, Z., 2015, The fate of CO_2 derived from thermochemical sulfate reduction (TSR) and effect of TSR on carbonate porosity and permeability, Sichuan Basin, China: Earth-Science Reviews, v. 141, p. 154–177, https://doi.org/10.1016/j.earscirev.2014.12.001.

Hirani, J., Bastesen, E., Boyce, A., Corlett, H., Gawthorpe, R., Hollis, C., John, C.M., Robertson, H., Rotevatn, A., Whitaker, F., and Lokier, S., 2018, Controls on the formation of stratabound dolostone bodies, Hammam

TABLE A4. C AND O ISOTOPIC VALUES OF CARBONATE MINERALS, YELI-LIANGJIASHAN FORMATION, CHENGDAO-ZHUANGHAI AREA, CHINA

Well	Depth (m)	Lithology	δ^{13}C (‰, VPDB)	δ^{18}O (‰, VPDB)
ZG28	4137.93	D1	–1.41	–6.03
CB244	2920.60	D1	0.07	–7.00
ZG28	4134.73	D2	–1.68	–5.05
ZG28	4122.92	D2	0.07	–5.70
ZG28	4126.87	D2	–1.16	–5.51
ZH102	4622.26	D2	–1.39	–5.77
ZH102	4626.44	D2	–1.52	–5.00
ZH102	4624.26	D2	–0.72	–5.43
ZH102	4623.86	D2	–0.84	–5.29
CB244	2899.19	D3	0.45	–6.86
CB244	2903.77	D3	0.38	–7.17
CB244	2914.37	D3	–1.49	–6.55
ZH102	4622.92	D3	–0.51	–6.76
ZH102	4623.56	D3	–0.43	–6.81
CB302	4005.45	D3	–2.15	–7.16
CB302	4007.76	D3	–0.37	–6.95
CB302	4005.45	Cd1	–0.28	–6.28
CB244	2903.77	Cd1	0.43	–7.72
ZH102	4622.96	Cd1	–0.35	–6.62
CB302	4003.50	D4	–0.51	–8.50
CB302	4004.00	D4	–0.66	–8.08
CB302	4004.80	D4	0.26	–7.89
CB302	4001.96	D4	–0.10	–7.26
CB302	4001.00	D4	–0.51	–8.07
ZH102	4622.66	D4	–0.25	–7.77
ZH102	4624.36	Cd2	0.43	–13.41
CBG6	3037.70	Cd2	–0.46	–13.95
CB302	4005.45	Cd2	–0.60	–14.25
CB302	4007.76	Cd2	–0.78	–14.93
ZG28	4122.92	SD	–0.40	–17.12
CB244	2903.77	SD	–1.18	–18.19
CB244	2914.37	SD	–0.55	–19.15
ZH102	4622.96	C1	–1.27	–15.24
ZH102	4624.36	C1	–2.10	–17.06
CB244	2903.77	C1	–2.26	–17.67
CB302	4007.76	C1	–1.61	–18.24
CB302	4002.36	C1	–1.64	–15.09
CB302	4004.46	C1	–2.27	–17.85
CB244	2914.37	C1	–1.69	–16.02
ZG28	4122.92	C1	–1.43	–14.26
CB302	4003.76	C2	–2.35	–15.40
CB302	4007.76	C2	–2.27	–12.13
CB302	4005.45	C2	–2.53	–12.42
ZH102	4622.96	C2	–2.72	–12.89

Note: Lithologies: D1—relict grains of the dolorudstones; D2, D3, and D4—matrices of fine crystalline dolostone (FCD), fine to medium crystalline dolostone (FMCD), and medium to coarse crystalline dolostone (MCCD), respectively; Cd1, Cd2—earliest-formed dolomite cement and dolomite cement adjacent to Cd1, respectively; SD—saddle dolomite; C1, C2—first and second type of calcite; respectively. VPDB—Vienna Peedee belemnite standard.

TABLE A5. IN SITU SR ISOTOPIC VALUES OF CARBONATE MINERALS, YELI-LIANGJIASHAN FORMATION, CHENGDAO-ZHUANGHAI AREA, CHINA

Well	Depth (m)	Lithology	^{87}Sr/^{86}Sr	Well	Depth (m)	Lithology	^{87}Sr/^{86}Sr
CB244	2903.77	D3	0.708898	CB244	2914.37	C1	0.716710
ZH102	4623.36	D3	0.708829	CB244	2903.77	C1	0.716713
CB302	4001.96	D4	0.709160	CB302	4007.76	C1	0.716742
CB302	4003.50	D4	0.709249	CB302	4002.36	C1	0.716922
ZH102	4622.66	D4	0.709069	ZG28	4122.92	C1	0.716704
CB302	4002.36	Cd1	0.708850	ZH102	4624.26	C2	0.715616
CB244	2903.77	Cd1	0.709010	ZH102	4623.86	C2	0.715573
CB302	4007.76	Cd2	0.714817	ZH102	4624.26	C2	0.715353
ZH102	4623.36	Cd2	0.714547	CB302	4005.45	C2	0.714985
CB244	2914.37	SD	0.714962	CB302	4007.76	C2	0.714594
ZG28	4122.92	SD	0.714724				

Note: Lithologies: D3, D4—fine to medium crystalline dolostone (FMCD) and medium to coarse crystalline dolostone (MCCD), respectively; Cd1, Cd2—earliest-formed dolomite cement and dolomite cement adjacent to Cd1, respectively; C1, C2—first and second type of calcite, respectively.

Faraun fault block, Gulf of Suez: Sedimentology, v. 65, p. 1973–2002, https://doi.org/10.1111/sed.12454.

Hollis, C., Bastesen, E., Boyce, A., Corlett, H., Gawthorpe, R., Hirani, J., Rotevatn, A., and Whitaker, F., 2017, Fault-controlled dolomitization in a rift basin: Geology, v. 45, p. 219–222, https://doi.org/10.1130/G38s394.1.

Holm, E.A., Zacharopoulos, N., and Srolovitz, D.J., 1998, Nonuniform and directional grain growth caused by grain boundary mobility variations: Acta Materialia, v. 46, p. 953–964, https://doi.org/10.1016/S1359-6454(97)00307-8.

Hu, W., Chen, Q., Wang, X., and Cao, J., 2010, REE models for the discrimination of fluids in the formation and evolution of dolomite reservoirs: Oil & Gas Geology, v. 31, no. 6, p. 810–818, https://doi.org/10.1016/S1876-3804(11)60008-6 [in Chinese with English abstract].

Huang, B., Zhang, S., Lu, Z., Ye, N., Zhu, B., Ding, X., and Li, Y., 2021, Origin of dolomites in Lower–Middle Ordovician carbonate rocks in the Yingshan Formation, Gucheng area, Tarim Basin: Evidence from petrography and geochemical data: Marine and Petroleum Geology, v. 134, https://doi.org/10.1016/j.marpetgeo.2021.105322.

Jia, L., Cai, C., Li, K., Liu, L., Chen, Z., and Tan, X., 2022, Impact of fluorine-bearing hydrothermal fluid on deep burial carbonate reservoirs: A case study from the Tazhong area of Tarim Basin, northwest China: Marine and Petroleum Geology, v. 139, https://doi.org/10.1016/j.marpetgeo.2022.105579.

Jiang, L., Worden, R.H., and Yang, C., 2018, Thermochemical sulphate reduction can improve carbonate petroleum reservoir quality: Geochimica et Cosmochimica Acta, v. 223, p. 127–140, https://doi.org/10.1016/j.gca.2017.11.032.

Jin, C., Qiao, D., and Tan, W., 2012, Meso-Cenozoic volcanic rock distribution and reservoir characteristics in the Bohai Bay Basin: Oil & Gas Geology, v. 33, no. 1, p. 19–29, https://doi.org/10.11743/ogg20120103.

Jin, Z., and Yu, K., 2011, Characteristics and significance of the burial dissolution of dolomite reservoirs: Taking the Lower Paleozoic in eastern Tarim Basin as an example: Petroleum Exploration and Development, v. 38, p. 428–435, https://doi.org/10.1016/S1876-3804(11)60045-1.

Jiu, B., Huang, W., and Li, Y., 2020, The effect of hydrothermal fluids on Ordovician carbonate rocks, southern Ordos Basin, China: Ore Geology Reviews, v. 126, https://doi.org/10.1016/j.oregeorev.2020.103803.

Jiu, B., Huang, W., Mu, N., and Hao, R., 2022, Petrology, mineralogy and geochemistry of Ordovician rocks in the southwest of Tarim Basin: Implications for genetic mechanism and evolution model of the hydrothermal reformed-paleokarst carbonate reservoir: Marine and Petroleum Geology, v. 140, https://doi.org/10.1016/j.marpetgeo.2022.105687.

Kaczmarek, S.E., and Thornton, B.P., 2017, The effect of temperature on stoichiometry, cation ordering, and reaction rate in high-temperature dolomitization experiments: Chemical Geology, v. 468, p. 32–41, https://doi.org/10.1016/j.chemgeo.2017.08.004.

Kareem, K.H., Al-Aasm, I.S., and Mansurbeg, H., 2021, Geochemical constraints on hydrothermal alteration of dolostones: An example of Lower Cretaceous Qamchuqa Formation, Kurdistan region, northern Iraq: Marine and Petroleum Geology, v. 134, https://doi.org/10.1016/j.marpetgeo.2021.105337.

Katz, D.A., Eberli, G.P., Swart, P.K., and Smith, L.B., 2006, Tectonic-hydrothermal brecciation associated with calcite precipitation and permeability destruction in Mississippian carbonate reservoirs, Montana and Wyoming: American Association of Petroleum Geologists Bulletin, v. 90, p. 1803–1841, https://doi.org/10.1306/03200605072.

Koeshidayatullah, A., Corlett, H., Stacey, J., Swart, P.K., Boyce, A., Robertson, H., Whitaker, F., Hollis, C., and Qing, H., 2020a, Evaluating new fault-controlled hydrothermal dolomitization models: Insights from the Cambrian dolomite, Western Canadian sedimentary basin: Sedimentology, v. 67, p. 2945–2973, https://doi.org/10.1111/sed.12729.

Koeshidayatullah, A., Corlett, H., Stacey, J., Swart, P.K., Boyce, A., and Hollis, C., 2020b, Origin and evolution of fault-controlled hydrothermal dolomitization fronts: A new insight: Earth and Planetary Science Letters, v. 541, https://doi.org/10.1016/j.epsl.2020.116291.

Köster, M.H., Hölzl, S., and Gilg, H.A., 2017, A strontium isotope and trace element geochemical study of dolomite-bearing bentonite deposits in Bavaria (Germany): Clay Minerals, v. 52, p. 161–190, https://doi.org/10.1180/claymin.2017.052.2.01.

Land, L.S., 1983, The application of stable isotopes to studies of the origin of dolomite and to problems of diagenesis of clastic sediments, *in* Arthur, M.A., Anderson, T.F., Kaplan, I.R., Veizer, J., and Land, L.S., eds., Stable Isotopes in the Sedimentary Geology: Society of Economic Paleontologists and Mineralogists (SEPM) Short Course Notes 10, p. 4.1–4.22, https://doi.org/10.2110/scn.83.01.0000.

Lavoie, D., Chi, G., Urbatsch, M., and Davis, W.J., 2010, Massive dolomitization of a pinnacle reef in the Lower Devonian West Point Formation (Gaspé Peninsula, Quebec): An extreme case of hydrothermal dolomitization through fault-focused circulation of magmatic fluids: American Association of Petroleum Geologists Bulletin, v. 94, p. 513–531, https://doi.org/10.1306/09080909083.

Lawrence, M.G., Greig, A., Collerson, K.D., and Kamber, B.S., 2006, Rare earth element and yttrium variability in south east Queensland waterways: Aquatic Geochemistry, v. 12, p. 39–72, https://doi.org/10.1007/s10498-005-4471-8.

Li, J., Wang, Y., Liu, C., Dong, D., and Gao, Z., 2016, Hydrothermal fluid activity and the quantitative evaluation of its impact on carbonate reservoirs: A case study of the Lower Paleozoic in the west of Dongying sag, Bohai Bay Basin: Petroleum Exploration and Development, v. 43, p. 395–403, https://doi.org/10.1016/S1876-3804(16)30046-5.

Li, K., Cai, C., Tan, X., Jiang, H., and Fan, J., 2022, Multiple fluid flow events and diversity of hydrothermal minerals in Neoproterozoic to Lower Paleozoic carbonate reservoirs, Tarim Basin, NW China: Journal of Asian Earth Sciences, v. 233, https://doi.org/10.1016/j.jseaes.2022.105260.

Li, M., Zhang, H., Hu, Z., and Zhang, F., 2004, Study of Paleozoic sequence stratigraphy in Jiyang depression: Oil & Gas Geology, v. 25, no. 1, p. 106–110, https://doi.org/10.11743/ogg20040120 [in Chinese with English abstract].

Li, Q., Chen, C., Tao, C., Wu, T., Zhou, J., Su, Z., Zhu, Z., Liu, L., Jie, T., and Chen, M., 2023, Evidence of hydrothermal fluid migration pathways in pores and microfractures based on nuclear magnetic resonance and electron microscopic analyses from the Southwest Indian Ridge: Marine Geology, v. 457, https://doi.org/10.1016/j.margeo.2023.107012.

Li, T., Zhu, D., Yang, M., Zhang, X., Li, P., Lu, C., and Zou, H., 2021, Early-stage marine dolomite altered by hydrothermal fluids in the Middle Permian Maokou Formation in the eastern Sichuan Basin, southern China: Marine and Petroleum Geology, v. 134, https://doi.org/10.1016/j.marpetgeo.2021.105367.

Li, W., Wu, Z., Zhang, M., Zhen, D., and Zhou, Y., 2006, Development characteristic of Mesozoic and Cenozoic faults and its control over deposition in Chengdao area: Journal of China University of Petroleum, v. 30, no. 1, p. 1–6.

Lima, B.E.M., Tedeschi, L.R., Pestilho, A.L.S., Santos, R.V., Vazquez, J.C., Guzzo, J.V.P., and De Ros, L.F., 2020, Deep-burial hydrothermal alteration of the presalt carbonate reservoirs from northern Campos Basin, offshore Brazil: Evidence from petrography, fluid inclusions, Sr, C and O isotopes: Marine and Petroleum Geology, v. 113, https://doi.org/10.1016/j.marpetgeo.2019.104143.

Lin, H., 2006, The forming mechanism of dolomite reservoir pace of Lower Paleozoic in Zhuanghai region, Jiyang Depression: Petroleum Geology and Recovery Efficiency, v. 13, no. 3, p. 5–7 [in Chinese with English abstract].

Lin, H., Xiong, W., Wang, Y., Qin, F., Jing, A., Wang, X., Zhang, M., Feng, Y., and Liu, J., 2021, Hydrocarbon accumulation in Chengdao buried hill of Jiyang Depression: Petroleum Geology and Recovery Efficiency, v. 28, no. 1, p. 1–9, https://doi.org/10.13673/j.cnki.cn37-1359/te.2021.01.001.

Liu, B., Qian, X., and Wang, Y., 1999, Tectono-sedimentary evolution of North China plate in the early Paleozoic: Chinese Journal of Geology, v. 34, no. 3, p. 347–356 [in Chinese with English abstract].

Liu, H., Zhao, D., Jiang, Y., Zhuang, M., and Liu, Y., 2016, Hydrocarbon accumulation model for Neogene traps in the Chengdao area, Bohai Bay Basin, China: Marine and Petroleum Geology, v. 77, p. 731–745, https://doi.org/10.1016/j.marpetgeo.2016.06.017.

Liu, L.H., Ma, Y.S., Liu, B., and Wang, C.L., 2017, Hydrothermal dissolution of Ordovician carbonates rocks and its dissolution mechanism in Tarim Basin, China: Carbonates and Evaporites, v. 32, p. 525–537, https://doi.org/10.1007/s13146-016-0309-2.

Liu, T., Ding, W., Zhang, R., Li, J., Feng, G., Han, P., Zhou, X., Ye, D., and Zhang, Z., 2023, Cenozoic tectonostratigraphy and structural styles in the Nangong Sag, Bohai Bay Basin, eastern China: Implications for the generation of oil-gas traps: Marine and Petroleum Geology, v. 149, https://doi.org/10.1016/j.marpetgeo.2022.106081.

Liu, Y., Hu, Z., Gao, S., Günther, D., Xu, J., Gao, C., and Chen, H., 2008, In situ analysis of major and trace elements of anhydrous minerals by LA-ICP-MS without applying an internal standard: Chemical Geology, v. 257, p. 34–43, https://doi.org/10.1016/j.chemgeo.2008.08.004.

Liu, Y., Wu, Z., Liu, L., Zhang, X., Li, W., Chen, S., and Hao, X., 2019, Cenozoic fault system and tectonic framework of Chengbei sag and its adjacent areas, Bohai Bay Basin: Geotectonica et Metallogenia, v. 43, no. 6, p. 1133–1143, https://doi.org/10.16539/j.ddgzyckx.2019.04.016 [in Chinese with English abstract].

Liu, Y., Liu, L., Wu, Z., Li, W., and Hao, X., 2022, New insight into East Asian tectonism since the late Mesozoic inferred from erratic inversions of NW-trending faulting within the Bohai Bay Basin: Gondwana Research, v. 102, p. 17–30, https://doi.org/10.1016/j.gr.2020.01.022.

Lonnee, J., and Machel, H.G., 2006, Pervasive dolomitization with subsequent hydrothermal alteration in the Clarke Lake gas field, Middle Devonian Slave Point Formation, British Columbia, Canada: American Association of Petroleum Geologists Bulletin, v. 90, p. 1739–1761, https://doi.org/10.1306/03060605069.

Loucks, R.G., 1999, Paleocave carbonate reservoirs: Origins, burial-depth modifications, spatial complexity, and reservoir implications: American Association of Petroleum Geologists Bulletin, v. 83, p. 1795–1834, https://doi.org/10.1306/E4FD426F-1732-11D7-8645000102C1865D.

Loucks, R.G., 2003, Origin of Lower Ordovician Ellenburger Group brecciated and fractured reservoirs in west Texas: Paleocave, thermobaric, tectonic, or all of the above?: American Association of Petroleum Geologists Search and Discovery Article 90013, https://www.searchanddiscovery.com/pdfz/abstracts/pdf/2003/annual/short/ndx_78591.PDF.html (accessed July 2023).

Lucia, F.J., Major, R.P., 1994, Porosity evolution through hypersaline reflux dolomitization, *in* Purser, B., Tucker, M., and Zenger, D., eds., Dolomites: A Volume in Honour of Dolomieu: Oxford, UK, International Association of Sedimentologists, p. 325–341, https://doi.org/10.1002/9781444304077.ch18.

Luczaj, J.A., Harrison, W.B., III, and Smith Williams, N., 2006, Fractured hydrothermal dolomite reservoirs in the Devonian Dundee Formation of the central Michigan Basin: American Association of Petroleum Geologists Bulletin, v. 90, p. 1787–1801, https://doi.org/10.1306/06270605082.

Luo, X., Fang, X., Zhang, Y., and Zhang, Y., 2021, Structural characteristics and formation mechanism of the Palaeozoic buried hills of the Zhuanghai area in the Jiyang Depression: Earth Science Frontiers, v. 28, no. 1, p. 33–42, https://doi.org/10.13745/j.esf.sf.2020.5.3.

Ma, X., Zhang, Z., and Wang, Y., 1998, The Tremadocian–early Arenigian (Early Ordovician) sequence stratigraphy and lithofacies paleogeography of North China: Chinese Journal of Geology, v. 33, no. 2, p. 166–179 [in Chinese with English abstract].

Machel, H.G., 2004, Concepts and models of dolomitization: A critical reappraisal, *in* Braithwaite, C.J.R., Rizzi, G., and Darke, G., eds., The Geometry and Petrogenesis of Dolomite Hydrocarbon Reservoirs: Geological Society, London, Special Publication 235, p. 7–63, https://doi.org/10.1144/GSL.SP.2004.235.01.02.

Machel, H.G., and Lonnee, J., 2002, Hydrothermal dolomite—A product of poor definition and imagination: Sedimentary Geology, v. 152, p. 163–171, https://doi.org/10.1016/S0037-0738(02)00259-2.

Mansurbeg, H., Morad, D., Othman, R., Morad, S., Ceriani, A., Al-Aasm, I., Kolo, K., Spirov, P., Proust, J.N., Preat, A., and Koyi, H., 2016, Hydrothermal dolomitization of the Bekhme formation (Upper Cretaceous), Zagros Basin, Kurdistan region of Iraq: Record of oil migration and degradation: Sedimentary Geology, v. 341, p. 147–162, https://doi.org/10.1016/j.sedgeo.2016.05.015.

Mansurbeg, H., Alsuwaidi, M., Salih, N., Shahrokhi, S., and Morad, S., 2021, Integration of stable isotopes, radiometric dating and microthermometry of saddle dolomite and host dolostones (Cretaceous carbonates, Kurdistan, Iraq): New insights into hydrothermal dolomitization: Marine and Petroleum Geology, v. 127, https://doi.org/10.1016/j.marpetgeo.2021.104989.

Martín-Martín, J.D., Travé, A., Gomez-Rivas, E., Salas, R., Sizun, J.P., Vergés, J., Corbella, M., Stafford, S.L., and Alfonso, P., 2015, Fault-controlled and stratabound dolostones in the late Aptian–earliest Albian Benassal Formation (Maestrat Basin, E Spain): Petrology and geochemistry constraints: Marine and Petroleum Geology, v. 65, p. 83–102, https://doi.org/10.1016/j.marpetgeo.2015.03.019.

Mattey, D., Lowry, D., and Macpherson, C., 1994, Oxygen isotope composition of mantle peridotite: Earth and Planetary Science Letters, v. 128, p. 231–241, https://doi.org/10.1016/0012-821X(94)90147-3.

Milliman, J.D., 1974, Precipitation and cementation of deep-sea carbonate sediments, *in* Inderbitzen, A.L., ed., Deep-Sea Sediments: Physical and Mechanical Properties: Boston, Massachusetts, Springer, p. 463–476, https://doi.org/10.1007/978-1-4684-2754-7_23.

Möller, P., Morteani, G., and Schley, F., 1980, Discussion of REE distribution patterns of carbonatites and alkalic rocks: Lithos, v. 13, p. 171–179, https://doi.org/10.1016/0024-4937(80)90018-3.

Montañez, I.P., 1994, Late diagenetic dolomitization of Lower Ordovician, Upper Knox carbonates: A record of the hydrodynamic evolution of the southern Appalachian basin: American Association of Petroleum Geologists Bulletin, v. 78, p. 1210–1239, https://doi.org/10.1306/A25FEAB3-171B-11D7-8645000102C1865D.

Montes-Hernandez, G., Findling, N., and Renard, F., 2016, Dissolution-precipitation reactions controlling fast formation of dolomite under hydrothermal conditions: Applied Geochemistry, v. 73, p. 169–177, https://doi.org/10.1016/j.apgeochem.2016.08.011.

Nelson, D.R., Chivas, A.R., Chappell, B.W., and McCulloch, M.T., 1988, Geochemical and isotopic systematics in carbonatites and implications for the evolution of ocean-island sources: Geochimica et Cosmochimica Acta, v. 52, p. 1–17, https://doi.org/10.1016/0016-7037(88)90051-8.

Pan, L., Shen, A., Zhao, J.-x., Hu, A., Hao, Y., Liang, F., Feng, Y., Wang, X., and Jiang, L., 2020, LA-ICP-MS U-Pb geochronology and clumped isotope constraints on the formation and evolution of an ancient dolomite reservoir: The Middle Permian of northwest Sichuan Basin (SW China): Sedimentary Geology, v. 407, https://doi.org/10.1016/j.sedgeo.2020.105728.

Pan, L., Hu, A., Liang, F., Jiang, L., Hao, Y., Feng, Y., Shen, A., and Zhao, J., 2021, Diagenetic conditions and geodynamic setting of the middle Permian hydrothermal dolomites from southwest Sichuan Basin, SW China: Insights from in situ U-Pb carbonate geochronology and isotope geochemistry: Marine and Petroleum Geology, v. 129, https://doi.org/10.1016/j.marpetgeo.2021.105080.

Phillips, W.J., 1972, Hydraulic fracturing and mineralization: Journal of the Geological Society, v. 128, p. 337–359, https://doi.org/10.1144/gsjgs.128.4.0337.

Qiao, Z., Zhang, S., Shen, A., Hu, A., Liang, F., Luo, X., She, M., and Lv, X., 2020, Laser ablated U-Pb dating–based determination of burial dolomitization process: A case study of Lower Ordovician Penglaiba Formation of Yonganba outcrop in Tarim Basin: Acta Petrologica Sinica, v. 36, no. 11, p. 3493–3509, https://doi.org/10.18654/1000-0569/2020.11.15.

Qing, H., and Mountjoy, E.W., 1994, Formation of coarsely crystalline, hydrothermal dolomite reservoirs in the Presqu'ile Barrier, Western Canada sedimentary basin: American Association of Petroleum Geologists Bulletin, v. 78, p. 55–77, https://doi.org/10.1306/BDFF9014-1718-11D7-8645000102C1865D.

Qing, H., Qiao, Z., Zhang, S., Cosford, J., Hu, A., Liang, F., Wang, Y., and Zheng, J., 2023, δ^{26}Mg-δ^{13}C-δ^{18}O systems as geochemical tracers for dolomite recrystallization: A case study of Lower Ordovician dolomite from Tarim Basin: Chemical Geology, v. 619, https://doi.org/10.1016/j.chemgeo.2023.121302.

Radke, B.M., and Mathis, R.L., 1980, On the formation and occurrence of saddle dolomite: Journal of Sedimentary Research, v. 50, p. 1149–1168, https://doi.org/10.1306/212F7B9E-2B24-11D7-8648000102C1865D.

Ramos, F.C., Wolff, J.A., and Tollstrup, D.L., 2004, Measuring ^{87}Sr/^{86}Sr variations in minerals and groundmass from basalts using LA-MC-ICPMS: Chemical Geology, v. 211, p. 135–158, https://doi.org/10.1016/j.chemgeo.2004.06.025.

Rasbury, E.T., and Cole, J.M., 2009, Directly dating geologic events: U-Pb dating of carbonates: Reviews of Geophysics, v. 47, no. 3, RG3001, https://doi.org/10.1029/2007RG000246.

Roberts, N.M.W., Rasbury, E.T., Parrish, R.R., Smith, C.J., Horstwood, M.S.A., and Condon, D.J., 2017, A calcite reference material for LA-ICP-MS U-Pb geochronology: Geochemistry, Geophysics, Geosystems, v. 18, p. 2807–2814, https://doi.org/10.1002/2016GC006784.

Roberts, N.M.W., Drost, K., Horstwood, M.S.A., Condon, D.J., Chew, D., Drake, H., Milodowski, A.E., McLean, N.M., Smye, A.J., Walker, R.J., Haslam, R., Hodson, K., Imber, J., Beaudoin, N., and Lee, J.K., 2020, Laser ablation inductively coupled plasma mass spectrometry (LA-ICP-MS) U-Pb carbonate geochronology: Strategies, progress, and limitations: Geochronology, v. 2, no. 1, p. 33–61, https://doi.org/10.5194/gchron-2-33-2020.

Rollett, A.D., Srolovitz, D.J., and Anderson, M.P., 1989, Simulation and theory of abnormal grain growth—Anisotropic grain boundary energies and mobilities: Acta Metallurgica, v. 37, p. 1227–1240, https://doi.org/10.1016/0001-6160(89)90117-X.

Saller, A.H., Pollitt, D., and Dickson, J.A.D., 2014, Diagenesis and porosity development in the First Eocene reservoir at the giant Wafra field, Partitioned Zone, Saudi Arabia and Kuwait: American Association of Petroleum Geologists Bulletin, v. 98, p. 1185–1212, https://doi.org/10.1306/12021313040.

Shen, A., Hu, A., Cheng, T., Liang, F., Pan, W., Feng, Y., and Zhao, J., 2019, Laser ablation in situ U-Pb dating and its application to diagenesis-porosity evolution of carbonate reservoirs: Petroleum Exploration and Development, v. 46, p. 1127–1140, https://doi.org/10.1016/S1876-3804(19)60268-5.

Sibley, D.F., and Gregg, J.M., 1987, Classification of dolomite rock textures: Journal of Sedimentary Research, v. 57, p. 967–975, https://doi.org/10.1306/212F8CBA-2B24-11D7-8648000102C1865D.

Song, J., 2001, Re-recognization of Huaiyuan movement: Geology of Shandong, v. 17, no. 1, p. 19–23, 51 [in Chinese with English abstract].

Song, M., Wang, H., and Zhang, Y., 2019, "Extrusion, tension and strike-slip" mountain-forming mechanism and reservoir type of buried hills in Jiyang Depression: Petroleum Geology and Recovery Efficiency, v. 26, no. 4, p. 1–8, https://doi.org/10.13673/j.cnki.cn37-1359/te.2019.04.001.

Stacey, J., Corlett, H., Holland, G., Koeshidayatullah, A., Cao, C., Swart, P., Crowley, S., and Hollis, C., 2021a, Regional fault-controlled shallow dolomitization of the Middle Cambrian Cathedral Formation by hydrothermal fluids fluxed through a basal clastic aquifer: Geological Society of America Bulletin, v. 133, p. 2355–2377, https://doi.org/10.1130/B35927.1.

Stacey, J., Hollis, C., Corlett, H., and Koeshidayatullah, A., 2021b, Burial dolomitization driven by modified seawater and basal aquifer-sourced brines: Insights from the Middle and Upper Devonian of the Western Canadian sedimentary basin: Basin Research, v. 33, p. 648–680, https://doi.org/10.1111/bre.12489.

Su, J., Wang, X., Yang, H., Yu, F., Li, Y., Ma, S., Wei, C., Weng, N., and Yang, Y., 2021, Hydrothermal alteration and hydrocarbon accumulations in ultra-deep carbonate reservoirs along a strike-slip fault system, Tarim Basin, NW China: Journal of Petroleum Science Engineering, v. 203, https://doi.org/10.1016/j.petrol.2021.108605.

Tang, Y., Cui, K., Zheng, Z., Gao, J., Han, J., Yang, J., and Liu, L., 2020, LA-ICP-MS U-Pb geochronology of wolframite by combining NIST series and common lead-bearing MTM as the primary reference material: Implications for metallogenesis of South China: Gondwana Research, v. 83, p. 217–231, https://doi.org/10.1016/j.gr.2020.02.006.

Taylor, S.R., and McLennan, S.M., 1985, The Continental Crust: Its Composition and Evolution: London, Blackwell Scientific, 312 p., https://doi.org/10.1017/S0016756800032167.

Tian, W., Wang, Y., Jing, A., Xin, Y., and Yang, G., 2021, Study of the characteristics and main controlling factors of Lower Palaeozoic carbonate reservoir in Tanhai areas of Jiyang Depression: Geological Review, v. 67, no. S1, p. 119–120, https://doi.org/10.16509/j.georeview.2021.s1.053.

Veizer, J., and Prokoph, A., 2015, Temperatures and oxygen isotopic composition of Phanerozoic oceans: Earth-Science Reviews, v. 146, p. 92–104, https://doi.org/10.1016/j.earscirev.2015.03.008.

Veizer, J., Ala, D., Azmy, K., Bruckschen, P., Buhl, D., Bruhn, F., Carden, G.A.F., Diener, A., Ebneth, S., Godderis, Y., Jasper, T., Korte, C., Pawellek, F., Podlaha, O.G., and Strauss, H., 1999, ^{87}Sr/^{86}Sr, δ^{13}C and δ^{18}O evolution of Phanerozoic seawater: Chemical Geology, v. 161, p. 59–88, https://doi.org/10.1016/S0009-2541(99)00081-9.

Wang, D., Zhang, X., Yang, L., Chen, X., Ma, S., and Wu, Z., 2022a, Influence of pre-existing faults on Cenozoic structures in the Chengbei sag and the Wuhaozhuang area, Bohai Bay Basin, East China: Marine and Petroleum Geology, v. 138, https://doi.org/10.1016/j.marpetgeo.2022.105539.

Wang, L., Hu, W., Wang, X., Cao, J., and Chen, Q., 2014, Seawater normalized REE patterns of dolomites in Geshan and Panlongdong sections, China: Implications for tracing dolomitization and diagenetic fluids: Marine and Petroleum Geology, v. 56, p. 63–73, https://doi.org/10.1016/j.marpetgeo.2014.02.018.

Wang, X., Wang, J., Cao, Y., Han, J., Wu, K., Liu, Y., Liu, K., and Xie, M., 2022b, Characteristics, formation mechanism and evolution model of Ordovician carbonate fault-controlled reservoirs in the Shunnan area of the Shuntuogole lower uplift, Tarim Basin, China: Marine and Petroleum Geology, v. 145, https://doi.org/10.1016/j.marpetgeo.2022.105878.

Wang, Y., and Li, J., 2017, Characteristics and main controlling factors of layered reservoir in buried hill of carbonate rock in Pingfangwang oilfield, Jiyang Depression: Journal of China University of Petroleum, v. 41, no. 4, p. 27–35, https://doi.org/10.3969/j.issn.1673-5005.2017.04.004 [in Chinese with English abstract].

Warren, J., 2000, Dolomite: Occurrence, evolution and economically important associations: Earth-Science Reviews, v. 52, p. 1–81, https://doi.org/10.1016/S0012-8252(00)00022-2.

Webb, G.E., and Kamber, B.S., 2000, Rare earth elements in Holocene reefal microbialites: A new shallow seawater proxy: Geochimica et Cosmochimica Acta, v. 64, p. 1557–1565, https://doi.org/10.1016/S0016-7037(99)00400-7.

Wei, C., and Li, S., 2011, Effect of temperature gradient on grain growth behavior from phase field simulations: Acta Physica Sinica, v. 60, no. 10, p. 132–139, https://doi.org/10.7498/aps.60.100701 [in Chinese with English abstract].

Wei, W., Chen, D., Qing, H., and Qian, Y., 2017, Hydrothermal dissolution of deeply buried Cambrian dolomite rocks and porosity generation: Integrated with geological studies and reactive transport modeling in the Tarim Basin, China: Geofluids, v. 2017, p. 1–19, https://doi.org/10.1155/2017/9562507.

Wendte, J., Chi, G., Al-Aasm, I., and Sargent, D., 2009, Fault/fracture controlled hydrothermal dolomitization and associated diagenesis of the Upper Devonian Jean Marie Member (Redknife Formation) in the July Lake area of northeastern British Columbia: Bulletin of Canadian Petroleum Geology, v. 57, p. 275–322, https://doi.org/10.2113/gscpgbull.57.3.275.

Weyl, P.K., 1960, Porosity through dolomitization—Conservation-of-mass requirements: Journal of Sedimentary Research, v. 30, p. 85–90, https://doi.org/10.1306/74D709CF-2B21-11D7-8648000102C1865D.

White, D.E., 1957, Magmatic, connate, and metamorphic waters: Geological Society of America Bulletin, v. 68, p. 1659–1682, https://doi.org/10.1130/0016-7606(1957)68[1659:MCAMW]2.0.CO;2.

Wierzbicki, R., Dravis, J.J., Al-Aasm, I., and Harland, N., 2006, Burial dolomitization and dissolution of Upper Jurassic Abenaki platform carbonates, Deep Panuke reservoir, Nova Scotia, Canada: American Association of Petroleum Geologists Bulletin, v. 90, p. 1843–1861, https://doi.org/10.1306/03200605074.

Woodhead, J., and Petrus, J., 2019, Exploring the advantages and limitations of in situ U-Pb carbonate geochronology using speleothems: Geochronology, v. 1, p. 69–84, https://doi.org/10.5194/gchron-1-69-2019.

Wu, S., Yu, Z., Zhang, R., Han, W., and Zou, D., 2005, Mesozoic–Cenozoic tectonic evolution of the Zhuanghai area, Bohai Bay Basin, East China: The application of balanced cross-sections: Journal of Geophysics and Engineering, v. 2, p. 158–168, https://doi.org/10.1088/1742-2132/2/2/011.

Xiao, S., Lü, D., Hou, M., Hu, H., and Huang, Z., 2019, Mesozoic tectonic evolution and buried hill formation mechanism in the southwestern Bohai Sea: Natural Gas Industry, v. 39, no. 5, p. 34–44, https://doi.org/10.13745/j.esf.sf.2021.9.22.

Xu, S., Bi, H., Li, S., Somerville, I., Ye, Q., Feng, H., and Li, M., 2017, Deep burial dissolution of Lower Palaeozoic carbonates and the role of compacted released water from Palaeogene strata in the Zhuanghai area, Jiyang Depression, Bohai Bay Basin, NE China: Geological Journal, v. 52, p. 30–44, https://doi.org/10.1002/gj.2730.

Yang, S., Qi, L., and Li, S., 2012, Fracture types, development phases and controlling factors of Chengbei 20 buried hills in Chengdao area: Journal of China University of Petroleum, v. 36, no. 5, p. 1–6, https://doi.org/10.3969/j.issn.1673-5005.2012.05.001.

Yang, Z., Liu, X., Han, X., Zhou, H., Zhan, S., Gui, X., Niu, J., and Wang, K., 2022, Multiple-stage injection of deep hydrothermal fluids in the dolostone reservoirs of Ordovician Majiagou Formation, southern Ordos Basin: Frontiers of Earth Science, v. 10, https://doi.org/10.3389/feart.2022.954192.

Ye, T., Wei, A., Lu, F., Hu, Z., Sun, Z., and Deng, H., 2019, Characteristic of inversion tectonics of pre-Cenozoic and formation mechanism in southwest of Bohai Bay area: Acta Geologica Sinica, v. 93, no. 2, p. 317–328, https://doi.org/10.19762/j.cnki.dizhixuebao.2019018.

Zhang, W., Guan, P., Jian, X., Feng, F., and Zou, C., 2014, In situ geochemistry of Lower Paleozoic dolomites in the northwestern Tarim basin: Implications for the nature, origin, and evolution of diagenetic fluids: Geochemistry, Geophysics, Geosystems, v. 15, no. 7, p. 2744–2764, https://doi.org/10.1002/2013GC005194.

Zhang, X., Li, Q., You, X., Ma, L., Jing, A., Tian, W., and Wen, L., 2022, Characteristics and formation mechanism of the Lower Paleozoic dolomite reservoirs in the Dongying Depression, Bohai Bay Basin: Energies, v. 15, https://doi.org/10.3390/en15062155.

Zhang, Z., Li, Z., Kang, H., Peng, D., Zhou, H., and Gao, R., 2015, Paleozoic stratigraphic characteristics and its tectonic significance in Chengdao oilfield: Geoscience, v. 29, no. 6, p. 1377–1386.

Zhao, Y.-Y., Zheng, Y.-F., and Chen, F., 2009, Trace element and strontium isotope constraints on sedimentary environment of Ediacaran carbonates in southern Anhui, South China: Chemical Geology, v. 265, p. 345–362, https://doi.org/10.1016/j.chemgeo.2009.04.015.

Zhou, Z., Wen, H., Qin, C., de Fourestier, J., Liu, L., and Shi, Q., 2018, The genesis of the Dahebian Zn-Pb deposit and associated barite mineralization: Implications for hydrothermal fluid venting events along the Nanhua Basin, South China: Ore Geology Reviews, v. 101, p. 785–802, https://doi.org/10.1016/j.oregeorev.2018.08.013.

Zhu, D., Meng, Q., Jin, Z., Liu, Q., and Hu, W., 2015, Formation mechanism of deep Cambrian dolomite reservoirs in the Tarim Basin, northwestern China: Marine and Petroleum Geology, v. 59, p. 232–244, https://doi.org/10.1016/j.marpetgeo.2014.08.022.

Zong, G., Xiao, H., Li, C., Shi, Y., and Wang, L., 1999, Evolution of Jiyang Depression and its tectonic implications: Geological Journal of China Universities, v. 5, no. 3, p. 275–282, https://doi.org/10.16108/j.issn.1006-7493.1999.03.005 [in Chinese with English abstract].

Science Editor: Brad Singer
Associate Editor: Laishi Zhao

Manuscript Received 25 May 2023
Revised Manuscript Received 31 July 2023
Manuscript Accepted 11 August 2023

Printed in the USA